UNIVERSITY OF TRENTO

Doctoral School in Civil, Environmental and
Mechanical Engineering

Curriculum 3. Modelling and Simulation

Luigi Calabrese

Development of Devices Based on Electrically Actuated Soft Elastomers

2018 - Doctoral thesis

UNIVERSITY OF TRENTO - Italy

Department of Civil, Environmental
and Mechanical Engineering

Doctoral School in Civil, Environmental and Mechanical Engineering
Topic 3. Modelling and Simulation - XXXI cycle 2015/2018

Doctoral Thesis - July 2019

Luigi Calabrese

Development of Devices Based on Electrically Actuated Soft Elastomers

Supervisors
Prof. Nicola M. Pugno - University of Trento
Prof. Danilo De Rossi - University of Pisa
Prof. Massimiliano Gei - University of Cardiff

Except where otherwise noted, contents on this book are licensed under a Creative
Common Attribution - Non Commercial - No Derivatives
4.0 International License

University of Trento
Doctoral School in Civil, Environmental and Mechanical Engineering
http://web.unitn.it/en/dricam
Via Mesiano 77, I-38123 Trento
Tel. +39 0461 282670 / 2611 - *dicamphd@unitn.it*

Preface

The work presented in this thesis has been previously published in the form of two refereed journal articles. A third manuscript has been submitted for peer review.

- Calabrese, L., Frediani, G., Gei, M., De Rossi, D. E. and Carpi, F. (2018). Active compression bandage made of electroactive elastomers. *IEEE/ASME Transactions on Mechatronics*, 23(5), 2328-2337.
- De Acutis, A., Calabrese, L., Bau, A., Tincani, V., Pugno, N. M., Bicchi, A. and De Rossi, D. E. (2018). Design and proof of concept for multi degree of freedom hydrostatically coupled dielectric elastomer actuators with roto-translational kinematics for object handling. *Smart Materials and Structures*, 27(7), 074005.
- Calabrese, L., Berardo, A., De Rossi, D. E., Gei, M., Pugno, N. M., and Fantoni, G. (2019). A soft robot structure with limbless resonant, stick and slip locomotion. *Smart Materials and Structures*, (accepted).

Abstract

Dielectric elastomer (DE) actuators are electromechanical transducers that essentially consist of one layer of an insulating soft elastomer coated on both sides with compliant electrodes. When a voltage is applied between the electrodes, an electrostatic pressure deforms the elastomer triggering the motion of the actuator. In this thesis, this principle is exploited for the development of three different actuators: an electroactive compression bandage, a hydrostatically coupled actuator for use in the field of soft manipulators and a dielectric elastomer based inchworm-like robot able to perform locomotion. By doing so, several challenges related to the design, to the modeling and to the manufacturing of this kind of devices are raised and tackled.

During the development of the electroactive compression bandage, the issue of electrical insulation and prevention of electrical discharge in wearable devices was addressed by using coating layers as an interface between the DE actuator and the human body. Both experimental investigations and a finite electro-elasticity analytical model showed that the passive layers play a key role for an effective transmission of the actuation from the active layers to the load. Indeed, the model showed that by increasing the number of electroactive layers, the pressure variation can be increased, although with a saturation trend, providing a useful indication for future designs of such bandages.

The second piece of work here reported consists in a design upgrade of the Hydrostatically Coupled Dielectric Elastomer Actuator (HC-DEA), already known in the literature, that enable its use in the field of soft manipulators. The new design features segmented electrodes, which stand as four independent elements on the active membrane of the actuator, enabling it for generating both out of plane and in plane motions. This novel design makes the actuator suitable for delicate transportation of a flat object. This capability was proven via an experimental investigation in which a flat Petri dish was roto-translated on a platform composed of two actuators. The electromechanical transduction performance of the actuator was characterized and its contact mechanics was modeled.

Finally, a smart robot structure that exploits anisotropic friction to achieve stick-slip locomotion is presented. The robot, which is made out just of a plastic beam, a planar dielectric elastomer actuator and four bristle pads with asymmetric rigid metallic bristles, exploits the resonance condition to reach the maximum locomotion speed. The fundamental frequency of the structure, which was estimated both analytically and numerically, was identified within the range of frequencies in which the top locomotion speed was observed during the experiments to be identified.

Acknowledgements

I will never cease to be deeply grateful to Prof. Massimiliano Gei, whose expertise within the field of solid mechanics and electroactive polymers added considerably to this thesis. Also, I need to thank him for the precious time spent together at Cardiff University. Working under his guidance has been a tremendous source of knowledge and inspiration that I will bring with me for the rest of my life.

A very special thanks goes to Prof. Danilo De Rossi, for his technical support and his advices: without the facilities of the Interdepartmental Research Centre E. Piaggio of University of Pisa and his important mentoring, this work would not have been possible.

I am deeply grateful to Prof. Nicola Pugno for giving me the opportunity to work within the Laboratory of Bioinspired Graphene and Nanomechanics at the Department of Civil, Environmental and Mechanical Engineering of University of Trento. Prof. Pugno is a formidable generator of ideas which I admire for its incredible creativity. His support and mentoring are very much appreciated.

I have an immense debt of gratitude to Prof. Federico Carpi and Dr. Gabriele Frediani, that with their experience, understanding and patience, gave an important contribution to this thesis. I will never thank them enough for all the things that they taught me.

I also need to thank all the robotics group of the "E. Piaggio" Research Centre. In particular I would like to express my sincere gratitude to Prof. Antonio Bicchi, Dr. Vinicio Tincani, Dr. Carmelo De Maria, Dr. Aurora De Acutis and Dr. Andrea Baù for their help and teachings in the development, manufacturing and testing of the actuators here presented.

Prof. Gualtiero Fantoni also deserves a special recognition for his brilliant ideas shared with me during my time spent in Pisa.

I wish to thank the European Society for Electromechanically Active Polymers Transducers and Artificial Muscles (EuroEAP Society), in person of its former president Prof. Federico Carpi, for giving me the opportunity to participate to its activities. These valuable experiences really helped me in both technical and personal development.

This PhD thesis represents for me an important achievement, that has been possible thanks to the support of my dad Michele and my mother Nicolina: with their example they taught me integrity and abnegation, whit their sacrifices they made possible for me to reach the graduation; this work is dedicated to them.

I would like to thank my brother Luca for his support, these few words can not express how lucky I feel for having him in my life.

One day I will look back to these years and I will fondly remember the people that walked with me during this journey. My friends and PhD colleagues Giacomo Roverso and Martina Azzolini deserves a special recognition for their genuine and trustworthy friendship that I really treasure.

Contents

Preface iii

Abstract v

Acknowledgements vii

1 Introduction 1
1.1 Thesis outline 3

2 Theory of Dielectric Elastomers 5
2.1 Introduction 5
2.1.1 Dielectric elastomers 6
2.2 Elements of finite electro-elasticity 6
2.2.1 Kinematics 7
2.2.2 Strain measures 7
Case of incompressible materials 10
2.2.3 Statics 10
Deformation of an electromechanical transducer 11
2.3 Constitutive equations of finite electro-elasticity 12
2.3.1 The case of an active incompressible homogeneous membrane 12
2.3.2 Linear dielectric elastomer 13
2.3.3 Strain energy density function for a Neo-Hookean hyperelastic material 13
2.4 The Pelrine's model 14

3 Electroactive Compression Bandage Made of Soft Elastomers 17
3.1 Introduction 17
3.2 Active bandage concept 18
3.2.1 Active bandage specifications 19
3.3 Manufacturing of prototype active bandages 20
3.4 Testing of the prototype active bandages 21
3.5 Analytical model of the active bandage 23
3.5.1 Kinematics of the multilayer structure 23
3.5.2 Electro-mechanics of a single layer 25
3.5.3 Voltage-pressure relationship for the multilayer bandage 27
3.6 Model validation: comparison between experimental data and model predictions 29
3.7 Model predictions: contact pressure 30

3.8 Future developments 31
3.8.1 Improvement of the electromechanical properties 31
3.8.2 Improvements of the model 32
3.8.3 High-voltage driving: viability and challenges 32
3.9 Conclusions 33

4 Hydrostatically Coupled Dielectric Elastomer Actuator 35
4.1 Introduction 35
4.2 Conceptual design and working principle of the multi-DoF HC-DEA . 37
4.2.1 Key idea 37
4.2.2 Manufacturing 39
4.2.3 Actuation cycle 41
4.3 Mechanical interaction between the multi-DoF HC-DEA and objects . 42
4.3.1 Measurement of the static friction coefficient 42
4.3.2 Electro-mechanical performance 43
4.3.3 Compliance of the active membrane 45
4.4 Flat object roto-translation experiments 47
4.4.1 Driving Electronics 47
4.4.2 Translation test 48
4.4.3 Roto-translation test 48
4.5 Conclusions 50

5 Stick and slip locomotion of a Soft Resonant Structure 53
5.1 Introduction 53
5.2 Materials and Methods 54
5.2.1 Concept design 54
5.2.2 Robot components 54
Dielectric elastomer actuator 54
Plastic beam 56
Bristle pads 58
5.2.3 Robot manufacturing 61
5.2.4 Estimation of the fundamental frequency 62
Analytical: Rayleigh's quotient method 62
Numerical: finite element analysis 67
5.2.5 Frequency response analysis: calculation of net displacement and locomotion speed 67
5.2.6 Locomotion test: experimental setup and test procedure 70
5.3 Results and discussion 70
5.4 Conclusions 74

6 Summary and Outlook 75
6.1 Summary and Outlook 75

A List of Publications 77

List of Figures

2.1 Actuation of a single layer of dielectric elastomer film coated with compliant electrodes. 6
2.2 Deformation of a continuous body, the material point P in reference configuration is displaced by the deformation function in another material point p of the current configuration. 7
2.3 Strain in a continuous body, the oriented segment $\boldsymbol{dX}$ in the reference configuration B_0 is transformed into another oriented segment $\boldsymbol{dx}$ in the current configuration B. 8
2.4 Deformation of a plane membrane. 9
2.5 Deformation of a plane membrane, equilibrium in the current configuration is achieved under the normal tractions p_i. 10
2.6 Deformation of a dielectric membrane subjected to a combination of voltage and external tractions, the equilibrium in the current configuration is reached under the body forces generated by the electric field. 11
2.7 Maxwell pressure calculated for the Pelrine's model in the case of an incompressible material. 15

3.1 Schematic representation of the dynamic active bandage. The magnification shows the multilayer structure of the bandage, where two inner active layers (a_1 and a_2) are coupled to two passive layers (p_1 and p_2). Wooden stiffeners are embedded within the outer passive layer longitudinally in order to maximise actuation radially. Velcro stripes allow for securing the bandage to the limb. 19
3.2 Schematic drawing (top) and picture (bottom) of a prototype active bandage. 21
3.3 Testing of the prototype dynamic bandages: air chamber that mimicked the compliance of a human limb, without (a) and with (b) the bandage. 22
3.4 Electromechanical performance of three samples of bandages having a different initial thickness D_P of their passive layers. Quadratic fitting curves are used as a guide for the eye. 23

3.5 Schematic representation of the cross-section of the air chamber surrounded by the active bandage. (a) In the "initial state" B_b, the active bandage is secured around the rubber membrane of the chamber with an air chamber pressure P_b and a contact pressure P_{cb}, so that the bandage's inner radius R_{p1} is $\approx$ 40 mm (radial distances are denoted by the letter R), (b) In the "Voltage OFF" state B_0, the air chamber pressure is manually set to P_0=7.5 kPa, causing an expansion of the bandage (radial distances are denoted by $\bar{r}$). (c) Following the application of a voltage V, the system is switched to its"Voltage ON" state B_V, where the air chamber pressure decreases from P_0 to a lower value P_V and the contact pressure drops from P_{c0} to $P_c < P_{c0}$ (radial distances are denoted by the letter r). 24
3.6 Dependence of the air chamber pressure P_V on the applied voltage V: comparison between experimental data and model-based predictions, for the three types of prototype bandages having different thickness D_p of their passive layers. 29
3.7 Dependence of the contact pressure P_c on the applied voltage V for the three types of prototype bandages having different thickness D_p of their passive layers. 30
3.8 Variation of the contact pressure between the air chamber and the bandage, as estimated from the model for bandages having a different thickness D_p of the passive layers. 31
3.9 Relative variation of the contact pressure (with respect to its initial value) between the air chamber and the bandage, as estimated from the model for five types of prototype bandages having an increasing number of active layers and a constant thickness of the passive layers D_p= 2 mm. 32
3.10 Relative variation of the contact pressure (with respect to its initial value) at V=8 kV between the air chamber and the bandage, as estimated from the model for ten samples of prototype bandage having an increasing number of active layers and a constant thickness of the passive layers D_p= 2 mm. 32

4.1 A push-pull HC-DEA. In rest state (left) and in active state (right). . . . 38
4.2 Top view of the multi-DoF HC-DEA in its rest state (a) where the four independent electrodes enable the tridimensional displacement of the actuator's apical point. For example, when a driving voltage V is applied to the two electrodes on the right-hand side, a displacement is triggered along the x-axis coupled to a displacement along the z-axis (b). The electrode position within the coupled layers that constitute the active membrane of the actuator is also highlighted in the x-z section planes (c) and (d). 39
4.3 Schematic representation of the manufacturing process of the actuator. Fabrication procedure of both the active and the passive membranes (a), assembly of the actuator's components (b). 40

4.4 Actuation cycle used to induce the unidirectional motion of a flat object. The first row shows the pictures of the multi-DoF HC-DEA in each of the four steps of the actuation cycle (namely A, B, C and D), with its apical point identified by a red marker. A magnification of the voltage-induced deformation is shown in the second row, where the active membrane is represented by both the grey line V>0 and by the grey electrodes drawn in the logo (top right corner). The passive part is represented by the black bold line V=0 and by the black electrodes. The last row highlights the position of the apical point for each step in the cycle. 41

4.5 Conceptual scheme of the experimental set-up carried out to measure the static friction coefficient between the HC-DEA and diverse materials. In the picture, the execution of the experiment is broken down into four phases. Each phase is furnished with a graph of the normal and tangential force as functions of the displacement Δx and Δy of the carriers with respect to their location at the first phase: (a) the vertical carrier, on which a 6-axis ATI-Nano force/torque sensor and a plate of an established material are mounted, start moving down along the y-axis; (b) the plate contacts the HC-DEA and the descent of the carrier stops when a normal force N of 0.1 N is reached; (c) after N reaches 0.1 N, the horizontal carrier moves along the x-axis at a constant velocity of 0.5mm/s. A tangential force F_f arises on the system composed of the plate and the ATI sensor through the contact area at the apical point of the HC-DEA which, in this stage, does not move with respect to the plate; (d) as the horizontal carrier moves rightwards, the tangential force increases until it reaches a peak value when the contact area is on the verge of moving. After the peak value, that is the maximum static friction force we seek, the contact area translates rightwards and F_f slightly decreases at the value of the kinetic friction force. 43

4.6 Compression tests of the actuation unit: experimental set-up. The compression tests of the actuator were performed with a uniaxial testing machine (left) equipped with a load cell for force measurements. The contact area was approximated with a circle of radius a (right). 44

4.7 Plot of the normal blocking force N as a function of the driving voltage V, experimental data and best fitting function $N = f(V)$= 7.646 10^{-10} $V^{2.354}$. The correspondent tangential blocking force $F_f = \mu f(V)$ is also reported for a static friction coefficient μ=0.63 obtained for the contact with ABS plastic. 45

4.8 The contact circle radius a as a function of the driving voltage V, experimental data and best fitting function $a = h(V) = 0.315V^{0.352}$. . . . 46

4.9 Compression force N vs contact circle radius a, experimental data and nonlinear function $a = g(N)$. The curve a= 7.270 $N^{0.149}$ obtained for the multi-DoF HC-DEA is in the range set by the curves a= 2.070 $N^{0.259}$ relating to a silicone finger and a=6.740 $N^{0.050}$ relating to a viscoelastic finger. 47

4.10 The modular electronic circuit employed for the activation of each multi-DoF HC-DEA. 48

4.11 Setup used for the roto-translation test. Two multi-DoF HC-DEAs enclosed in the support structure used for the experiment. 49
4.12 Roto-translation sequence of a Petri Dish on an array of two multi-DoF HC-DEAs. Starting from the rest position (a), in each of the 5 steps of actuation (b), (c), (d), (e) and (f) both actuators performed rotation phases R, or translation phases T. When both actuators were Activated Clockwise (AC) a translation phase T was performed, resulting in a translation of the petri dish along the x-axis Δx=3mm. On the other hand, when the Actuator 1 was Activated Anticlockwise (AA), a rotation phase R was performed, resulting in a clockwise rotation of the petri dish $\Delta\theta = 2.25°$. 50

5.1 Schematic drawing of the locomotion robot (a) consisting of an assembly of three components: a plastic beam, a dielectric elastomer actuator and four clawed pads featuring rigid bristles with an asymmetric orientation. The locomotion cycle (b) starts from the initial self-standing configuration (top); when a voltage V is applied to the DE actuator, an elongation is induced resulting in a forward slip of the front bristles (centre); finally, when the voltage is switched off the DE actuator shrinks, resulting in a forward slip of the back bristles (bottom). 55
5.2 Schematic drawing of the DE actuator with embedded stiffening elements aligned along the transversal direction. When a load pre-stretches the actuator, the initial length l_0 is obtained (left). Upon application of a driving voltage V and since the elongation along the other in-plane direction is prevented by the stiffening elements, the actuator elongates along the longitudinal direction only reaching the length $l < l_0$. 56
5.3 Tensile test of the DE actuator to calculate the tensile stiffness k_{DEA}=29.85 N/m. The test was performed with a strain rate of 0.043 s^{-1}. 57
5.4 Schematic drawing of the structure of the robot: unbent plastic structure (a), self-standing operational configuration (b) and particular of the clawed pads featuring the asymmetric steel bristles (c). All dimensions are expressed in mm. 57
5.5 Tensile test of the styrene plastic material: experimental stress-strain data and estimation of the Young's modulus. 58
5.6 Bristle pads: resin 3D printed (a), stainless steel (b). 59
5.7 Experimental setup for the measurement of the friction force generated at the interface between the testing surface and the bristle pads. The bristle pad sample coupled to the sample holder and loaded with a mass m = 20 g constituting the slider. A double inextensible wire allowed for pulling the slider with a tensile machine along the linear guide covered with a layer of baking paper showed in the enlargement of the picture. 60
5.8 Static (a) and dynamic (b) friction coefficients of the six 3D printed bristle pads (indicated with the values of the angles) and the steel bristle pad. 61
5.9 Static and dynamic friction coefficients of the 3D printed bristle pads for increasing value of the bristle's angle. 62

5.10 Variation of the backward vs forward sliding static and dynamic friction coefficients of the 3D printed bristle pads for increasing value of the bristle's angle. The error bar associated with each value of $\Delta\mu_s$ and $\Delta\mu_s$ is calculated according to the variance sum law. 63
5.11 Schematic representation of the robot structure. Top: longitudinal section. Bottom: top view of the detail of the connection between curved beam, straight actuator and clawed pads (whose perimeters are sketched with dashed lines) (left) and detail of the cross sections (right). Coordinate z describes the out-of-plane axis. Dimensions are expressed in mm. 64
5.12 Schematic representation of the robot about the initial configuration of equilibrium. An imposed horizontal displacement δ_x in D induces a vertical displacement $1.772\delta_x$ in F. The magnification shows the kinematics of the rigid motion of the structure about point D. 64
5.13 Mesh of the robot plastic structure about the initial configuration of equilibrium. The DE actuator is not visually represented since its presence is imposed as equivalent spring constraints to the plastic structure. 68
5.14 Kelvin-Voigt model adopted to describe the viscoelastic behaviour of the DE actuator. 69
5.15 Picture of the experimental setup. 70
5.16 Locomotion speed v_x vs actuation frequency f: experimental data and model prediction for the unloaded (top) and loaded with m=9 g (bottom) robot. Bars represent the standard deviation of measures. The two dotted lines represent the fundamental frequency f_n calculated with either the Rayleigh's quotient method (on the right in both plots) or the FEM modal analysis (on the left in both plots). 71
5.17 Eigenfrequencies and modal shapes of a 3D model of the robot: first vibration mode for the unloaded (top left) and loaded with m=9 g (top right) robot; second vibration mode for the unloaded (bottom left) and loaded with m=9 g (bottom right) robot. 72
5.18 Fundamental frequency vs lumped mass weight. The experimental data corresponding to the peak values of the locomotion speed, namely 19 Hz for m=9 g and 23 Hz for m=0 are marked by dots. The blue solid line represents the predictions of the Rayleigh's quotient method whereas the red solid one refers to the FEM calculations performed with a step along the abscissa corresponding to Δm=0.1 g. 73

List of Tables

3.1 Values of the hoop stretch of the midline in the initial configuration B_b for each layer of the three samples of bandages tested in state B_b. . . . 25

4.1 Values of the static friction coefficient measured for different materials. 43

W

Chapter 1

Introduction

With the advent of the so-called “Soft Robotics", soft materials are increasingly used for the development of both robots and their sub-components [1, 2]. With respect to the traditional “rigid" robotics, this new field aims at building robots with highly compliant materials, exploiting the continuum deformation with theoretically an infinite number of degrees-of-freedom, often inspired by biological organisms [3]. By exploiting the adaptability of such materials, as well as new design architectures, soft robots can accomplish a large variety of tasks that are impossible to perform by using rigid materials [4, 5]. Nowadays, soft robots and soft actuators are expanding their influence well beyond the traditional fields: from manufacturing and automation, they are rapidly approaching healthcare and human-robot cooperative manipulation. Therefore, the interaction with humans is set to be unavoidable, in particular for the case of wearable devices.

Since the beginning of this new research field, that can be dated back to the 1980s with the development of the first artificial muscles based on contractile polymers [6], several materials and actuation methods to convert chemical or electrical energy into mechanical work have been investigated. At first, polymer gels were deeply studied due to their remarkable capability of shrinking their volume as much as 1000 times in response to small changes in external conditions such as temperature, pH, electric fields or solvent or ionic composition [7]. While polymer gels revealed great potential [8, 9, 10], limitations linked to the material’s performance(i.e. low response time, elastic modulus, tensile strength and fatigue life) as well as thermodynamic limits (low power and force densities) and several unsolved engineering challenges related to their construction limited their use [6]. Later on, conducting polymers were also investigated for developing soft muscle-like actuators. Compared to polymer gels, conducting polymer revealed a much better dimensional scalability and durability due to the possibility of using a solid electrolyte, although the limitations concerning their response speed remained unsolved [11, 12, 13].

When both high power density and actuation speed are required, inflatable elastomeric actuators powered by the pneumatic technology are usually considered one of the best solutions [14]. Indeed, since the application of flexible microactuators to robotic mechanisms [15], reported in the literature as one of the first examples of soft inflatable robots [5], the pneumatic technology has been playing a key role for the development of soft robots. Also, when the elastomeric matrix is endowed with flexible fibers, self- sensing and programmable motion capabilities [16, 17, 18], as well as even higher actuation pressures and hence larger force outputs [19] are possible. Despite these advancements, inflatable actuators still present relevant limitations, since they inevitably require the presence of channels for the fluid's flow within the material's structure and also needs external pumping systems, making them unsuitable for many applications [4]. Infinite degrees-of-freedom soft actuators were also developed by using tendon-driven mechanisms [20, 21], that however still relied on traditional motors and rigid transmission mechanism for their operation, therefore no significant advantage over the pneumatic technology was achieved yet.

Smart materials have been recently used to overcome these limitations, with particular relevance of Shape Memory Alloys (SMAs) that, despite the difficult control due to their temperature-dependent behavior, were successfully used to develop a soft octopus arm using a SMAs tendon [22, 23]. Very high temperature-induced deformation has also been reported in the literature for the case of highly twisted fishing line or sewing thread forming coiled muscles. Indeed, these muscles can contract by 49%, lift loads over 100 times heavier than can human muscle of the same length and weight, and generate 5.3 kilowatts of mechanical work per kilogram of muscle weight, similar to that produced by a jet engine [24].

The use of smart materials within the field of soft robotics has been rapidly growing in the last two decades, in particular for a specific kind of Electromechanically Active Polymers (EAPs) called Dielectric Elastomers (DEs). Indeed, DEs were increasingly adopted as actuation technology for the development of smart actuators and soft robots due to their high force output, large actuation strain, high power-to-weight ratio and noiseless operation [25, 26]. Indeed, since they present the best performance in terms electromechanical transduction among all the class of EAPs, they are seen as one of the most promising technologies for the development of soft actuators and robots [13]. Moreover, due to their self-sensing capability [27], it is possible to integrate them in soft robotic systems to form smart soft robots, in which the actuation and the sensing functions could be performed simultaneously as happens for human muscles.

Despite these positive aspects and the great versatility that this technology features, the use of DEs to build soft actuators still raises several challenges, that depending on the intended application to be developed, might present themselves under different aspects. In order to address some of those challenges, this thesis presents three case studies that helped to highlight different aspects that anyone who intends to develop such devices may face.

The first case that we consider is the case of wearable devices, in which the issue of electrical insulation and prevention of electrical discharge must be properly solved by using coating layers as an interface between the DE actuator and the human body. In this case, since they inevitably interfere with the transmission of the load from the body to the actuator, it is important to understand how such coating layers affects the performance of the DE actuator. To asses this aspect, Chapter 3 presents a case study where a soft electro-mechanically active compression bandage developed for medical applications is designed, manufactured and tested, highlighting the influence of the insulating layers on the actuation performance for this kind of devices.

Another challenge that often arises within the field of soft manipulators is the problem of 3D manipulation of delicate and fragile objects. In this case, a contextual generation of both a normal and a tangential thrust on the object by using just one

DE actuator is required. However, since DEs are basically made of a thin membrane coated on both sides with compliant electrodes that expands in the plane upon the application of a driving voltage, they are generally not able to operate with a 3D trajectory, unless special architectures are adopted. This issue is treated in Chapter 4, where an upgraded design of the HC-DEA first presented by Carpi et. al [28] allows for achieving this new functionality.

The last problem presented in Chapter 5 deals with the challenge of coupling of a soft DE actuator with a flexible elastic structure. In particular, we present a locomotion robot composed by a linear DE actuator and a flexible beam able to perform locomotion thanks to the presence of asymmetric rigid bristles. By analyzing the dynamic properties and the frequency response of the resulting structure we show that a DE actuator can be successfully used to trigger a higher locomotion speed in correspondence of the resonance frequency of the robot.

1.1 Thesis outline

Chapter 2 provides a brief introduction to the theory of dielectric elastomers, in particular introducing some elements of finite electro-elasticity which are particularly relevant to the experiments and results presented in this thesis. Chapter 3 presents the wearable soft electro-mechanically active compression bandage previously mentioned, Chapter 4 reports about the soft actuator developed for manipulation of delicate and fragile objects and Chapter 5 presents the locomotion robot composed by a linear DE actuator and a flexible beam able to perform locomotion thanks to the presence of asymmetric rigid bristles. Finally, Chapter 6 concludes the thesis with a summary of the key results.

Chapter 2

Theory of Dielectric Elastomers

2.1 Introduction

Electromechanically Active Polymers (EAPs) are smart materials able to respond to applied electrical stimuli with changes of size and/or shape [29, 13, 30]. They are the electro-mechanical transducers that most closely emulate muscles, so that they earned the moniker "artificial muscles" [25]. EAPs are usually divided in two main categories: electronic and ionic.

Electronic EAPs are basically soft capacitors, in which the space between electrodes is filled with a dielectric layer made of elastomer material. The actuation is triggered upon voltage driving by the electrostatic forces generated between the two electrodes. They typically require high actuation voltages, but since there is no power required to keep the actuation position, energy consumption is very low. This class of electro-active polymers exhibit fast response to electric stimulus, high mechanical energy density and high actuation force. They are also able to exhibit remarkably high voltage-induced deformations that can range from 360% in linear strain clamped elastomer [31], to 488% area strain in membranes under equal-biaxial dead load [32], up to 1692% area strain in elastomer membrane mounted on an air chamber [33]. Once the voltage is turned off they return to the initial state. In electronic EAPs the actuation is not dependent on voltage polarity: whichever electrode is positively or negatively charged, the motion is uniquely defined.

In ionic EAPs the actuation is triggered by ion diffusion inside the polymer, therefore they admit bi-directional motion depending on voltage polarity. Ionic flow require time, hence actuation speed is lower than in electronic EAPs. Despite a lower voltage required to start the motion (typically 1-5 V), a considerable power consumption (higher than in electronic EAPs is needed in order to reach the desired position and also to keep it. Another drawback of this class of actuators is that they need an electrolyte to allow the ion flow, meaning that they must operate in wet state.

Since Dielectric Elastomers (DEs) are the most performing electronic EAPs in terms of output force and response speed [26, 13, 34, 35], they were used for the developement of the actuators presented in this work.

2.1.1 Dielectric elastomers

Dielectric elastomers are electromechanical transducers that can operate in two different manners: when they convert electrical into mechanical energy are called actuators; when they operate in reverse mode, converting mechanical into electrical energy they are called generators. In this thesis we focused only on the actuation mode. DE actuators can be considered simply as soft capacitors since they are essentially made of a thin layer of an insulating elastomer coated on both sides with compliant electrodes [36]. When a DC driving voltage V is applied between the electrodes of a planar DE actuator, an electrostatic pressure parallel to the electric field E, which is known as Maxwell stress, squeezes the membrane reducing its thickness and expanding its area [26]. Due to material incompressibility, area expansion and thickness reduction are related one to another. Figure 2.1 shows the DE working principle. The derivation of the expression of the Maxwell stress for this particular case, according to the Pelrine's model [26], is reported later in this chapter.

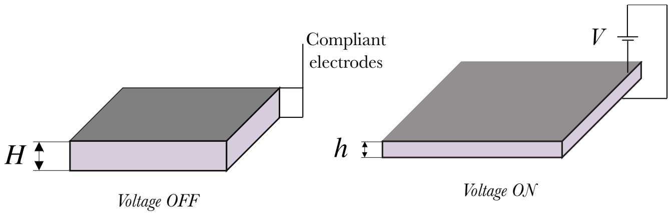

FIGURE 2.1: Actuation of a single layer of dielectric elastomer film coated with compliant electrodes.

Due to their low elastic modulus, elastomeric materials presents large displacements even in response at relative low applied forces. Upon application of an initial stress state, the elastomeric media show consistent deformations, resulting in displacements comparable or even greater than any other dimension of the body. This behaviour invalidates assumptions inherent infinitesimal strain theory, therefore equilibrium equations must be written in deformed configuration to take in account the effect of these large strains. In the following sections some elements of finite strain theory of electro-elasticity are reported.

2.2 Elements of finite electro-elasticity

In continuum mechanics, the finite strain theory describes the deformation of solid bodies in which the displacements of the material particles are relevant to the body dimensions. In this case, equilibrium is written with respect to the deformed configuration, but it can be also described in terms of a reference configuration that usually coincides to the initial, stress-free configuration of the actuator [37, 38].

2.2.1 Kinematics

The deformation function χ of a body is a vector field that has, in general, two components: the first one is a rigid displacement in which the body translate and rotate without changing shape; the second one is a change in shape and size accompanied by strain. From the combination of these two components the undeformed body in the so called "reference configuration" B_0 deforms to the "current configuration" B. Figure 2.2 shows a schematic representation of this concept. In general, a motion of B is a smooth function that assign to each material point $\boldsymbol{X}$ and time t a point $\boldsymbol{x} = \chi(\boldsymbol{X}, t)$ [37]. Relative displacement between material points occurs if and only if a strain has occurred. A deformation that occurs without strain is called rigid-body displacement. In the following we will refer to a unique deformed configuration (defined by a combination of applied voltage and prestretch), therefore from now on we will neglect the time dependency.

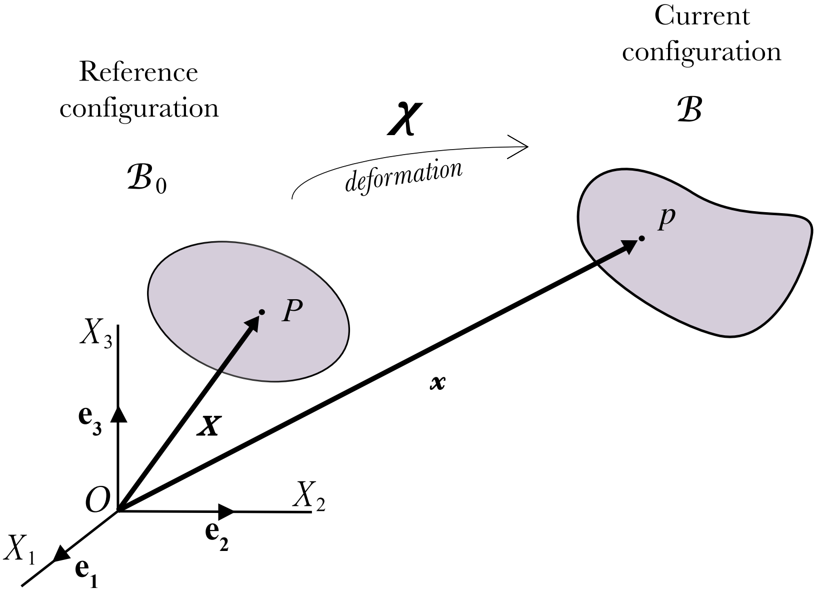

FIGURE 2.2: Deformation of a continuous body, the material point P in reference configuration is displaced by the deformation function in another material point p of the current configuration.

2.2.2 Strain measures

Let's consider a certain infinitesimal oriented straight line segment $\boldsymbol{dX}$ in the neighbourhood of a material point of the the reference configuration B_0, see Figure 2.3. The strain component of the displacement vector χ describes its transformation in another infinitesimal oriented segment $\boldsymbol{dx}$ that is part of the current configuration B. The strain can be expressed by means of a deformation gradient tensor.

The deformation gradient tensor $\boldsymbol{F} = \boldsymbol{F}(\chi)$ that describe the strain state is given by:

$$\boldsymbol{F} = Grad(\chi). \tag{2.1}$$

Since it is related to both reference and current configuration, $\boldsymbol{F}$ is a two-point tensor, meaning that operates with input quantities from the reference domain B_0 and giving outputs in the current domain B. Thanks to this operator it is possible to define the infinitesimal oriented segment $\boldsymbol{dx}$ in the current configuration as:

$$\boldsymbol{dx} = Grad(\chi)\boldsymbol{dX}. \tag{2.2}$$

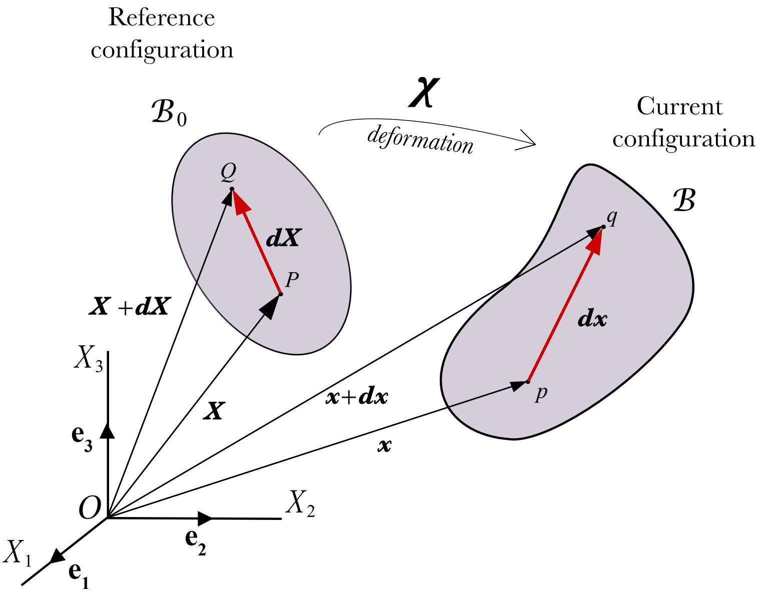
Reference configuration
$\mathcal{B}_0$
$\boldsymbol{\chi}$
deformation
Current configuration
$\mathcal{B}$
Q
dX
P
q
dx
p
X +dX
X
x+dx
x
X_3
$\mathbf{e}_3$
O
X_2
$\mathbf{e}_2$
X_1
$\mathbf{e}_1$

FIGURE 2.3: Strain in a continuous body, the oriented segment $\boldsymbol{dX}$ in the reference configuration B_0 is transformed into another oriented segment $\boldsymbol{dx}$ in the current configuration B.

A measure of the strain is given by the square modulus of $\boldsymbol{dx}$:

$$|\boldsymbol{dx}|^2 = \boldsymbol{dx} \cdot \boldsymbol{dx} = \boldsymbol{FdX} \cdot \boldsymbol{dX} = \boldsymbol{dX} \cdot \boldsymbol{F}^T\boldsymbol{FdX} = \boldsymbol{dX} \cdot \boldsymbol{CdX},$$

where $\boldsymbol{C} = \boldsymbol{F}^T\boldsymbol{F}$ is called right Cauchy-Green strain tensor.

$\boldsymbol{C}$ allows to quantify the deformation:

$$|\boldsymbol{dx}| = \sqrt{\boldsymbol{dX} \cdot \boldsymbol{CdX}}.$$

If $\boldsymbol{C} = \boldsymbol{I}$ then $|\boldsymbol{dx}| = |\boldsymbol{dX}|$, a zero strain deformation is described by the tensor. The left Cauchy-Green strain tensor $\boldsymbol{B} = \boldsymbol{F}\boldsymbol{F}^T$ is defined by inverting (2.2):

$$\boldsymbol{dX} = \boldsymbol{F}^{-1}\boldsymbol{dx}, \tag{2.3}$$

therefore:

$$|\boldsymbol{dX}|^2 = \boldsymbol{dX} \cdot \boldsymbol{dX} = \boldsymbol{F}^{\mathbf{-1}}\boldsymbol{dx} \cdot \boldsymbol{F}^{-1}\boldsymbol{dx} = \boldsymbol{dx}\boldsymbol{F}^{-T} \cdot \boldsymbol{F}^{-1}\boldsymbol{dx} = \boldsymbol{dx} \cdot \boldsymbol{B}^{-1}\,\boldsymbol{dx}.$$

Let's consider the strain of the plane membrane schematically represented in Figure 2.4. The strain described by the gradient tensor (2.1), in this specific case, makes the dimension of the membrane's sides change from L_1, L_2 and H to l_1, l_2 and h respectively.

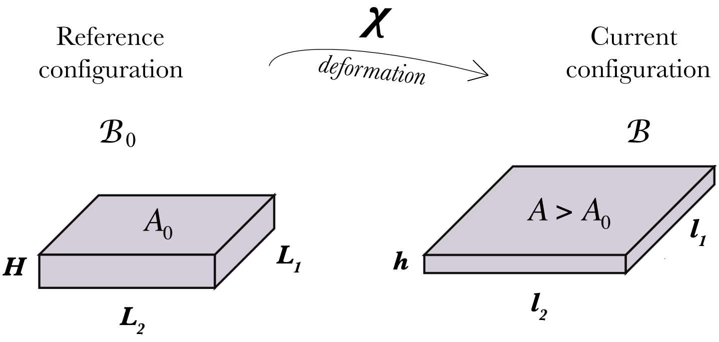

FIGURE 2.4: Deformation of a plane membrane.

For each direction, if the strain is homogeneous, the ratio given by the length of the membrane's side after the strain over the one before the strain is defined as the " stretch " and corresponds to the eigenvalue of $\boldsymbol{F}$ for the principal direction considered:

$$\lambda_1 = \frac{l_1}{L_1}, \tag{2.4}$$

$$\lambda_2 = \frac{l_2}{L_2}, \tag{2.5}$$

$$\lambda_3 = \frac{h}{H}. \tag{2.6}$$

In case of elongation $1 < \lambda_i < +\infty$, in case of contraction $0 < \lambda_i < 1$.

Case of incompressible materials

If the material is incompressible, the deformation occurs at constant volume, in that case:

$$V_0 = V = L_1 L_2 H = l_1 l_2 h. \tag{2.7}$$

Substituting equations (2.6) into (2.7) we obtain:

$$\lambda_3 = \frac{1}{\lambda_1\, \lambda_2}. \tag{2.8}$$

If $\lambda_1 \equiv \lambda_2$ then $\lambda_3 = \frac{1}{\lambda_1^2}$.

In general, for a non homogeneous deformation, incompressibility is expressed by:

$$J = det(\boldsymbol{F}) = \frac{dV}{dV_0} = 1. \tag{2.9}$$

For the deformation of a plane membrane made of an incompressible material, as the one shown in Figure 2.4, it turns out that:

$$\boldsymbol{F} = \begin{bmatrix} \lambda_1 & 0 & 0 \\ 0 & \lambda_2 & 0 \\ 0 & 0 & \lambda_3 \end{bmatrix} = \begin{bmatrix} \lambda_1 & 0 & 0 \\ 0 & \lambda_2 & 0 \\ 0 & 0 & \frac{1}{\lambda_1\, \lambda_2} \end{bmatrix}.$$

2.2.3 Statics

Figure 2.5 shows a deformation of an elastomeric membrane subject to a biaxial stress state.

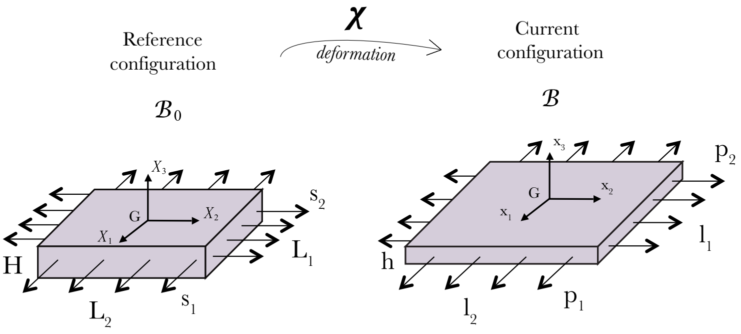
Reference configuration
$\mathcal{B}_0$
χ
deformation
Current configuration
$\mathcal{B}$
X_3
G
X_2
X_1
s_2
H
L_1
L_2
s_1
x_3
G
x_2
x_1
p_2
h
l_1
l_2
p_1

FIGURE 2.5: Deformation of a plane membrane, equilibrium in the current configuration is achieved under the normal tractions p_i.

In the current configuration B the membrane is in equilibrium under the so called external current normal tractions p_i, resulting in the total forces:

$$F_1 = p_1\, h\, l_2, \tag{2.10}$$
$$F_2 = p_2\, h\, l_1. \tag{2.11}$$

These expressions can be written in terms of undeformed dimensions L_1, L_2, H by using a fictitious nominal traction distribution s_i known as nominal external tractions:

$$F_1 = s_1\, H\, L_2, \tag{2.12}$$
$$F_2 = s_2\, H\, L_1. \tag{2.13}$$

By using this formulation there is no need to define the deformed geometry: once the nominal external tractions s_i are defined, the stress distribution in the current configuration B can be calculated by means of the geometric dimensions already known in B_0. The nominal tractions distribution is represented by the "first Piola-Kirchhoff stress tensor" $\boldsymbol{S}$, this tensor can be calculated from the Cauchy stress tensor $\boldsymbol{\sigma}$ as:

$$\boldsymbol{S} \;=\; J\,\boldsymbol{\sigma}\,\boldsymbol{F}^{-T}. \tag{2.14}$$

Deformation of an electromechanical transducer

Figure 2.6 shows the working principle of a dielectric elastomer electromechanical transducer. A soft dielectric membrane is coated on both sides with compliant electrodes; upon application of a voltage difference V an electrostatic force (equivalent to a body force) is generated between the electrodes. This force reduce the membrane thickness, due to the elastomer incompressibility this induce an area expansion.

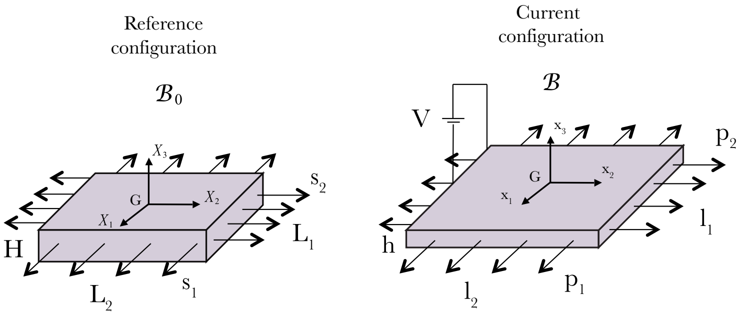

FIGURE 2.6: Deformation of a dielectric membrane subjected to a combination of voltage and external tractions, the equilibrium in the current configuration is reached under the body forces generated by the electric field.

2.3 Constitutive equations of finite electro-elasticity

2.3.1 The case of an active incompressible homogeneous membrane

The right hand side of Figure 2.6 shows a deformed dielectric elastomer membrane in the current configuration, where the generated Maxwell stress squeezes the membrane changing its dimensions from L_1, L_2 and H to l_1, l_2 and h respectively. Moreover, in this state the two electrodes accumulate electric charges $+Q$ and $-Q$ and in general the system stores a certain amount of Helmholtz free energy [36]. This section reports about the constitutive equations for such membrane, under the hypotesis of incompressible and isotropic material. The equations are expressed in terms of principal stretches λ_i, electric field E_i and electric displacement field D_i (i=1,2,3.). In the following, in order to maintain the Einstein convention implying summation over an index repeted twice, for generic quantities A_i and B_i (i=1,2,3.) it is useful to introduce the notations $[A/B]_i$ and $[AB]_i$ which correspond to A_i/B_i and A_iB_i, respectively.

Due to large strains accompanying the deformation of DE materials, constitutive equations are usually defined in terms of nominal quantities, such as principal components of nominal total stress S_i, nominal electric field E_i^0 and nominal electric displacement D_i^0, via a free energy $H(\lambda_i, E_i^0)$ as [38]:

$$S_i = \frac{\partial H}{\partial \lambda_i} + q\frac{1}{\lambda_i}, \tag{2.15}$$

$$\frac{\partial H}{\partial E_i^0} = -D_i^0, \tag{2.16}$$

where q is a pressure term defined by boundary conditions. These forms are implied by the expressions of the change $\dot{H}$ of H brought about by independent changes $\dot{\lambda}_i$ and $\dot{E}_i^0$

$$\dot{H} = S_i\dot{\lambda}_i + q\frac{\dot{\lambda}_i}{\lambda_i} - D_i^0\dot{E}_i^0. \tag{2.17}$$

As shown by isotropic finite-strain electro-mechanics, along principal axes $E_i^0 = [\lambda E]_i$, $D_i^0 = [D/\lambda]_i$ and $S_i^0 = [\sigma/\lambda]_i$, so that introducing the function $W(\lambda_i, E_i) = H(\lambda_i, [\lambda E]_i)$, it turns out that 2.17 is equivalent to

$$\frac{\partial W}{\lambda_i}\dot{\lambda}_i + \frac{\partial W}{E_i}\dot{E}_i = \left[\frac{\sigma}{\lambda}\right]_i\dot{\lambda}_i + q\frac{\dot{\lambda}_i}{\lambda_i} - \left[\frac{D}{\lambda}\right]_i\{[\dot{\lambda}E]_i + [\lambda\dot{E}]_i\}, \tag{2.18}$$

which corresponds to the constitutive equations in terms of true quantities:

$$\frac{\partial W}{\partial E_i} = -D_i \tag{2.19}$$

$$\frac{\partial W}{\partial \lambda_i} = \left[\frac{\sigma}{\lambda}\right]_i + q\frac{1}{\lambda_i} - \left[\frac{D}{\lambda}E\right]_i. \tag{2.20}$$

In particular, (2.20) can be rewritten as

$$\sigma_i = \lambda_i \frac{\partial W}{\partial \lambda_i} - q + D_i E_i \quad \text{(no sum on index } i\text{)}. \tag{2.21}$$

For a dielectric elastomer membrane, both the electric field $\boldsymbol{E}$ and the electric displacement field $\boldsymbol{D}$ only feature components along the direction of the electric field i.e. trough the membrane's thickness. Therefore, only E_3 and D_3 are not null. In this specific case we can write $E_3 = E$ and $D_3 = D$, so that (2.19) and (2.21) specializes to:

$$D = -\frac{\partial W}{\partial E}, \tag{2.22}$$

$$\sigma_1 - \sigma_3 = \lambda_1 \frac{\partial W}{\partial \lambda_1} - \lambda_3 \frac{\partial W}{\partial \lambda_3} - DE, \tag{2.23}$$

$$\sigma_2 - \sigma_3 = \lambda_2 \frac{\partial W}{\partial \lambda_2} - \lambda_3 \frac{\partial W}{\partial \lambda_3} - DE, \tag{2.24}$$

which is the form of the constitutive equations used in the following.

2.3.2 Linear dielectric elastomer

In a linear dielectric elastomer the electric field E and the electric displacement D are related by the permittivity ε (also called dielectric constant), that is assumed to be a constant independent from deformation:

$$E = \frac{D}{\varepsilon}. \tag{2.25}$$

2.3.3 Strain energy density function for a Neo-Hookean hyperelastic material

To describe the voltage-induced strain of a dielectric elastomer membrane we consider a strain energy density function W made of two components:

$$W = W_{mech} + W_E. \tag{2.26}$$

The component W_{mech} is independent of the electric field and is only associated with the stretching of the incompressible elastomer, therefore by assuming a Neo-Hookean hyperelastic material model for the material we can write:

$$W_{mech} = \frac{\mu}{2}(\lambda_1^2 + \lambda_2^2 + (\frac{1}{\lambda_1 \lambda_2})^2 - 3), \tag{2.27}$$

where Y is the Young's modulus and $\mu = \frac{Y}{3}$ is the shear modulus in the natural configuration.

The component W_E depends on the electric field only. By assuming the linear dielectric elastomer behaviour (2.25) it can be written as:

$$W_E = -\frac{1}{2}\varepsilon E^2. \tag{2.28}$$

In general, for a neo-Hookean incompressible electro-elastic material deforming non-homogeneously, the strain energy density function can be written as follow:

$$W = \frac{1}{2}\mu(\boldsymbol{F} \cdot \boldsymbol{F} - 3) + \frac{1}{2\varepsilon}\boldsymbol{E}^0 \cdot \boldsymbol{C}^{-1}\boldsymbol{E}^0, \tag{2.29}$$

where $\boldsymbol{E}^0 = \boldsymbol{F}^T\boldsymbol{D}$ is the electric field tensor in the reference configuration.

2.4 The Pelrine's model

When an active homogeneous membrane deforms under the effect of an electric field E, the equilibrium of the body is reached because the mechanical response of the elastomeric material equals the electrical-induced pressure, namely the Maxwell's pressure. Due to the 3D nature of the problem, to define the equilibrium on the external boundary of the elastomer, the stress jump between the two sides of the actuator must be considered [39]. This boundary value problem can be exemplified by considering the planar DE actuator of Figure 2.6. If no mechanical external forces are applied to the actuator, and the electric field outside the actuator is considered to be negligible, at the equilibrium both the total true and nominal stresses must be null at any point i.e. $\sigma_{ij} = S_{ij} = 0$, that for an isotropic material turns out to be

$$\sigma_i = S_i = 0 \quad (i = 1, 2, 3). \tag{2.30}$$

In order to solve this boundary value problem, in the following we consider a general form of the strain-energy function assuming the linear dielectric behaviour of the elastomer (2.25). In this case, a general form of a strain-energy function can be written as

$$W(\lambda_1, \lambda_2, E^0) = W_{mech}(\lambda_1, \lambda_2) - \frac{\varepsilon}{2}\left(\frac{E^0}{\lambda_1\lambda_2}\right)^2. \tag{2.31}$$

Considering (2.15) and (2.16), where the free energy H is substituted by (2.31) we obtain the following set of constitutive equations

$$S_i = \frac{\partial W(\lambda_1, \lambda_2, E^0)}{\partial \lambda_i} + q\frac{1}{\lambda_i}, \tag{2.32}$$

$$\frac{\partial W(\lambda_1, \lambda_2, E^0)}{\partial E^0} = -D^0. \tag{2.33}$$

From (2.33), by substituting (2.31) we obtain

$$D^0 = \frac{\partial W(\lambda_1, \lambda_2, E^0)}{\partial E^0} = \varepsilon\frac{E^0}{\lambda_1^2\lambda_2^2}, \tag{2.34}$$

while from (2.32) with (2.31) and (2.14) with $J = 1$ due to the incompressibility the total true stress components are:

$$\sigma_1 = \sigma_1^{mech} - \frac{\varepsilon}{2}E^2 - q \tag{2.35a}$$

$$\sigma_2 = \sigma_2^{mech} - \frac{\varepsilon}{2}E^2 - q \tag{2.35b}$$

$$\sigma_3 = \sigma_3^{mech} + \frac{\varepsilon}{2}E^2 - q. \tag{2.35c}$$

where the mechanical contribution of the stress associated with the elastic response of the material σ_i^{mech} has been introduced. As previously reported, for an incompressible solid superimposing an arbitrary hydrostatic pressure q does not change the response of the material. Therefore we can write the difference

$$\sigma_3^{mech} - \sigma_1^{mech} = \sigma_3^{mech} - \sigma_2^{mech} = -\varepsilon E^2. \tag{2.36}$$

If we set arbitrarily $\sigma_1^{mech} = \sigma_2^{mech} = 0$, it turns out that σ_3^{mech} is

$$\sigma_3^{mech} = -\varepsilon E^2 = -p, \tag{2.37}$$

which corresponds to the Maxwell's stress given by the Pelrine's model [40] as schematically represented in Figure 2.7.

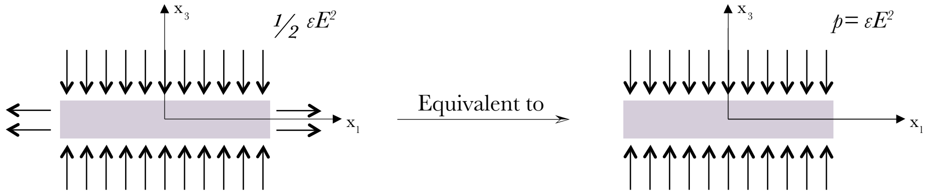

FIGURE 2.7: Maxwell pressure calculated for the Pelrine's model in the case of an incompressible material.

Chapter 3

Electroactive Compression Bandage Made of Soft Elastomers

Active compression bandages made of electro-mechanically active elastomers have recently been proposed to counteract dynamically, rather than statically, limb swelling due to various pathologies or conditions. To apply and modulate the compression pressure they exploit the ability of electroactive elastomer layer/s of changing size in response to a high voltage. For safety reasons such devices must be properly insulated from the user limb. In this work we present an electroactive bandage made of two pre-stretched layers of an electroactive acrylic elastomer sandwiched between two insulating layers of a passive silicone elastomer. Moreover, uniaxial stiffening elements where introduced to maximise actuation along the radial direction. Prototypes of the bandage were tested with a pressurized air chamber, which mimicked the compliance of a human limb. Both experimental investigations and a finite electro-elasticity analytical model showed that the passive layers play a key role for an effective transmission of actuation from the active layers to the load. The prototypes were able to actively vary the applied pressure up to 10%. The model showed that by increasing the number of electroactive layers the pressure variation could be further increased, although with a saturation trend, providing useful indication for future designs of such bandages.

This work has been published in the peer reviewed journal article:

- Calabrese, L., Frediani, G., Gei, M., De Rossi, D. E. and Carpi, F. (2018). Active compression bandage made of electroactive elastomers. *IEEE/ASME Transactions on Mechatronics*, 23(5), 2328-2337.

3.1 Introduction

Blood circulation from the lower limbs to the heart highly depends on vein valves and muscular compression on blood vessels. When those mechanisms are pathological, blood tends to accumulate in the lower limbs [41]. This may cause swelling, pain or lead to even more severe conditions [42], [43]. Treatments for those diseases include both static (passive) and dynamic (active) compression systems, such as stockings and pneumatic sleeves [44], [45]. The former are elastic garments applying a static pressure, typically in the range 20-60 mmHg (2.7-2.8 kPa) [46], which however have been proved to be less effective than pneumatic systems [47], [48]. On the other hand, the latter require bulky pneumatic cuffs and a pumping box, resulting impractical in many conditions.

An alternative solution to address these issues, consisting of electro-mechanically active bandages made of a dielectric elastomer actuator, was recently proposed [49], [50]. The device was conceived as a stretchable bandage consisting of a single layer of a silicone elastomer with compliant electrodes on both sides. The active bandage was designed to be wrapped around human limbs with an initial maximum pressure that can be dynamically reduced via an applied high-voltage. Considering the high voltage needed to activate the bandage, such device must prevent electrical discharges and guarantee proper insulation from both the human limb and the external environment.

To address this issue, the work reported in this chapter presents a dynamic active bandage featuring silicone elastomer coating layers acting as insulators. Moreover, the coating layers are analysed also in terms of their effect on the transmission of actuation from the active layers to the load. Furthermore, this work also presents the following means to improve the performance of such active bandages: a multi-layer structure for the active part, a more-performing active material and a design solution that maximises actuation along the radial direction. Both experimental tests and a finite electro-elasticity model, specifically developed for the multilayer bandage, were used to investigate the effects on the actuation performance of the number of the active layers and the thickness of the coating passive layers as reported in the following.

3.2 Active bandage concept

The bandage was conceived as a thin, stretchable and electro-responsive multilayer structure of elastomer films, to be wrapped around limbs as shown in Figure 3.1.Two active layers (a_1 and a_2) are sandwiched between two passive layers (p_1 and p_2).

Each inner active layer consists of a DE film coated with compliant electrodes. The two active layers are then coupled to thicker and softer passive layers. The passive layers have two key functions. Firstly, they serve as a mechanical interface with the limb, aimed at reducing the constraining effect introduced by the latter on the electrically induced deformation of the active layers. Secondly, as the proposed prototype bandage requires high driving voltages (as detailed in the following), the passive layers also ensure electrical safety, providing insulation. Wooden stiffening sticks were embedded within the outer passive layer, with the aim of maximising actuation (variation of pressure) along the radial direction, preventing elongations of the bandage longitudinally. Indeed, combining a DE actuator with unstretchable elements has previously been demonstrated to be effective for unidirectional actuation [51]. The

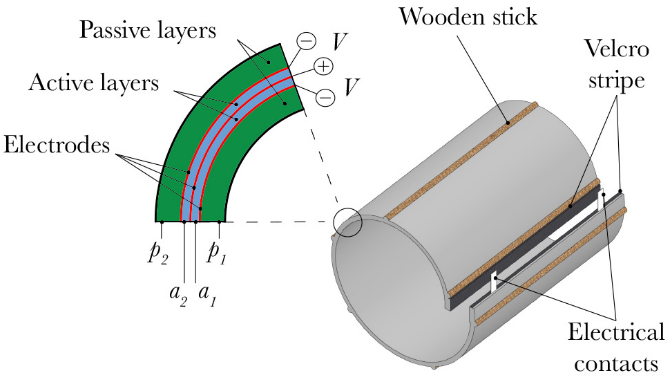

FIGURE 3.1: Schematic representation of the dynamic active bandage. The magnification shows the multilayer structure of the bandage, where two inner active layers (a_1 and a_2) are coupled to two passive layers (p_1 and p_2). Wooden stiffeners are embedded within the outer passive layer longitudinally in order to maximise actuation radially. Velcro stripes allow for securing the bandage to the limb.

bandage was conceived to be wrapped around the limb with a certain prestretch, thus applying a certain passive pressure. When a voltage V is applied between the electrodes, the bandage is able to partially release the initial passive pressure, by increasing its circumference. Therefore, by modulating the applied voltage it is possible to continuously vary the applied pressure. As mentioned above, prior to this work other investigators have reported on the use of DE actuators to develop active bandages [49, 50]. The peculiarities of the approach described here are:

1. two active layers were stacked together to increase the strength of the system;
2. the active layers were made of an acrylic elastomer film showing one of the highest electromechanical transduction performance, in terms of maximum achievable strains and stresses;
3. stiffening sticks were used to maximise actuation along the radial direction;
4. two thick and soft passive layers were used as interfaces with suitable properties in terms of mechanical compliance and electrical safety.

The effects of these improvements were investigated theoretically and experimentally as reported in the following sections.

3.2.1 Active bandage specifications

The bandage should be able to apply a maximum pressure comparable to those of elastic compression stockings, i.e. 1-6 kPa [52], and then reduce the pressure upon electric driving. The literature does not offer any widely accepted exact estimate on the variation of pressure required to compensate for a deficient blood return. This is likely due to the variability of individual pathological and anatomical conditions.

Indeed, for any given deficit, the compensation pressure could vary significantly according to the size of the limb, especially due to the thickness of muscles and adipose tissue. So, instead of targeting a specific performance, this work was aimed at validating the functionality of the proposed concept. This was achieved by manufacturing and characterising prototypes, as described below.

3.3 Manufacturing of prototype active bandages

Proof-of-concept prototype bandages were manufactured as follows. The active layers consisted of an acrylic elastomer film (VHB 4910, 3M, USA). This material was chosen in consideration of its well-known high electromechanical transduction performance in terms of achievable active stress [13, 26] and its adhesive properties, which simplified the manufacturing process by ensuring proper bonding between layers. The compliant electrode material consisted of carbon black powder (Vulcan XC72, Cabot Corporation, USA). The passive elastomeric layers were made of a soft silicone elastomer (TC-5005 A/B-C, BJB Enterprises Inc., USA), which was used with a content of softening agent C equal to 50 wt%. The passive elastomeric layers were produced by mould casting as films of different thickness, ranging from 2 to 4 mm. The different films were used to manufacture different samples of the bandage, in order to investigate how the electromechanical performance was affected by the thickness of the passive layers. Six wooden stiffening sticks, having a diameter of 2.5 mm each, were integrated within the outer passive layer, during its fabrication by mould casting, according to the layout shown in Figure 3.2. Electrical contacts for the electrodes were obtained by means of metal stripes integrated within the structure. Velcro stripes were glued at the two ends of the bandage, so as to secure it to the limb (Figure 3.2).

The overall manufacturing process consisted of the following steps. A single active layer with a thickness at rest of 2 mm was obtained by coupling together two unstretched 1 mm-thick VHB 4910 films. This was justified by preliminary experimental evidences, which had shown superior force generation capabilities from actuators featuring thicker active layers. The resulting film was then equi-biaxially prestretched by 300% and attached to a support frame. The use of that pre-strain was justified by its well-known beneficial effect in terms of electromechanical performance increase, as first reported by [26] and then explained in different ways by [34] and [53]. The prestretch caused a reduction of the thickness from 2 to 0.125 mm.
A first compliant electrode (250 mm x 120 mm) was then created by depositing an alcohol-based suspension of the carbon black powder on one of the surfaces of the active layer. Then, a metal stripe connector was attached to it. A second active layer was coupled to the first one, covering the electroded side. The outer surfaces of the two-layer structure were coated with the carbon black powder to obtain analogous compliant electrodes and were fitted with metal stripe connectors. In order to create the passive layers, the active layer sandwich was laid at the bottom of a mould and then coated with the silicone material in liquid form, which was poured into the mould. The mould was maintained horizontally for curing at room temperature for 24 hours. After curing, the obtained multi-layer structure was removed from the

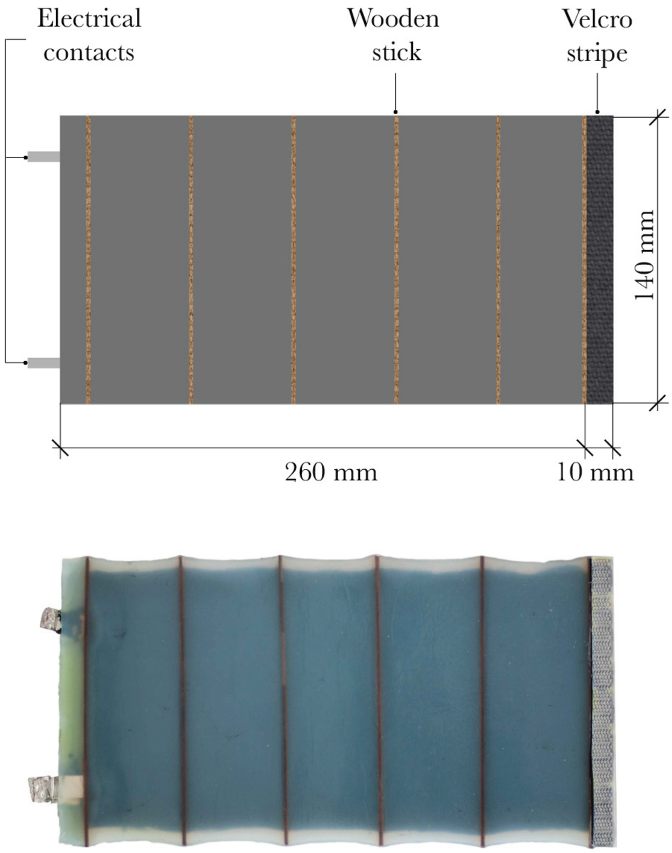

FIGURE 3.2: Schematic drawing (top) and picture (bottom) of a prototype active bandage.

mould and flipped over, and the same procedure was repeated in order to cast the second passive layer. During this process, six wooden sticks were also integrated on one side of the structure, by placing them on the surface of the active layer before the deposition of the silicone. The sticks allowed for holding the pre-stretch along one direction upon the removal of the bandage from the supporting frame. The resulting self-standing bandage acquired the shape visible in Figure 3.2. The extent of inevitable shrinking between two adjacent sticks depended on the passive layers thickness, according to the mechanical resistance offered by the passive coatings. Owing to that reason, it was not possible to obtain self-standing bandages with a passive layer thickness lower than 2 mm.

3.4 Testing of the prototype active bandages

In order to test the performance of the different prototype bandages, a chamber that mimicked the compliance of a human limb was assembled. It consisted of a soft tubular structure containing pressurized air, as shown in Figure 3.3a. It was constructed by coupling together two soft rubber membranes (model 4075 triaxial test rubber membrane, Wykeham Farrance, UK), having each a diameter of 70 mm and a thickness of 0.4 mm, and combining them with two rigid sealing plugs. The sealing plugs were connected one another by a rigid spacer, setting to 180 mm the distance between the two inner plugs edges. A manual pump, connected to one of the sealing plugs, allowed for pressurizing the air chamber. Pressure readings were taken from a digital pressure gauge (model Bit02B-2.5 bar, AEP Transducers, Italy), connected to the other sealing plug (Figure 3.3).

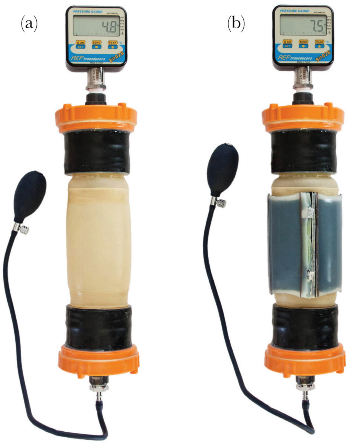

FIGURE 3.3: Testing of the prototype dynamic bandages: air chamber that mimicked the compliance of a human limb, without (a) and with (b) the bandage.

The bandage was secured (by means of the Velcro stripes) to the air chamber, such that the stiffening sticks were oriented axially (Figure 3.3b). The chamber pressure was initially set to P_0=7.5 kPa for each prototype bandage tested. Therefore, the different bandages reached different initial values of their diameter, according to the different values of their passive layer thickness (and, so, their stiffness). From this initial state, increasing voltages were applied, with steps of 500 V, until electrical breakdown of the bandage occurred. As a result of the radial actuation, the internal chamber pressure P_V reached a lower value, monitored with the pressure gauge. Results of the testing of three samples of the bandage with a passive layer thickness D_P of 2, 3 and 4 mm are presented in Figure 3.4.

The data show that 3 mm was an ‘optimum’ value, among those tested, for the passive layer thickness. In order to obtain an analytical description of the system, an axisymmetric model of the bandage based on finite electro-elasticity was developed as described in the following section.

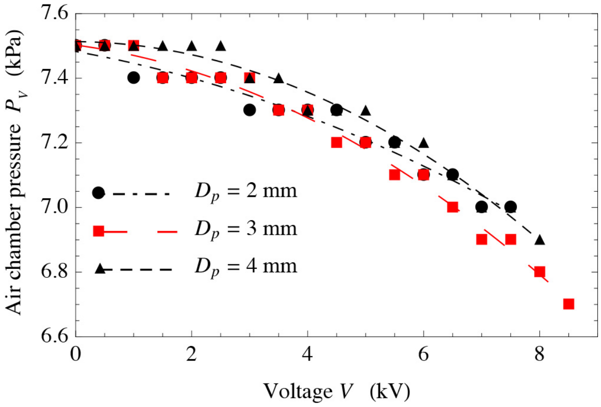

FIGURE 3.4: Electromechanical performance of three samples of bandages having a different initial thickness D_P of their passive layers. Quadratic fitting curves are used as a guide for the eye.

3.5 Analytical model of the active bandage

The model here developed neglects the viscoelastic behaviour of each layer and describes its nonlinear electromechanical properties using a Neo-Hookean hyper-electro-elastic representation. The model is developed for a central portion of the tubular structure, which was assumed to be sufficiently distant from the two ends of the tube to neglect any variation of pressure along the longitudinal coordinate z. Moreover, in consideration of the fact that the stiffening sticks constrain the longitudinal stretch to a fixed value, the length along the z-axis was considered constant (140 mm, see Figure 3.2). Therefore, the problem was studied assuming a plane strain condition, implying a longitudinal stretch λ_z=1 for the passive layers and λ_z=4 for the active ones.

3.5.1 Kinematics of the multilayer structure

To describe the geometry of the system, the three deformed configurations reported in Figure 3.5 were considered.

In the “initial state” B_b (Figure 3.5 top), the bandage is wrapped around the air chamber with a circumferential length at the interface of 260 mm. Here, the system is in equilibrium with an air chamber pressure P_b and a contact pressure between the bandage and the chamber’s rubber membrane P_{cb}. It is worth pointing out that when the bandage is applied to the chamber and the latter is pressurized, the azimuthal or hoop stress is distributed between the rubber membrane and the bandage, according to their stiffness. In this state B_b, which is reached when the planar bandage is bent to reach the cylindrical configuration, the length of the inner circumference of the passive layer p_1 was assumed to be equal the length (260 mm) of the unbent bandage (Figure 3.2). This way, the inner boundary of the layer p_1 has a hoop stretch $\lambda_{\theta b}$=1. In principle, it should be considered that, while bending the multilayer, a non-homogeneous deformation is imposed [54], which would induce

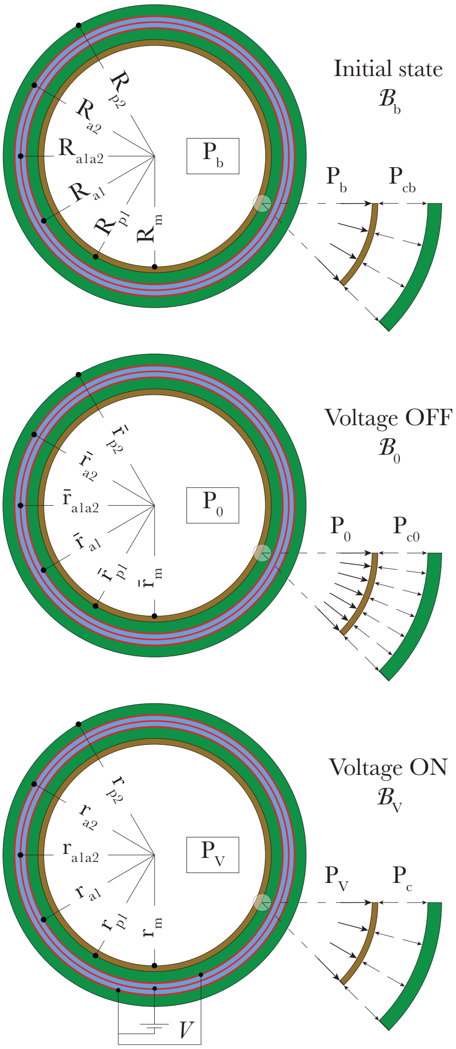
Initial state
$\mathcal{B}_b$
R_{p2}
R_{a2}
R_{a1a2}
R_{a1}
R_{p1}
R_m
P_b
P_b
P_{cb}
Voltage OFF
$\mathcal{B}_0$
$\bar{r}_{p2}$
$\bar{r}_{a2}$
$\bar{r}_{a1a2}$
$\bar{r}_{a1}$
$\bar{r}_{p1}$
$\bar{r}_m$
P_0
P_0
P_{c0}
Voltage ON
$\mathcal{B}_V$
r_{p2}
r_{a2}
r_{a1a2}
r_{a1}
r_{p1}
r_m
P_V
P_V
P_c
V

FIGURE 3.5: Schematic representation of the cross-section of the air chamber surrounded by the active bandage. (a) In the "initial state" B_b, the active bandage is secured around the rubber membrane of the chamber with an air chamber pressure P_b and a contact pressure P_{cb}, so that the bandage's inner radius R_{p1} is $\approx$ 40 mm (radial distances are denoted by the letter R), (b) In the "Voltage OFF" state B_0, the air chamber pressure is manually set to P_0=7.5 kPa, causing an expansion of the bandage (radial distances are denoted by $\bar{r}$). (c) Following the application of a voltage V, the system is switched to its"Voltage ON" state B_V, where the air chamber pressure decreases from P_0 to a lower value P_V and the contact pressure drops from P_{c0} to $P_c < P_{c0}$ (radial distances are denoted by the letter r).

a radius-dependent hoop stretch in the layers. However, due to the thinness of the strata, only the stretch of the midline of each layer $\lambda_{\theta b,lay}$ (where "lay" indicates the layer, namely $lay = m, p_1, a_1, a_2, p_2$) was considered in our model. A straightforward computation shows that for the active layers a_1, a_2 this hoop stretch ranges between 4.196 and 4.388 (as these layers are initially prestretched with a factor 4), while $\lambda_{\theta b,p_1}$ ($\lambda_{\theta b,p_2}$) ranges between 1.024 (1.075) and 1.046 (1.140). The stretch $\lambda_{\theta b,m}$ is assumed unitary. Table 3.1 reports the calculated hoop stretches.

	$D_p = 2mm$	$D_p = 3mm$	$D_p = 4mm$
$\lambda_{\theta b,p_1}$	1.024	1.035	1.046
$\lambda_{\theta b,a_1}$	4.196	4.284	4.376
$\lambda_{\theta b,a_2}$	4.208	4.296	4.388
$\lambda_{\theta b,p_2}$	1.075	1.108	1.140

TABLE 3.1: Values of the hoop stretch of the midline in the initial configuration B_b for each layer of the three samples of bandages tested in state B_b.

In the "Voltage OFF" state B_b (Figure 3.5 centre), the bandage is secured to the air chamber with a certain circumferential stretch, assigned when the air chamber pressure $P_0 > P_b$ is set to 7.5 kPa. In this state, the contact pressure between the rubber membrane and the active bandage is $P_{c0} > P_{cb}$. In the "Voltage ON" state B_V (Figure 3.5 bottom), a voltage V generates a radial expansion of the bandage, which behaves like a cylindrical DE actuator [55, 56]. The radial expansion causes an active reduction of both the chamber's internal pressure and the contact pressure applied to the chamber, respectively from P_0 to $P_V < P_0$ and from P_{c0} to $P_c < P_{c0}$. In this state, the hoop stretch in the generic layer $\lambda_{\theta,lay}(r)$is given by:

$$\lambda_{\theta lay}(r) = \frac{r}{R}\lambda_{\theta b,lay} = \frac{r}{\sqrt{R^2_{in,lay} + \lambda_z(r^2 - r^2_{lay})}}\lambda_{\theta b,lay}, \tag{3.1}$$

where $lay = m, p_1, a_1, a_2, p_2$ and $R_{in,lay}$ denotes the inner radius of layer "lay" in state B_b. In (3.1), the ratio r/R is the hoop stretch with respect to B_b, while $\lambda_{\theta b,lay}$ takes into account the deformation undergone by the multilayer in state B_b. The square root term is an alternative expression for the radius R, obtained by taking into account the constraint of incompressibility of the elastomeric material, i.e. $\lambda_r\lambda_z\lambda_\theta$=1, which is useful to compute the radial stretch λ_r recalling that λ_z=1.

3.5.2 Electro-mechanics of a single layer

In order to describe the overall behaviour of the multilayer, it is useful to recall the governing equations for a single layer in a cylindrical reference system. Let us assume that the current inner and outer radii of an DE cylindrical actuator are r_i and r_e, respectively, and that at the two cylindrical surfaces the radial tensile stresses $\sigma_r(r_i)$ and $\sigma_r(r_e)$ are applied. In addition, the surfaces are coated with perfectly stretchable electrodes subjected to a voltage V, which induces through the thickness a radial electric field $E(r) = E_r(r)$. An application of the Gauss' theorem at a generic radial distance within the dielectric provides a relation between E and the amount of charge

Q stored on one electrode:

$$E = \frac{Q}{2\pi r \lambda_z L \varepsilon}, \tag{3.2}$$

where $\varepsilon = \varepsilon_0 \varepsilon_r$ is the absolute dielectric permittivity of the elastomer.

By integrating (3.2) with respect to the radius while considering the well-known relation between the electric potential ϕ and electric field E for a cylindrical capacitor having an axial length L, we obtain the relation between Q and the applied voltage V:

$$V = \phi(r_i) - \phi(r_e) = \int_{r_i}^{r_e} -d\phi = \int_{r_i}^{r_e} E dr = \frac{Q}{2\pi\varepsilon\lambda_z L} \ln\frac{r_e}{r_i}, \tag{3.3}$$

so that

$$E = \frac{1}{r} V / \ln\frac{r_e}{r_i}. \tag{3.4}$$

The layer, which is incompressible, obeys an isotropic hyper-electro-elastic strain energy $W(\lambda_r, \lambda_\theta, \lambda_z, E)$. In this configuration, the constitutive equations (2.22) (2.23) and (2.24) can be written as:

$$D = -\frac{\partial W}{\partial E}, \tag{3.5}$$

$$\sigma_\theta - \sigma_r = \lambda_\theta \frac{\partial W}{\partial \lambda_\theta} - \lambda_r \frac{\partial W}{\partial \lambda_r} - DE, \tag{3.6}$$

$$\sigma_z - \sigma_r = \lambda_z \frac{\partial W}{\partial \lambda_z} - \lambda_r \frac{\partial W}{\partial \lambda_r} - DE, \tag{3.7}$$

where D is the electric displacement, which has only a radial component, according to (3.5). Under the action of an axisymmetric electromechanical loading, the equilibrium of each layer is governed, in terms of Cauchy total stress σ, by the following differential equation:

$$\frac{d\sigma_r}{dr} + \frac{\sigma_r - \sigma_\theta}{r} = 0. \tag{3.8}$$

Integration of (3.8) between r_i and r_e provides

$$\sigma_r(r_e) - \sigma_r(r_i) = \int_{r_i}^{r_e} \frac{\sigma_\theta - \sigma_r}{r} dr. \tag{3.9}$$

In this model, the extended neo-Hookean strain energy function (2.26)

$$W = \frac{1}{2}\mu(\lambda_r^2 + \lambda_\theta^2 + \lambda_z^2 - 3) - \frac{\varepsilon}{2}E^2, \tag{3.10}$$

was adopted to compare model predictions with experimental results. Therefore, the in plane constitutive equations for the layer specialise to:

$$D = -\frac{\partial W}{\partial E} = \varepsilon E, \tag{3.11}$$

$$\sigma_\theta - \sigma_r = \lambda_\theta \frac{\partial W}{\partial \lambda_\theta} - \lambda_r \frac{\partial W}{\partial \lambda_r} - DE = \mu(\lambda_\theta^2 - \lambda_\theta^{-2} - \lambda_z^{-2}) - \varepsilon E^2, \tag{3.12}$$

where it is clearly seen that (3.10) admits the classical linear relationship (3.11) among electric displacement and electric field. Eq. (3.7) can be employed to find σ_z at each point once σ_r has been computed. In addition, the pressure difference $\sigma_r(r_e) - \sigma_r(r_i)$ becomes

$$\sigma_r(r_e) - \sigma_r(r_i) = \int_{r_i}^{r_e} \frac{1}{r} \left[\mu \left(\lambda_\theta^2 - \lambda_\theta^{-2} \lambda_z^{-2} \right) - \varepsilon \left(\frac{1}{r} \frac{V}{\ln \frac{r_e}{r_i}} \right)^2 \right] dr. \tag{3.13}$$

It is worth pointing out that, while a closed form of the integral in (3.13) can be obtained, this will not be given here.

3.5.3 Voltage-pressure relationship for the multilayer bandage

The voltage pressure relationship for the bandage in state B_V can be obtained by imposing continuity of the radial stresses at the interface between two generic concentric layers and the following boundary conditions:

$$\sigma_r(r_m) = -P_V, \sigma_r(r_{p2}) = 0. \tag{3.14}$$

A repeated use of (3.13), where $V = 0$ in layers m, p_1 and p_2, yields

$$\begin{aligned} P_V = &+ \int_{r_m}^{r_{p_1}} \frac{\mu_m}{r} \left(\lambda_{\theta m}^2 - \lambda_{\theta m}^{-2} \lambda_{zm}^{-2} \right) dr \\ &+ \int_{r_{p_1}}^{r_{a_1}} \frac{\mu_{p_1}}{r} \left(\lambda_{\theta p_1}^2 - \lambda_{\theta p_1}^{-2} \lambda_{z p_1}^{-2} \right) dr \\ &+ \int_{r_{a_1}}^{r_{a_1 a_2}} \frac{1}{r} \left[\mu_{a_1} \left(\lambda_{\theta_{a_1}}^2 - \lambda_{\theta_{a_1}}^{-2} \lambda_{z_{a_1}}^{-2} \right) - \varepsilon \left(\frac{1}{r} \frac{V}{\ln \frac{r_{a_1 a_2}}{r_{a_1}}} \right)^2 \right] dr \\ &+ \int_{r_{a_1 a_2}}^{r_{a_2}} \frac{1}{r} \left[\mu_{a_2} \left(\lambda_{\theta_{a_2}}^2 - \lambda_{\theta_{a_2}}^{-2} \lambda_{z_{a_2}}^{-2} \right) - \varepsilon \left(\frac{1}{r} \frac{V}{\ln \frac{r_{a_2}}{r_{a_1 a_2}}} \right)^2 \right] dr \\ &+ \int_{r_{a_2}}^{r_{p_2}} \frac{\mu_{p_2}}{r} \left(\lambda_{\theta_{p_2}}^2 - \lambda_{\theta_{p_2}}^{-2} \lambda_{z_{p_2}}^{-2} \right) dr. \end{aligned} \tag{3.15}$$

Assuming that the product between the pressure P_V and the air volume Vol inside the chamber only depends on the mechanical path (i.e. assuming that the temperature is constant) and assuming no air leakage from the chamber, the ideal gas law gives

$$P_V = constant. \tag{3.16}$$

This condition allows for relating the inner radius of the rubber membrane r_m to the pressure P_V:

$$P_0 \bar{r}_m^2 = P_V r_m^2. \tag{3.17}$$

By substituting (3.17) into (3.15), a relation between the air chamber pressure P_0 and the inner radius of the rubber membrane rm is provided, once the driving voltage V is assigned:

$$\begin{aligned}
\frac{\bar{r}_m^2}{r_m^2} P_0 = &+ \int_{r_m}^{r_{p_1}} \frac{\mu_m}{r} \left(\lambda_{\theta m}^2 - \lambda_{\theta m}^{-2}\lambda_{zm}^{-2}\right) dr \\
&+ \int_{r_{p_1}}^{r_{a_1}} \frac{\mu_{p_1}}{r} \left(\lambda_{\theta p_1}^2 - \lambda_{\theta p_1}^{-2}\lambda_{z p_1}^{-2}\right) dr \\
&+ \int_{r_{a_1}}^{r_{a_1 a_2}} \frac{1}{r} \left[\mu_{a_1}\left(\lambda_{\theta_{a_1}}^2 - \lambda_{\theta_{a_1}}^{-2}\lambda_{z_{a_1}}^{-2}\right) - \varepsilon\left(\frac{1}{r}\frac{V}{\ln\frac{r_{a_1 a_2}}{r_{a_1}}}\right)^2\right] dr \\
&+ \int_{r_{a_1 a_2}}^{r_{a_2}} \frac{1}{r} \left[\mu_{a_2}\left(\lambda_{\theta_{a_2}}^2 - \lambda_{\theta_{a_2}}^{-2}\lambda_{z_{a_2}}^{-2}\right) - \varepsilon\left(\frac{1}{r}\frac{V}{\ln\frac{r_{a_2}}{r_{a_1 a_2}}}\right)^2\right] dr \\
&+ \int_{r_{a_2}}^{r_{p_2}} \frac{\mu_{p_2}}{r} \left(\lambda_{\theta_{p_2}}^2 - \lambda_{\theta_{p_2}}^{-2}\lambda_{z_{p_2}}^{-2}\right) dr.
\end{aligned} \tag{3.18}$$

In order to calculate the contact pressure P_c it is important to define the pressure sustained by the rubber membrane of the air chamber P_m. Considering equation (3.18), for a certain value of the radius r_m the pressure P_m is given by the first term on the right-hand side of (3.15):

$$P_m = \int_{r_m}^{r_{p_1}} \frac{\mu_m}{r} \left(\lambda_{\theta m}^2 - \lambda_{\theta m}^{-2}\lambda_{zm}^{-2}\right) dr \tag{3.19}$$

In the state B_V, the contact pressure between the rubber membrane and the bandage is obtained by subtracting P_m from the air chamber pressure P_V:

$$P_c = P_V - P_m \tag{3.20}$$

In order to quantify the contact pressure P_c it is necessary to know the shear moduli of the three materials (silicone, acrylic and rubber). For the passive layers, the quasi-static value 16 kPa experimentally determined by [57] was adopted for both the moduli μ_{p_1} and μ_{p_2}. For the acrylic elastomer, the value 73 kPa measured by [58] was used for both the moduli μ_{a_1} and μ_{a_2}. For the rubber membrane, the value 666 kPa reported in [59] was employed for the modulus μ_m.

3.6 Model validation: comparison between experimental data and model predictions

As a validation of the model, Figure 3.6 presents a comparison between experimental data and model predictions.

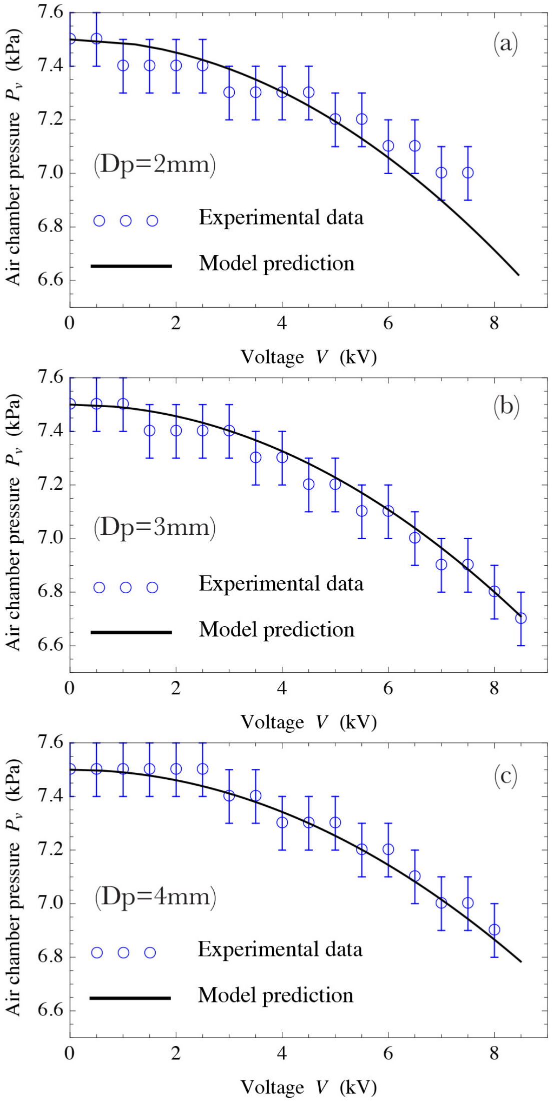

FIGURE 3.6: Dependence of the air chamber pressure P_V on the applied voltage V: comparison between experimental data and model-based predictions, for the three types of prototype bandages having different thickness D_p of their passive layers.

The comparison shows that the model accuracy increases with the thickness of the passive layer. This outcome may be explained in terms of the constraining effect introduced by the stiffening sticks. Indeed, for the sample with 2 mm-thick passive layers the wooden sticks were closer to the electroactive layer, inducing local stress concentration and, so, limiting actuation. As in the model the presence of the stiffeners was ignored, these effects were not considered. This might explain the discrepancy evident in Figure 3.6a, especially at high voltages. Conversely, for the other extreme case, i.e. for the 4 mm-thick passive layers, the stiffening sticks were significantly distant from the electroactive layer, such that stress concentration and expansion restraining were significantly reduced. This might justify the accurate match between experimental measurements and model predictions evident from Figure 3.6c.

3.7 Model predictions: contact pressure

The validated theoretical framework described above is particularly useful to compute the contact pressure P_c exchanged between the air chamber and the bandage in the "Voltage ON" state. This is an important variable as, with reference to the intended application, it represents the pressure that would actually be exerted by the bandage on the surface of the user. Figure 3.7 presents the estimates for the three prototype bandages, while Figure 3.8 compares the contact pressure variation ΔP_c as a function of the applied voltage V for bandages having a passive layer's thickness from 0 to 4 mm and a length of the inner circumference of the passive layer p_1 equal to L=260 mm.

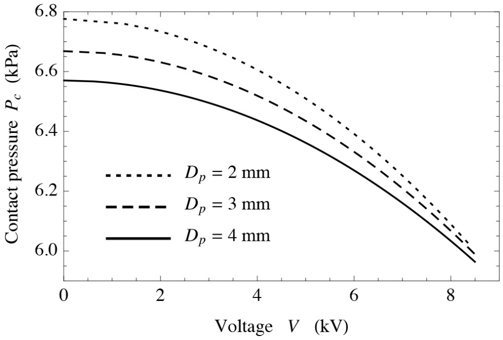

FIGURE 3.7: Dependence of the contact pressure P_c on the applied voltage V for the three types of prototype bandages having different thickness D_p of their passive layers.

Figure 3.7 shows the contact pressure-voltage curves for the three prototypes. The curves intersect close to the experimental breakdown limit. For D_p=2, 3 and 4 mm the estimated initial contact pressure was 6.78, 6.67 and 6.57 kPa, respectively, and upon actuation at 8 kV the pressure respectively dropped to 6.09, 6.06 and 6.03 kPa, corresponding to a reduction of 10.2%, 9.15% and 8.2%. These estimates indicate that the contact pressure change was highest for the sample featuring the thinnest passive layers. The fact that the model predicts a higher performance for a lower thickness of the passive layers is also evident from Figure 3.7, which plots the pressure variation also for values of thickness not tested experimentally. So, according to the model,

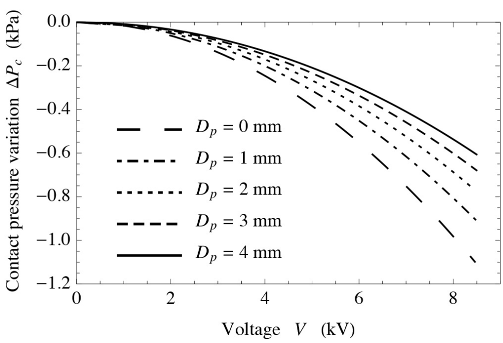

FIGURE 3.8: Variation of the contact pressure between the air chamber and the bandage, as estimated from the model for bandages having a different thickness D_p of the passive layers.

the highest performance would be achieved without any passive layer. This outcome is due to the fact that the presence of the stiffeners was neglected by the simplified model. Therefore, further developments of the model are needed in order to take in account the effect of the stiffeners. By taking into account the stiffeners, it is reasonable to expect an optimum value of the passive layer thickness, which should maximise the contact pressure variation.

3.8 Future developments

3.8.1 Improvement of the electromechanical properties

In order to study the influence of the number of electroactive layers on the actuator's ability to vary the contact pressure, the simulations shown in Figure 3.9 were performed. They refer to bandages having D_p=2 mm and an increasing number of active layers with properties identical to those considered above. The simulations show that the higher the number of active layers, the larger is the contact pressure variation, although it tends to saturate. This outcome is plausible as it is consistent with the intuitive view that, as the total number of layers increases, any constraint at the surfaces of the cylindrical stack tends to have a vanishing influence on the "central" layers that are "sufficiently distant" from the ends. Moreover, as the total number of layers increases, the number of the "central" layers unaffected by the constraint increases, such that the unaffected portion of stack is larger. So, as the stack grows up, it gets closer to an ideal infinitely thick structure, whose generated force is not affected by any constraint at the two ends and by the number of layers: it would generate the same force as that generated by a single ideal unloaded layer. Knowing that such a saturation effect exists is useful for the design of multi-layered electroactive bandages.

Figure 3.10 visualises the saturation trend of the contact pressure variation $\Delta P_c / P_c$ for bandages having up to 10 active layers and with V=8 kV.

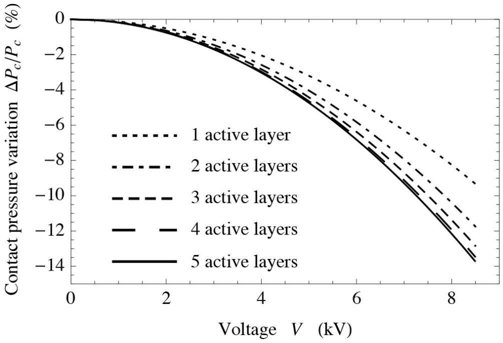

FIGURE 3.9: Relative variation of the contact pressure (with respect to its initial value) between the air chamber and the bandage, as estimated from the model for five types of prototype bandages having an increasing number of active layers and a constant thickness of the passive layers D_p= 2 mm.

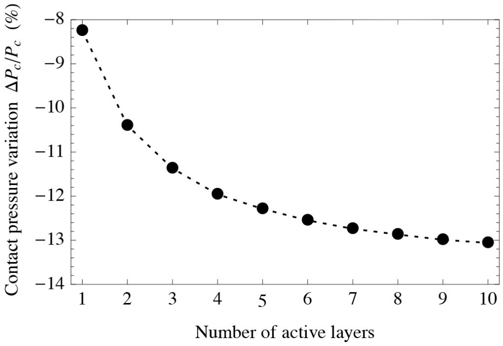

FIGURE 3.10: Relative variation of the contact pressure (with respect to its initial value) at V=8 kV between the air chamber and the bandage, as estimated from the model for ten samples of prototype bandage having an increasing number of active layers and a constant thickness of the passive layers D_p= 2 mm.

3.8.2 Improvements of the model

To improve the accuracy of the model, the presence of the stiffening sticks should be taken into account. Such a detailed modelling was beyond the aims of this first investigation and should be tackled in future studies.

3.8.3 High-voltage driving: viability and challenges

These prototype bandages required driving voltages of several kilovolts. In terms of electrical safety, dealing with such high voltages is clearly not desirable. However, this drawback is mitigated not only by the use of insulating layers, but, especially, by the fact that there's no need for a high driving current (and, so, power). Indeed, electrically the bandage is a capacitive load, which allows for using low-power, electrically safe sources. The low power requirement favours also the technical viability of high voltage driving. Indeed, high-voltage multipliers with low-power and compact size (volume of the order of 1 cm^3 or less) are commercially available such as those produced by EMCO High Voltage [60]. This allows for implementations of battery-powered portable and compact systems. Nevertheless, the need for high-voltage circuitry introduces a significant limitation in terms of costs. This drawback, which is characteristic for the whole field of the DE transducers today, is focusing efforts to produce films that can be driven at lower voltages. Besides fundamental attempts to synthesize new elastomers with higher dielectric constant [61, 62], the most readily achievable solution in the short term is represented by thin-film processing of conventional materials [35]. Indeed, several groups have already demonstrated DE transducers with voltages reduced to a few hundred volts [63], thus anticipating that in the near future the DE technology will likely adopt the standard and cheaper circuitry used today for piezoelectric drives.

3.9 Conclusions

We presented here a multilayer active bandage made of dielectric elastomer actuators. This study showed the following main evidences. First, the passive layers coating the bandage have a function that goes beyond those of electrical protection and mechanical impedance matching. Indeed, as shown by both the experiments and analytical model, they play a key role for an effective transmission of actuation from the active layers to the load. The second evidence is that by adopting the multilayer design reported above and different constitutive materials, it was possible to achieve a higher contact pressure drop as compared to previous studies. Indeed, the best performing active bandage prototype reported in [49] allowed for achieving an initial contact pressure of 2.87 kPa and a drop to 2.73 kPa, corresponding to a 5.2% decrease, for a voltage of 11.3 kV; in comparison, the active bandage prototypes presented here allowed for contact pressures ranging from 6.57 kPa to 6.78 kPa and, respectively, pressure drops from 8.2% to 10.2%, for a voltage of 8.5 kV. The third evidence is that, according to the new design, the existence of an optimum value of the passive layer thickness is expected. However, such value could not be precisely identified here, owing to the need for advanced models able to capture the complexity of the constraints introduced by the stiffening elements. The fourth evidence is that, for a given passive layer's thickness, the variation of contact pressure increases with the number of active layers, with a saturation trend. These outcomes, together with the theoretical framework specifically developed for the case of prestretched multiple layers, are expected to serve as help for future improvements of the design, implementation and manufacturing process of prestretched multi-layer electroactive bandages.

Chapter 4

Hydrostatically Coupled Dielectric Elastomer Actuator

This chapter presents an upgraded design of the existing push-pull Hydrostatically Coupled Dielectric Elastomer Actuator (HC-DEA) for use in the field of soft manipulators. The new design has segmented electrodes, which stand as four independent elements on the active membrane of the actuator. When properly operated, the actuator can generate both out of plane and in plane motions resulting in a multi-degrees of freedom soft actuator able to exert both normal pushes (like a traditional HC-DEA) and tangential thrusts. This novel design makes the actuator suitable for delicate flat object transportation. In order to use the actuator in soft systems, we experimentally characterized its electromechanical transduction and modeled its contact mechanics. Finally, we show that the proposed actuator can be employed as a modular unit to develop active surfaces for flat object roto-translation.

This work has been published in the peer reviewed journal article:

- De Acutis, A., Calabrese, L., Bau, A., Tincani, V., Pugno, N. M., Bicchi, A. and De Rossi, D. E. (2018). Design and proof of concept for multi degree of freedom hydrostatically coupled dielectric elastomer actuators with roto-translational kinematics for object handling. *Smart Materials and Structures*, 27(7), 074005.

4.1 Introduction

Material handling (e.g. grasping, transportation and sorting) is very important in all productive activities, particularly in industrial fields and in robotic industry worldwide. Usually, in manufacturing facilities, part feeders and conveyor systems together with grippers and manipulators are used for picking, sorting and moving items between specific locations [64]. All these systems are required to be effective, robust, fast and reliable in order to guarantee a rapid order fulfillment; yet, size and structural rigidity often limit their use, especially when the handling of fragile and/or delicate objects is required [65] or when frequent changes of picking and delivery locations occur.

To address the issue of fragile and delicate object handling, the growing research field of soft robotics has provided many devices that are based upon different concepts with respect to the more traditional rigid robotics. They rely on soft and compliant actuation systems such as pneumatic drives and variable stiffness actuators, on intrinsically adaptive structures that feature under-actuated mechanism and on the employment of soft materials that range from simply deformable to smart engineered materials (such as shape memory alloy and electro active polymers) [66, 67].

By exploiting these principles, many soft grippers and manipulators capable of stably and gently handling unknown shaped objects have been designed and reported in literature. One of the most representative soft gripper is the Universal Gripper, which stands out for its simplicity and adaptability to the shape of the grasped objects [68]. Such gripper is composed of granular material encased in a soft and elastic membrane that allows for deforming and adapting to the shape of the objects as it is pushed against them. Making a positive or negative pressure inside the membrane the gripper can quickly grip and release a broad range of objects of different shapes. The adaptability of the Universal Gripper allows for distributing the grasping force over a larger surface of contact than a not adaptive soft gripper does. Furthermore, by tuning the intensity of the pressure, it allows to modulate the grasping force making it particularly suitable also for delicate parts [68]. All these features contributed to make it a very successful commercial product of the last years demonstrating how much desirable those characteristics are for industry. Although in the last decade many soft grippers have been designed, on the other hand, the use of soft-bodied conveyors or feeders for the transportation of delicate objects rather than the traditional rigid-bodied ones is still a rather unexplored field.

Indeed, the soft-bodied conveyors or feeders reported in literature are mostly shaped as pneumatically deformable soft surfaces capable of moving objects on a horizontal plane. In this regard, key examples are the fluid-based systems such as the "Festo Wavehandling" platform [69], which features a soft surface actuated by a pneumatic system that enables for the displacement of round objects through a wave-like motion, and the soft platform developed by Stommel et al. [70], featuring a pneumatically-induced peristaltic motion enabling it for ovine offal sorting. Another interesting device for material handling is described in the work of Mosadegh et al. [71] who presented a reconfigurable manifold designed for controlling pneumatically actuated soft machines, based on a computer-controlled braille display. Such device relies on a compact array of piezoelectric actuators, and on an interchangeable micro pneumatic system, allowing it for controlling a large number of independent outputs. Since these systems are properly designed for specific purposes their usage is limited only to round objects with approximately spherical or, at most, cylindrical shape.

To address this limitation, Deng et al. [72] proposed a pneumatic machine table for manipulation of delicate objects inspired by caterpillar locomotion. This machine table successfully tackled the challenge of displacing flat objects like an iPhone in both translational and rotational direction on a plane, thanks to a peculiar shape and actuation control logic of its inflatable chambers, driven by an external pumping system. Despite these relevant attempts to improve the performance and usability of these systems, pneumatic-based machines still require a complex design, a cumbersome and expensive external pneumatic hardware (e.g. valves, pumps and compressors) and they also feature a high energy consumption, thus making them unsuitable in many applications [4].

In order to exploit a more convenient actuation principle, Wang et al. made use of the Dielectric Elastomer (DE) actuation technology to develop a soft-wave handling system [65], featuring a matrix of 16 air-filled bubble-like actuators similar to the fluid-filled push-pull Hydrostatically Coupled Dielectric Elastomer Actuators (HC-DEAs) first presented by Carpi et al. [28]. It is worth to point out that such bubble-like actuators are built by coupling two pre-stretched membranes enclosing a finite volume of air or fluid sealed upon manufacturing; therefore they do not require any pumping system for their actuation. However, since such devices work by design only in push and pull modes [28], when embedded in a soft platform, they are only capable to trigger the rolling of round objects placed on the platform's surface (as shown in [65]) but are unsuitable to induce the in-plane displacement of any object that can not roll, such as a flat object, since they are not capable of generating any tangent thrust but only a normal one.

Aiming at overcoming this limitation, it is here presented a new concept of HC-DEA with independent segmented electrodes on the active membrane (as better described in the following), which enables the actuator to generate both normal and tangent thrusts on objects placed in contact with its surface. Although the use of segmented electrodes in dielectric elastomer actuators was already reported to be effective for the conical DE-based multi-DoF actuator, presented by Conn and Rossiter [73], to the best of the author's knowledge, it has never been used for HC-DEA systems. Indeed, this simple change in the design of the electrodes results in a significant enhancement of the HC-DEA capabilities, making it able to generate both an out of plane action (push-pull behavior) and an in-plane one. In this way the actuator can operate following infinite trajectories in the space, therefore we called it multi-Degree of Freedom (multi-DoF) HC-DEA. Thanks to the ability to exert both normal and tangential thrusts in any direction in a plane, the multi-DoF HC-DEA enables a variety of possible applications in the field of soft manipulation. In particular, with this work we intend to demonstrate the possibility of using it as a building block of a modular soft platform aimed at handling objects. Moreover, since each actuator of the platform can be independently controlled by an electric signal, the result is an easily reprogrammable and reconfigurable soft surface composed by a plane matrix of actuators allowing for both round and flat objects handling. The proposed multi-DoF HC-DEA was investigated in terms of electromechanical transduction performance and contact mechanics. Actuation experiments were also carried out, thus proving the capacity of an array of multi-DoF HC-DEAs to roto-translate flat objects on a horizontal surface.

4.2 Conceptual design and working principle of the multi-DoF HC-DEA

4.2.1 Key idea

Within the field of DE transducers, HC-DEAs are of particular interest nowadays. As described in [28], a conventional HC-DEA consists of two pre-stretched membranes coupled together by a fixed volume of an incompressible fluid (Figure 4.1).

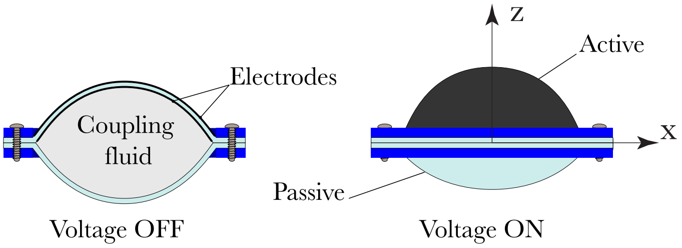

FIGURE 4.1: A push-pull HC-DEA. In rest state (left) and in active state (right).

The upper membrane of the actuator is coated on the inner and the outer sides with compliant electrodes, which form a flexible DE capacitor. Due to the pre-stretch of the membranes, the coupling fluid is sealed between the membranes with an initial pressure. Such pressure keeps the membranes stretched, enhancing the dielectric breakdown strength [74] and thus the electromechanical transduction capability of the actuator. When a voltage difference is applied to the electrodes, an electrostatic pressure is generated between them, thereby reducing the thickness and expanding the area of the elastomeric material due to its incompressibility [75, 13, 26]. Accordingly, the active membrane expands outward, while the passive membrane is dragged inward, driven by the hydrostatic transmission of the intermediate fluid. Therefore, a conventional HC-DEA results in a push-pull device whose stroke depends on the applied voltage. Considering the active membrane's apical point as a reference, due to axis-symmetry upon voltage application, the point is displaced along the out-of-plane (z-axis) direction only, and therefore no in-plane displacement is allowed. We can thus refer to it as a one-degree of freedom actuator, which exerts only a normal force on an object in contact with its surface.

In order to enhance the functionality of the actuator with an in-plane displacement capability, it is here presented an upgrade that features a particular electrode pattern (Figure 4.2). The design of the new electrodes, which stand as four independent quarter-circles within the active membrane, enables a tridimensional trajectory of the apical point to be generated, as the driving voltage V is applied. This new feature distinguishes the proposed actuator from the state of the art by allowing its active membrane for generating both a normal and a tangent thrust on the object to be moved. Indeed, when all the electrodes are activated the actuator behaves like a traditional push-pull HC-DEA, showing an axisymmetric out of plane deformation. On the other hand, when a voltage V is applied to two adjacent electrodes, for instance on the right side as depicted in Figure 4.2, only that part of the active membrane expands as a result of the applied voltage. Thus, this deformed configuration is not axisymmetric and the apical point moves to the left in addition to an out of plane displacement. In this fashion, the actuator is able to exert both a normal and a tangential (leftward in this example) thrust.

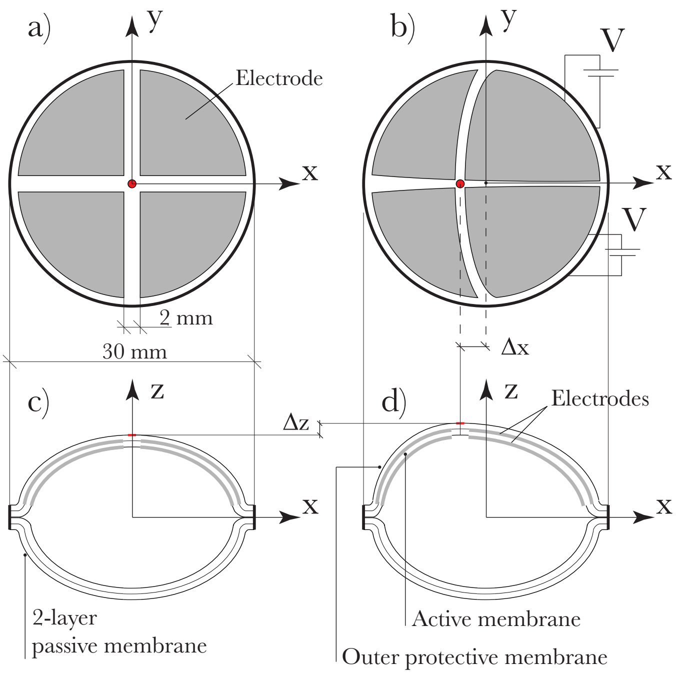

FIGURE 4.2: Top view of the multi-DoF HC-DEA in its rest state (a) where the four independent electrodes enable the tridimensional displacement of the actuator's apical point. For example, when a driving voltage V is applied to the two electrodes on the right-hand side, a displacement is triggered along the x-axis coupled to a displacement along the z-axis (b). The electrode position within the coupled layers that constitute the active membrane of the actuator is also highlighted in the x-z section planes (c) and (d).

4.2.2 Manufacturing

The actuator was fabricated with an acrylic elastomer film (VHB 4910, 3M, USA) for both the active and the passive membranes, carbon conductive grease (Carbon Conductive Grease 846, M.G. Chemicals, Canada) for the electrodes and silicone grease (8462, M.G. Chemicals, Canada) for the coupling fluid. In order to isolate the electrodes from the external environment, thereby preventing possible damage occurring from the contact with objects, the active membrane was coupled with a second outer insulating VHB film, as shown in Figure 4.2. In order to obtain an actuator with a symmetrical shape at rest, the same double layer configuration was used for the manufacturing of the passive membrane.

The fabrication process of the actuator is described in Figure 4.3.

In particular, Figure 4.3a describes the fabrication procedure of both the active and the passive membranes, in which two layers of VHB 4910 elastomer, each with an initial thickness of 1 mm, were equi-biaxially pre-stretched by 300% and secured

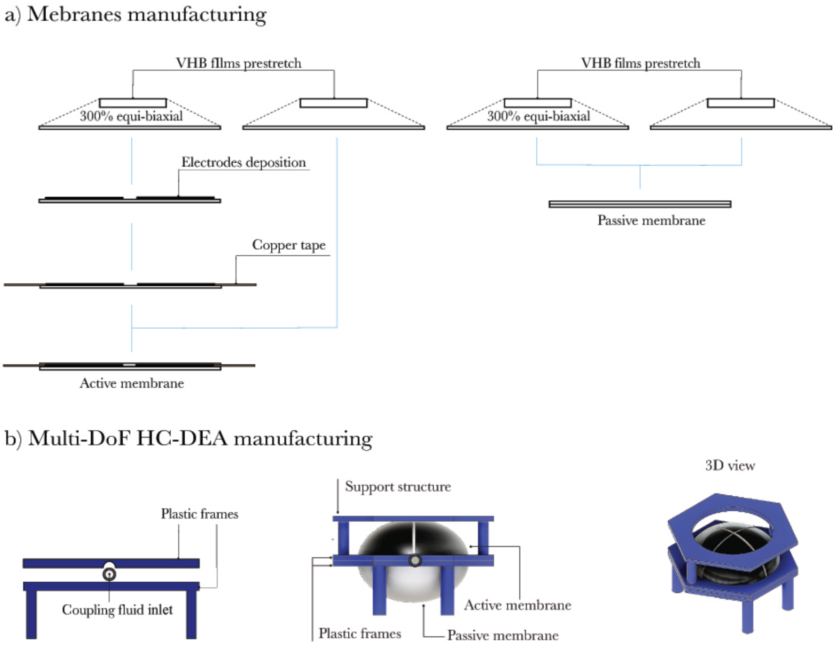
a) Mebranes manufacturing
VHB fllms prestretch
300% equi-biaxial
VHB films prestretch
300% equi-biaxial
Electrodes deposition
Passive membrane
Copper tape
Active membrane
b) Multi-DoF HC-DEA manufacturing
3D view
Support structure
Plastic frames
Coupling fluid inlet
Active membrane
Plastic frames
Passive membrane

FIGURE 4.3: Schematic representation of the manufacturing process of the actuator. Fabrication procedure of both the active and the passive membranes (a), assembly of the actuator's components (b).

to individual support frames. Due to the incompressibility of the material, the surface expansion of each layer, induced upon prestretch, resulted in a thickness reduction from the original thickness of 1 mm to 62.5 μm. Carbon grease electrodes were smeared with a brush and a stencil on both sides of the first layer of the active membrane. Thanks to the high adhesive properties of the VHB elastomer, this first layer was coupled to the second VHB layer forming a perfect bonding on the surfaces not covered by the electrodes. Copper tape was used for connecting the electrodes to the power source. The same procedure was repeated for the fabrication of the double layer passive membrane, except for the phase of the electrode deposition. The active and passive membranes were then coupled together by means of two 3D printed plastic frames (see Figure 4.3b), and filled with a volume of silicone grease (8462, M.G. Chemicals, Canada). The grease was inserted using a syringe through a silicone hose placed between the membranes and secured to the plastic frames. Each actuator resulted in a bubble-like shaped structure filled with 7 ml of coupling fluid, thus presenting a 30 mm diameter measured in relation to the horizontal plane of symmetry and a height of the apical point of 10 mm from the same plane. The driving voltage V was provided to each electrode pair by thin copper strips with negligible thickness and stiffness, placed in direct contact with the electrodes. In order for the multi-DoF HC-DEA to perform object displacement, the actuator was enclosed in the support structure represented in Figure 4.3b. The structure provides a flat top surface to support the objects to be displaced, and features a 20 mm diameter hole through which the actuator reaches the contact with the object upon activation performing the actuation cycle described in the following.

4.2.3 Actuation cycle

The actuation cycle adopted to enable the object to slide on the support surface is described in Figure 4.4. The cycle is composed of four steps, namely A, B, C and D, specifically designed to trigger the object to slide along one direction of the plane (with reference to Figure 4.2 in this case along the x-axis from left to right).

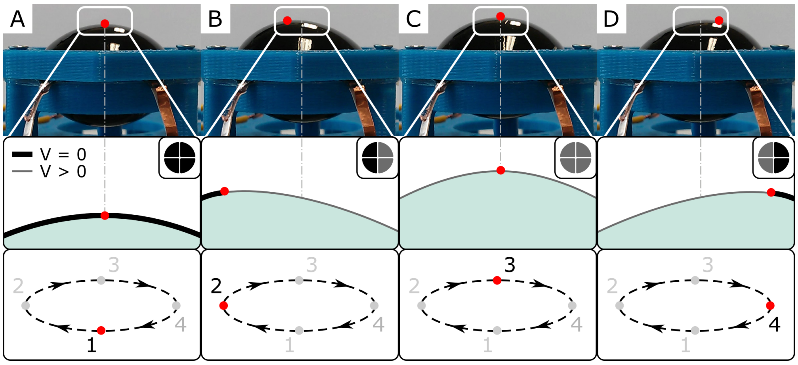

FIGURE 4.4: Actuation cycle used to induce the unidirectional motion of a flat object. The first row shows the pictures of the multi-DoF HC-DEA in each of the four steps of the actuation cycle (namely A, B, C and D), with its apical point identified by a red marker. A magnification of the voltage-induced deformation is shown in the second row, where the active membrane is represented by both the grey line $V > 0$ and by the grey electrodes drawn in the logo (top right corner). The passive part is represented by the black bold line $V = 0$ and by the black electrodes. The last row highlights the position of the apical point for each step in the cycle.

At the beginning of the cycle, see Figure 4.4a, the active membrane is in its rest state: no voltage is applied to the four electrodes of the actuator so that, when it is enclosed in the support structure, its apical point is just below the top surface of the support structure in incipient contact with the object. In the second step, described in Figure 4.4b, the actuator makes contact with the object thanks to the application of a driving voltage $V = 3.5$ kV to the two electrodes on the right side, which generates both a vertical and a horizontal displacement of the apical point. Figure 4.4c shows the third step of the cycle, where the driving voltage is applied to all four electrodes. During the transition between step B and C, the object can be lifted and displaced rightward from its original position. From this condition, in the last step of the cycle, see Figure 4.4d, the voltage on the right side electrodes is switched off, inducing a further horizontal shift of the object and a drop in the vertical height to the final position. In this fashion, by repeating the actuation cycle a proper number of times, it is possible to achieve any desired horizontal displacement as sum of the displacement generated by one cycle.

It is worth to point out that, the same actuation cycle can be used to trigger the sliding of the object along the y-axis, simply by activating the two couples of electrodes along that direction. Finally, each electrode in the multi-DoF HC-DEA can be activated individually, by different voltage signals, thus enabling the actuator to follow infinite trajectories.

4.3 Mechanical interaction between the multi-DoF HC-DEA and objects

During the actuation cycle, the actuator reaches the contact with the object and moves it on the horizontal plane thanks to the friction force generated through the contact area. If no slide occurs, according to the Coulomb friction model, the magnitude of the friction force is a function of both the normal force and the static friction coefficient. Therefore, in order to calculate the friction force generated on the object at a given voltage V it is important to know the normal force as function of the driving voltage V and to identify the value of the static friction coefficient for the object to be moved. For this reason, we experimentally measured the static friction coefficient between the active membrane of the actuator and four surfaces of different materials. Also, a test was carried out to identify the relation between the applied voltage and the normal blocking force exerted by the actuator. Eventually, the actuator was characterized as soft manipulator in terms of the relation between a geometrical parameter of the contact area and the normal blocking force and compared with robotic soft fingers.

4.3.1 Measurement of the static friction coefficient

This subsection reports the measurements performed to calculate the static friction coefficient occurring between the surface of the actuator and four flat objects made of plastic, aluminum, plywood and rigid cardboard. In performing the measurements, the active membrane of the actuator was dusted with talcum powder in order to prevent pernicious adhesive effects (as required in the usual operational condition). A conceptual scheme of the experimental set-up carried out to measure the static friction coefficient between the multi-DoF HC-DEA and the material samples tested is described in Figure 4.5. The test procedure is as follows. After securing the multi-DoF HC-DEA on a motorized linear carrier, which allowed for a translation along a horizontal axis, the first object was glued to a tri-axial ATI Nano 17 force sensor located on a second linear stage operating along a vertical axis over the actuator. Thanks to the linear stage, the sensor and the object were lowered until the object made contact with the actuator's active membrane. After setting an initial normal force of 0.1 N, the horizontal linear stage was activated with a velocity of 0.5 mm/s. Using the sensor to record both the normal force N and the tangential force F_f at the time of incipient sliding, the static friction coefficient $\mu = F_f/N$ was calculated for each specimen tested, and reported in Table 4.1.

These high values of the static friction coefficient μ allow the actuator to apply relatively high tangent forces on the object to be moved. Therefore, the actuator can operate with a gentle touch that makes it suitable for the displacement of delicate objects as better described in the following.

Material	Static friction coefficient μ
ABS plastic	0.63
Aluminium	0.72
Cardboard	0.76
Plywood	0.81

TABLE 4.1: Values of the static friction coefficient measured for different materials.

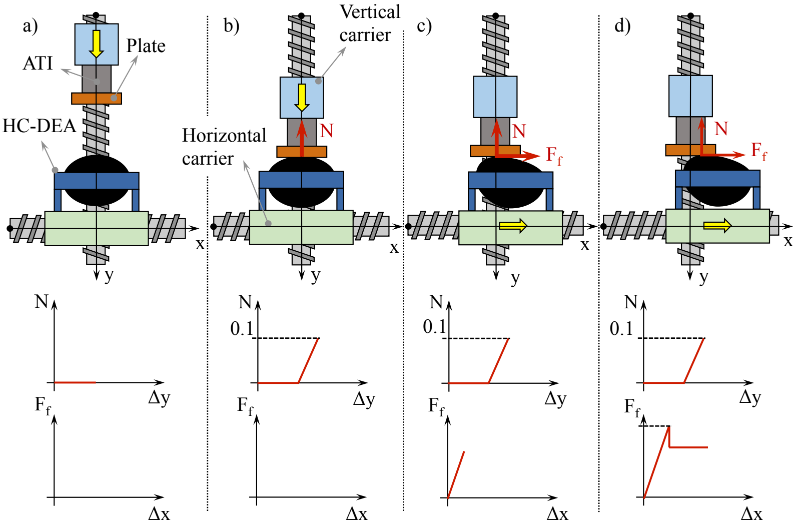

FIGURE 4.5: Conceptual scheme of the experimental set-up carried out to measure the static friction coefficient between the HC-DEA and diverse materials. In the picture, the execution of the experiment is broken down into four phases. Each phase is furnished with a graph of the normal and tangential force as functions of the displacement Δx and Δy of the carriers with respect to their location at the first phase: (a) the vertical carrier, on which a 6-axis ATI-Nano force/torque sensor and a plate of an established material are mounted, start moving down along the y-axis; (b) the plate contacts the HC-DEA and the descent of the carrier stops when a normal force N of 0.1 N is reached; (c) after N reaches 0.1 N, the horizontal carrier moves along the x-axis at a constant velocity of 0.5mm/s. A tangential force F_f arises on the system composed of the plate and the ATI sensor through the contact area at the apical point of the HC-DEA which, in this stage, does not move with respect to the plate; (d) as the horizontal carrier moves rightwards, the tangential force increases until it reaches a peak value when the contact area is on the verge of moving. After the peak value, that is the maximum static friction force we seek, the contact area translates rightwards and F_f slightly decreases at the value of the kinetic friction force.

4.3.2 Electro-mechanical performance

During phases B, C and D in the actuation cycle (Figure 4.4), the active surface of the multi-DoF HC-DEA makes contact with the object and generates both normal and tangent forces. By modelling the pre-slide regime with the Coulomb friction model we obtain:

$$F_f \leq \mu N, \tag{4.1}$$

where F_f is the friction force at the interface object-actuator, μ is the static friction coefficient and N is the normal force at the interface object-actuator. Since the deformation of the multi-DoF HC-DEA is voltage dependent, the resulting normal and tangent blocking forces are functions of the voltage amplitude V. In order to identify such relations, an actuation test was performed with a double column dynamometer (Z005, Zwick Roell, Germany) featuring a measure precision of 0.001 N. Figure 4.6 shows the experimental setup.

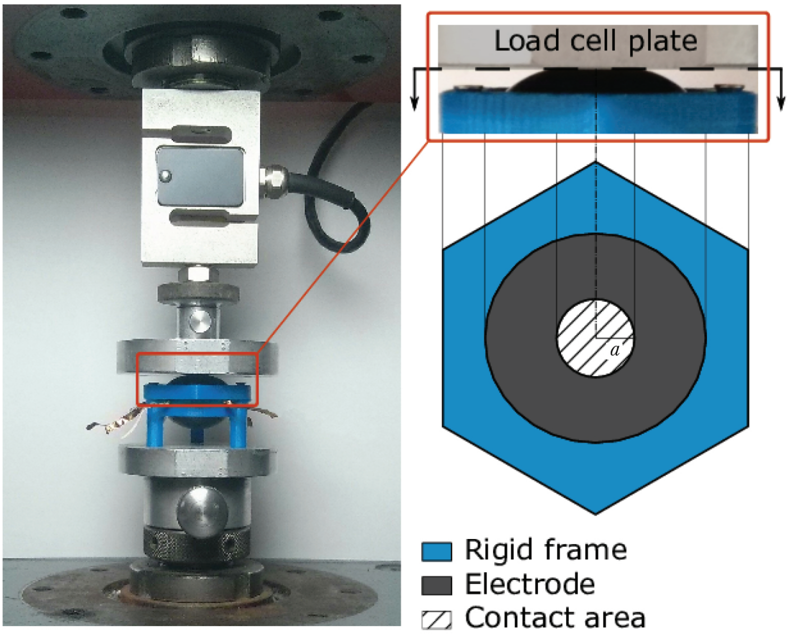

FIGURE 4.6: Compression tests of the actuation unit: experimental set-up. The compression tests of the actuator were performed with a uniaxial testing machine (left) equipped with a load cell for force measurements. The contact area was approximated with a circle of radius a (right).

The test procedure was as follows: 1) the multi-DoF HC-DEA actuator was placed on the horizontal surface of the uniaxial testing machine; 2) the load cell plate was lowered until an incipient contact with the actuator occurred; 3) the driving voltage V was applied to the two electrodes on the right-hand side (so as to simulate steps B or D of the actuation cycle); 4) for each step of the voltage ramp, the readings of the normal force were recorded after 10 s from the voltage application. Fig. 7 shows the experimental data as dots on a V-N graph. From Figure 4.7 it turns out that the curve can be treated with a good approximation as a power function:

$$N = f(V) = kV^{\beta}, \tag{4.2}$$

from which, through the knowledge of the coefficient of friction, we obtain the corresponding values of the tangent blocking force F_f as:

$$F_f = \mu N = \mu k V^{\beta}. \tag{4.3}$$

Performing a best fitting of the experimental data with the power function (4.2), the values k=7.646 10^{-10} $NV^{-\beta}$ with β=2.354 were obtained, for N expressed in N and V in V [SI]. Figure 4.7 shows the experimental data and the corresponding best fitting curve of both the normal blocking force N and the tangent blocking force F_f calculated for μ=0.63. The graph shows that the maximum tangential thrust that a multi-DoF HC-DEA can exert on a plastic object is around 0.1 N with a voltage of 3.5kV.

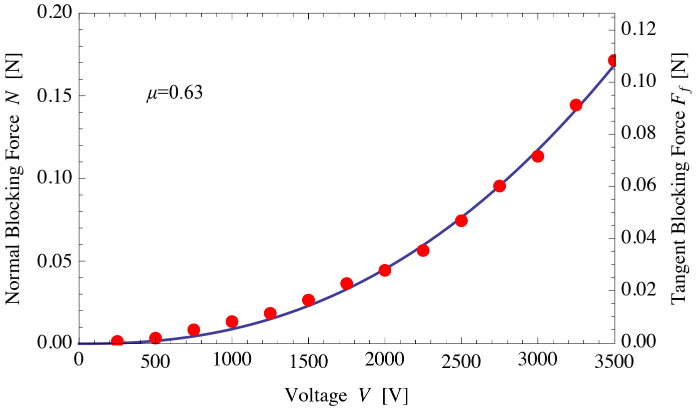

FIGURE 4.7: Plot of the normal blocking force N as a function of the driving voltage V, experimental data and best fitting function $N = f(V)$= 7.646 10^{-10} $V^{2.354}$. The correspondent tangential blocking force $F_f = \mu f(V)$ is also reported for a static friction coefficient μ=0.63 obtained for the contact with ABS plastic.

4.3.3 Compliance of the active membrane

When the active membrane of the actuator reaches the contact with an object the contact area increases with a non-linear function of the normal force N, and therefore of the driving voltage V. Since these relations provide information about the compliance of the actuator (e.g. allowing to calculate the contact pressure exerted at the interface), the contact area A was measured as a function of the driving voltage V by adding a further step to the test procedure reported in §4.3.2. Indeed, in this case the active membrane was smeared with a liquid colorant and a piece of graph paper was placed between the load cell plate and the actuator, allowing for measuring also the contact area imprints. For each step of voltage, the contact imprints were approximated by a best fitting circle calculated from a digital image analysis performed with MATLAB, with a 0.5 mm standard error on the estimate of the circle radius. The experimental data are plotted as dots in Figure 4.8. In order to compare the compliance of the HC-DEA with respect to other soft parts that are used as reference in soft robotics, it is worth approximating the nonlinear relation between the contact circle radius a and the voltage V with the best fitting power function:

$$a = h(V) = k'V^{\alpha}, \tag{4.4}$$

where k'=0.315 mmV$^{-\alpha}$, α=0.352 mm and V is expressed in V [SI]. In Figure 4.8 the best fitting power function is drawn with a continuous line.

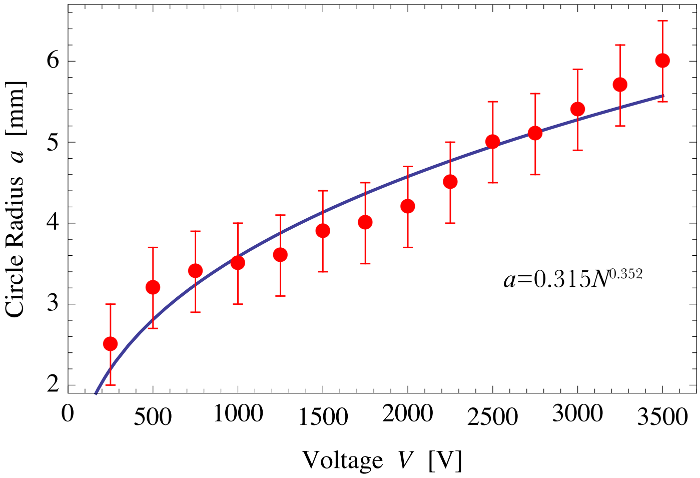

FIGURE 4.8: The contact circle radius a as a function of the driving voltage V, experimental data and best fitting function $a = h(V) = 0.315V^{0.352}$.

Considering both the nonlinear relations $f(V)$ described in (4.2) and $h(V)$ reported in (4.4), it is possible to calculate the expression $a = g(N) = h(f^{-1}(N))$ to obtain the nonlinear relation of the circle radius a as a function of the normal force N:

$$a = g(N) = k' \left(\frac{N}{k}\right)^{\alpha/\beta} = cN^{\gamma}, \tag{4.5}$$

where $c = \frac{k'}{k^{\gamma}}$ and $\gamma = \alpha/\beta$.

By using the coefficients α, β, k and k' previously defined we calculated $c = 7.270$ mmN$^{-\gamma}$ with γ=0.149, for a expressed in mm and N in N [SI], and consequently we obtained the nonlinear function $g(N)$ that relates the radius of the contact circle to the normal force N.

Indeed, this non-linearity between the normal force and contact area is common in contact mechanics, particularly in the case of soft silicone fingers performing grasping actions on rigid objects [76]. In order to assess the compliance of the multi-DoF HC-DEA to these soft silicone fingers a comparison is shown in Figure 4.9. In particular Figure 4.9 shows that the experimental data and the nonlinear power function $a = g(N)$ calculated for the multi-DoF HC-DEA are comprised between the two curves reported in [76], obtained for a soft silicone finger and a highly viscoelastic finger made of an artificial skin filled with gel. Figure 4.9 also shows that in the contact between the multi-DoF HC-DEA and a flat object, for small values of the normal force N the rate of increase of the contact area slows down as the normal force increases, whereas for higher values the rate of increase tend to be constant. This behavior is also observed in soft materials, such as rubber and silicone, as well as in human fingers [76, 77]. Thus, the multi-DoF HC-DEA makes a large area of contact for small normal forces, ensuring a gentle touch, which makes it suitable for handling delicate objects.

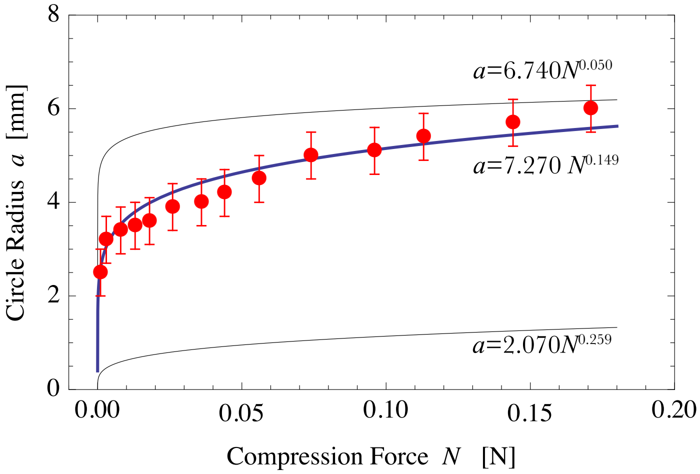

FIGURE 4.9: Compression force N vs contact circle radius a, experimental data and nonlinear function $a = g(N)$. The curve a= 7.270 $N^{0.149}$ obtained for the multi-DoF HC-DEA is in the range set by the curves a= 2.070 $N^{0.259}$ relating to a silicone finger and a=6.740 $N^{0.050}$ relating to a viscoelastic finger.

4.4 Flat object roto-translation experiments

In this section we describe the experiments performed to prove the capability of a single multi-DoF HC-DEA to translate a flat object. We also performed an actuation test with an array of two multi-DoF HC-DEAs, thereby roto-translating the flat object. The results from the experiments were merely for validating the actuation concept proposed in the previous sections.

4.4.1 Driving Electronics

To drive the multi-DoF HC-DEAs during the experiments, a custom-made electronics consisting of 4 modules powered by a 9 V battery was developed. Every module consisted of one channels; each channel was composed by a single high voltage power MOSFET (IXTF02N450, Ixys USA), a MOSFET driver (TC1427CPA, Microchip Technology, USA) and a 50 MΩ resistor (Figure 4.10).

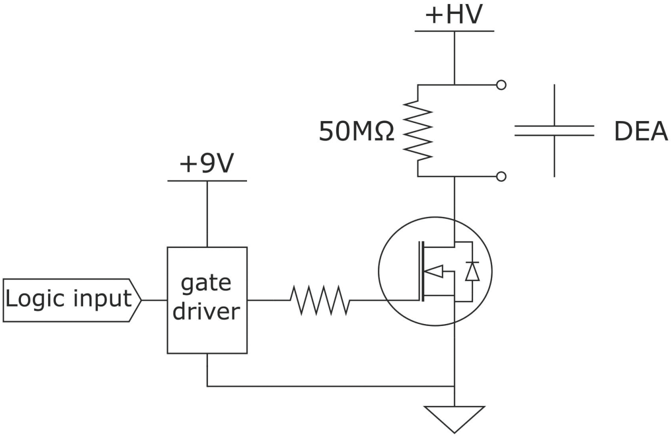

FIGURE 4.10: The modular electronic circuit employed for the activation of each multi-DoF HC-DEA.

The MOSFET, in a low side configuration (i.e.: when the load is between the power source and the MOSFET) worked as a switch, allowing for the maximum actuation voltage of 4.5 kV to be provided to the one actuator. A transistor-transistor-logic (TTL) signal (generated according to the actuation pattern) controlled the MOSFET driver, which worked as an interface allowing for a rapid and complete switching of the MOSFET gate. The 50 MΩ resistor was placed in parallel to each actuator to provide a discharge path, enabling the actuator to quickly return to its resting position when switched off. A four series-connected 8 bit serial-in parallel-out shift register was added to the system so as to enable the device to be controlled using a single serial interface instead of 28 GPIO pins. The signals, used to control the actuation cycles described in §4.2.3, were generated using an Arduino Due.

4.4.2 Translation test

In order to verify the ability of a single multi-DoF actuator to translate a flat object, a translation test was performed. A Petri dish with a weight of 8 g and a diameter of 90 mm was placed on the actuator's support and used as the object to be displaced during the experiment. The motion of the Petri dish placed on the support structure was triggered by the actuation cycle described in §4.2.3, which was set to last 4 seconds (1 second per step). Following the application of the 3.5 kV driving voltage, the actuator induced a horizontal translation of the Petri Dish of about 3 mm for each actuation cycle.

4.4.3 Roto-translation test

While in the previous experiment the translation of the Petri dish was obtained with just one actuator by applying the frictional force to the object, in order to achieve the roto-translation motion a torque was also required. As shown in Figure 4.11, two multi-DoF HC-DEAs were thus enclosed in a common support structure and secured through adjustment screws at a mutual distance of 70 mm. The support structure consisted of a 3D printed ABS plastic plane with a distribution of holes with a 20 mm diameter on which the Petri dish (the same Petri dish used for the translation experiment) was placed during the test.

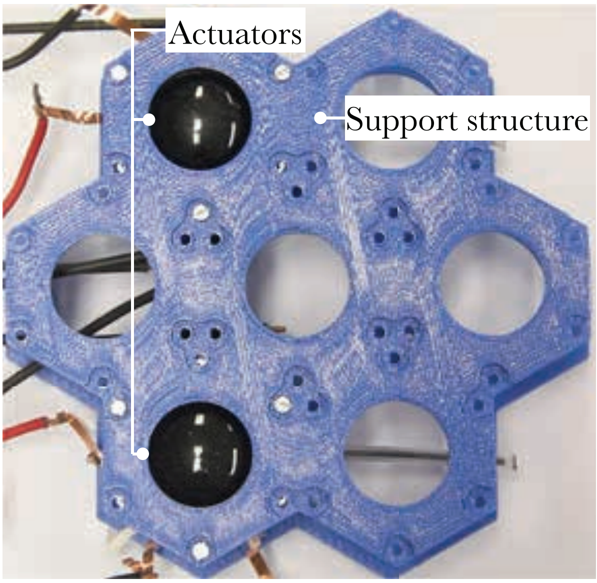

FIGURE 4.11: Setup used for the roto-translation test. Two multi-DoF HC-DEAs enclosed in the support structure used for the experiment.

In order to induce the roto-translation of the Petri dish placed on the surface of the support structure, the two actuators of the array represented in Figure 4.11 were activated with a combination of multiple translation and rotation phases as described in the following. In particular, during each translation phase, both actuators operated clockwise, by repeating the actuation cycle described in Figure 4.4, resulting in a translation of the Petri Dish of about 3 mm along the x-axis. On the other hand, during each rotation phase while one actuator operated following the actuation cycle clockwise, the other actuator reversed its motion operating in the anticlockwise direction. Since the lever distance between the two actuators was 70 mm, this resulted in the generation of a torque on the Petri dish, due to which a rotation of about 2.25° per cycle was achieved. Figure 12 shows a still frame sequence of the roto-translation test and graphical representation of the actuation control sequence. The test consisted of 5 steps of actuation each lasting 16 seconds, namely (b), (c), (d), (e) and (f) as shown in Figure 4.12. During each step both actuators performed Rotation phases (R), or Translation phases (T) according to the sequence reported in Figure 4.12. For each phase we also reported whether the actuator was Activated Clockwise (AC) or Activated Anticlockwise (AA).

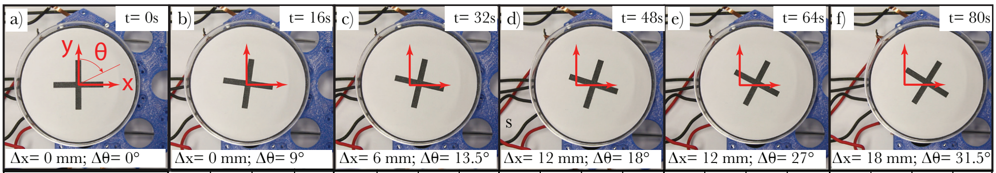

Actuation phases	R	R	R	R	T	T	R	R	R	R	T	T	R	R	R	R	T	T	R	R
Actuator 1	AC	AC	AC	AC	AC	AC	AC	AC	AC	AC	AC	AC	AC	AC	AC	AC	AC	AC	AC	AC
Actuator 2	AA	AA	AA	AA	AC	AC	AA	AA	AA	AA	AC	AC	AA	AA	AA	AA	AC	AC	AA	AA

0 16 32 48 64 s

FIGURE 4.12: Roto-translation sequence of a Petri Dish on an array of two multi-DoF HC-DEAs. Starting from the rest position (a), in each of the 5 steps of actuation (b), (c), (d), (e) and (f) both actuators performed rotation phases R, or translation phases T. When both actuators were Activated Clockwise (AC) a translation phase T was performed, resulting in a translation of the petri dish along the x-axis Δx=3mm. On the other hand, when the Actuator 1 was Activated Anticlockwise (AA), a rotation phase R was performed, resulting in a clockwise rotation of the petri dish $\Delta\theta = 2.25°$.

4.5 Conclusions

In this work we have presented an upgraded version of the Hydrostatically Coupled Dielectric Elastomer Actuator, which exploits the individual activation of four independent electrodes to achieve a tridimensional motion of its electroactive surface. This feature endows the actuator with a multi-degree of freedom kinematics that allows for the simultaneous generation of both a normal and a tangent action. Indeed, the simultaneous generation of both normal and tangential (frictional) forces distinguishes the proposed actuator from the state of the art, where only push-pull HC-DEAs are proposed. To demonstrate the capability of the multi-DoF HC-DEA for its use in the roto-translation of flat objects, an experimental characterization was carried out and phenomenological best fitting laws have been proposed. In particular, both the normal and the tangent blocking forces, which are functions of the driving voltage V, were derived from such laws. In addition, the relation between the contact area and the normal force acting at the interface with the object was obtained by fitting the experimental data with an analytical function describing an extension of the contact mechanics law of Hertz. This relation showed that the actuator features a gentle touch similar to the soft silicone fingers used in robotics, allowing for its use with delicate objects. Actuation tests were also conducted to assess the effectiveness of the multi-DoF HC-DEA in displacing and rotating a flat object. In fact, the soft platforms based on the push-pull HC-DEAs reported in literature can only displace round objects, specifically by triggering their rolling. On the other hand, we demonstrated that by using a minimum of two multi-DoF HC-DEA it is possible to also displace flat objects in a controllable manner. Therefore, the proposed actuator is suitable for designing modular soft platforms for roto-translating objects. It can also be adjusted in size and geometry in relation to the shape, dimensions and weight of the object to displace. Of particular interest for such systems is the dimensional scalability. While HC-DEAs with a diameter in the millimeter scale are reported to be effective [78], to the best of the authors' knowledge there are no reports in the literature regarding an HC-DEA with a diameter over few centimeters. Given that there is likely to be a limit value for the actuator's diameter beyond which the weight of the coupling fluid would hamper its actuation capability; further studies are being carried out.

Chapter 5

Stick and slip locomotion of a Soft Resonant Structure

In this chapter we present a smart robot structure that exploits anisotropic friction to achieve stick-slip locomotion. The robot is made out of three components: a plastic beam, a planar dielectric elastomer actuator and four bristle pads with asymmetric rigid metallic bristles. We show that when the robot is electronically activated at increasing frequency, its structure exploits the resonance condition to reach the maximum locomotion speed. The fundamental frequency of the structure is estimated both analytically and numerically, allowing the range of frequencies in which the top locomotion speed was observed during the experiments to be identified. The locomotion speed of the robot as a function of the actuation frequency is estimated with a frequency response analysis performed on a discretised model of the structure, revealing good agreement with the experimental evidence.

A manuscript of this work has been submitted for peer review:

- Calabrese, L., Berardo, A., De Rossi, D. E., Gei, M., Pugno, N. M., and Fantoni, G. (2019). A soft robot structure with limbless resonant, stick and slip locomotion. *Smart Materials and Structures*, (submitted).

5.1 Introduction

Nature has always been a source of inspiration for man to construct a large variety of artefacts. Hence, on the one hand, a large variety of artefacts have been made, all possessing, to some extent, life-like features. On the other, the world of modern technology is populated by machines made of strong, rigid, inorganic materials which exploit thermo-mechanical, electromagnetic and pneumatic/hydraulic energy conversion principles. In very recent years the field of robotics has seen a fast-growing interest and momentum in emerging knowledge of mechanism and materials exploited by natural organism to accomplish their living functions. Biologically inspired design [79], artificial ethology [80], artificial life [81], bio-robotics [82] and soft robotics [83] are different fields in which these tendencies manifest themselves. The propulsion and locomotion strategies proper of different animal species have been of interest to biologists for centuries and strongly revisited these days [84]. Boneless and limbless soft-bodied animals have recently attracted the interest of engineers trying to capture strategies and replicate functions that different species use for survival in different environments. Crawling, ciliary swimming, climbing digging and burrowing, regulation of particles-surface interactions and peristaltic transport are all functions under scrutiny by bio-inspired designers. In this paper, we describe a smart structure endowed with locomotion capabilities which combine resonant activation [85] and anisotropic friction [86]. While operation at resonance provides a minimum in energy consumption and speed changes, still maintaining this energy minimum, by simply tuning body resonance, functional anisotropy offers valid design options for direction-dependent or orientation-dependent sliding [87]. The structure is actuated by a dielectric elastomer actuator which, in addition to fast, silent large stroke and durability [13], also has the capacity of self–sensing [88] which easily enables closed-loop control [89].

5.2 Materials and Methods

5.2.1 Concept design

The robot presented in this work consists of an assembly of three components: a plastic beam, a planar Dielectric Elastomer (DE) actuator and four bristle pads with asymmetric rigid bristles, see Figure 5.1a. Since the actuator behaves as a spring with initial pretension (as better explained in the following), when coupled to the bent plastic beam it results in a self-standing structure in which elastic energy is stored. From this configuration (Figure 5.1b, top), owing to the capability of the DE membrane to elongate upon application of a driving voltage V [26], a part of the stored elastic energy is released, allowing the robot to deform by increasing its length (Fig. 1b, centre): the back bristles stick to the ground and the front bristles slip forward. In a second phase, when the voltage V is switched off, the DE actuator shortens, returning to its original length. This triggers the forward slip of the back bristles while the front bristles are stuck to the ground resulting in an overall net displacement δx (Figure 5.1b, bottom). What is here described as a simple sequence of two steps can be enhanced by exploiting the vibration properties of the structure and impose an on-off frequency of the voltage signal close to the resonance frequency of the robot.

5.2.2 Robot components

Dielectric elastomer actuator

As previously reported, DE actuators are electromechanical transducers consisting of a thin layer of a dielectric elastomer coated on both sides with compliant electrodes. When a voltage V is applied across the electrodes, the attraction electrostatic forces squeezes the soft dielectric layer causing a reduction of its thickness and an expansion of its surface [26]. Since in our case only a unidirectional actuation along the longitudinal direction is needed, we equipped the DE actuator with stiffening elements aligned in the transverse direction, as previously reported to be effective for this purpose [51, 90]. The DE actuator was manufactured by coupling two layers of an acrylic

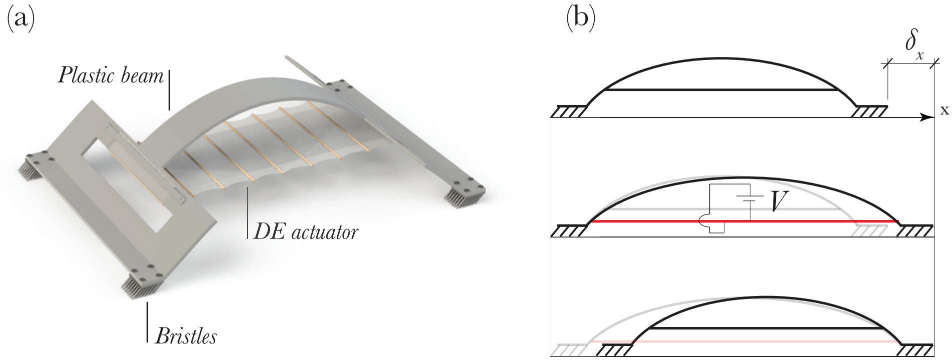

FIGURE 5.1: Schematic drawing of the locomotion robot (a) consisting of an assembly of three components: a plastic beam, a dielectric elastomer actuator and four clawed pads featuring rigid bristles with an asymmetric orientation. The locomotion cycle (b) starts from the initial self-standing configuration (top); when a voltage V is applied to the DE actuator, an elongation is induced resulting in a forward slip of the front bristles (centre); finally, when the voltage is switched off the DE actuator shrinks, resulting in a forward slip of the back bristles (bottom).

elastomer film (VHB 4910, 3M, USA), each of them featuring a thickness at rest of 1 mm, a width of 12.5 mm and a length of 17.5 mm, chosen because of its well-known high electromechanical transduction performance in terms of achievable active stress and actuation speed. To manufacture the actuator, the two VHB 4910 membranes were equi-biaxially pre-stretched by 300% and attached to individual support frames allowing for obtaining an actuator with a length of 70 mm and a width of 50 mm. At this stage, such pre-strain caused a thickness reduction of the coupled layers from 2 mm to 0.125 mm in the regions between the stiffening elements. The use of that pre-strain is justified by its well-known beneficial effect in terms of increase of electromechanical actuation [91]. The stiffening elements, consisting of wood sticks of 1.5 mm in diameter and 50 mm in length, were aligned with a uniform pitch of 10 mm. The well-known adhesive properties of the VHB material simplified the manufacturing process by ensuring a proper bonding between the layers, also allowing for properly retaining the stiffening elements enclosed between them as schematically represented in Figure 5.2. The DE actuator was eventually removed from the support frames and coupled with the plastic beam as better explained in the following. The compliant electrodes consisted of carbon conductive grease (MG Chemicals, Canada). The mass of the actuator, measured with a precision scale, accounted for 2.5 g. A schematic of the DE actuator is represented in Figure 5.2.

In order to measure the axial stiffness of the DE actuator about the pre-stretched configuration, a tensile test with a uniaxial tensile machine was performed. The DEA was secured to the load cell clamps with an initial length correspondent to the original strain of 300% along the longitudinal direction. The tensile test was performed with a speed of 3 mm/s (corresponding to a strain rate of 0.043 s^{-1}). The test results are reported in Figure 5.3, in which the increment in force required to elongate the specimen is reported.

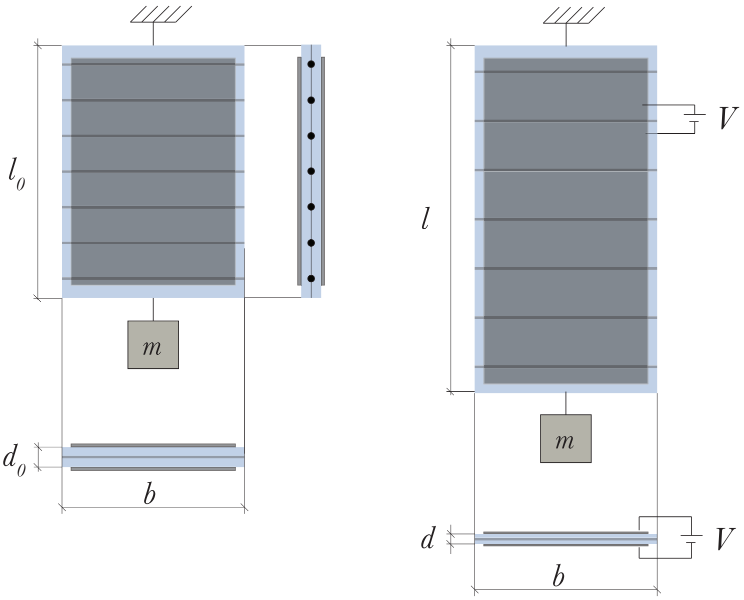

FIGURE 5.2: Schematic drawing of the DE actuator with embedded stiffening elements aligned along the transversal direction. When a load pre-stretches the actuator, the initial length l_0 is obtained (left). Upon application of a driving voltage V and since the elongation along the other in-plane direction is prevented by the stiffening elements, the actuator elongates along the longitudinal direction only reaching the length $l < l_0$.

By noting that the linear fit indicated with a red line interpolates satisfactorily the experimental data, we computed its slope that corresponds to the stiffness of the specimen, namely k_{DEA}=29.85 N/m. The reproduction of the same test with a hyper-electro-elastic model has proven to be difficult due to the lack of reliable and extensive investigations of the behaviour of the acrylic elastomer under investigation at large in-plane pre-stretches. The work by Hossain et al. [91] aimed at filling this gap, however the studied transverse pre-stretch was only up to 200%.

Plastic beam

The plastic beam of the robot was obtained from a 1.5 mm thick flat sheet of solid polystyrene plastic having a volumetric mass density of 1050 kg/m^3, the shape schematically represented in Figure 5.4 was realized with a CNC milling machine. The beam features a central part having a width of 20 mm and a length of 100 mm and two side appendices where, by exploiting the presence of interlocking holes (having a 2.5 mm diameter and 7 mm pitch), the clawed pads are secured. A rectangular opening on each appendix allowed for coupling the DE actuator to the plastic structure. The DE actuator was secured to the structure by means of one rigid plastic bar per side screwed to the structure as previously shown in Figure 5.1. Each rigid plastic bar and its screws accounted for a weight of 1.25 g.

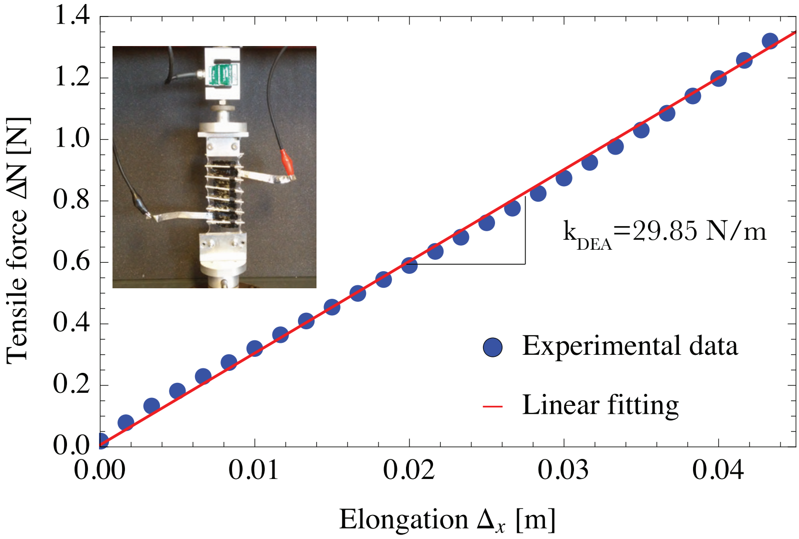

FIGURE 5.3: Tensile test of the DE actuator to calculate the tensile stiffness k_{DEA}=29.85 N/m. The test was performed with a strain rate of 0.043 s^{-1}.

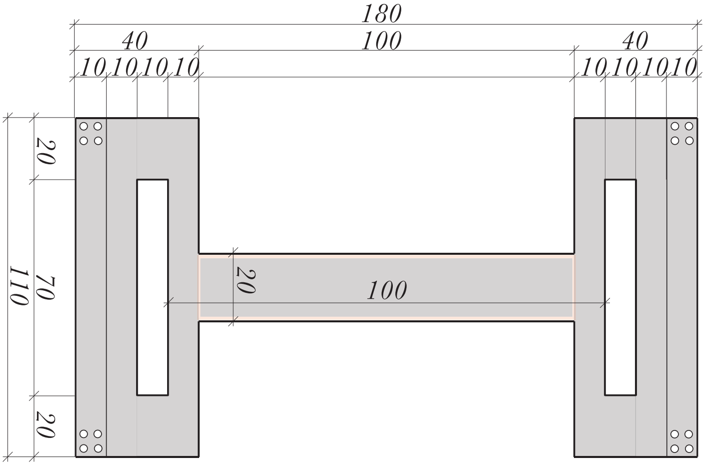

FIGURE 5.4: Schematic drawing of the structure of the robot: unbent plastic structure (a), self-standing operational configuration (b) and particular of the clawed pads featuring the asymmetric steel bristles (c). All dimensions are expressed in mm.

The polystyrene plastic was characterised by performing a tensile test with a uniaxial tensile machine on five "dogbone" specimens conforming to the type V shape reported in the ASTM D638-03. The test speed was 0.0167 mm/s. From the average values of the experimental data reported in Figure 5.5 we see that the stress-strain curve begins with a toe region. As stated in the Annex A1 to the ASTM D638-03, this region does not represent a property of the material since it is caused by a take up of slack and alignment or seating of the specimen. Therefore, to obtain a correct value of the elastic modulus, the stress-strain values must be compensated to give the corrected zero point on the strain or extension axis by following the reported procedure. According to such procedure, the modulus of elasticity is obtained by extending the initial linear portion of the load-extension curve and dividing the difference in stress corresponding to any segment of section on this straight line by the corresponding difference in strain using the average original area of the cross section in the gauge length segment of the specimen. Following this procedure for the strain interval 0.014 < ε <0.02, the Young's modulus Y = 1.172 GPa was calculated.

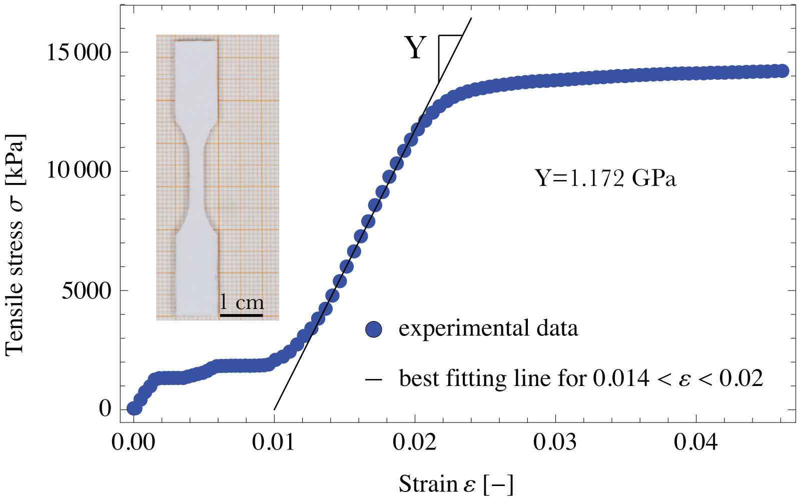

FIGURE 5.5: Tensile test of the styrene plastic material: experimental stress-strain data and estimation of the Young's modulus.

Bristle pads

Two different types of bristle pads were tested. The first one was obtained by 3D printing a photopolymer resin (Clear FLGPCL02, FormLabs, USA) with a stereolithography 3D printer (Form2, FormLabs, USA) eventually exposed to UV rays for 20 min in order to increase its hardness. The second one consisted of stainless-steel bristles obtained from a commercial bristle belt used in the textile industry for carding fibres. Figure 5.6 shows a picture of each pad. As shown in Figure 5.6a, the bristles of the 3D printed pads were manufactured with six different angles with respect to the vertical axis (from 15° to 65°). Despite the change of the angle, each pad featured a constant height of 6 mm, achieved by compensating the thickness of each base. Each pad presented a total of 49 bristles arranged in seven rows and seven lines aligned with a uniform pitch of 1.5 mm on a squared base plate having a 16 mm side dimension. Each bristle had a diameter of 0.7 mm ending with a sharp tip printed with convergent semi-angle of 13°. The stainless-steel pads were composed of six rows and seven lines of bristles, aligned with a uniform pitch of 1.5 mm, for a total of 42 steel bristles on each pad. Each bristle possesses a 5 mm straight part coming out from the rubber substrate and an oblique part ending with a sharp tip also measuring 5 mm in length. As shown in Figure 5.6b, the oblique part presented an angle of 55° with respect to the vertical axis for a total height of 11 mm.

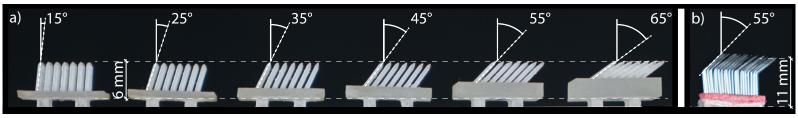

FIGURE 5.6: Bristle pads: resin 3D printed (a), stainless steel (b).

As better described in the following, during the locomotion tests of the robot both types of pads operated in contact with a horizontal surface covered with baking paper. For this reason, we measured the static friction coefficient against baking paper of each pad either in the case of forward or backward sliding with an ad hoc custom-built setup, shown in Figure 5.7. The setup consisted of three main components: a tensile testing machine, a linear guide and a slider (Figure 5.7). The linear guide was made out of rigid polycarbonate, whose top surface was coupled with a baking paper layer by means of double-sided adhesive tape, constituting the reference surface on which the samples were tested. The sample holder, coupled with the different samples of the bristle pads, constituted the slider, as shown in the close-up view of Figure 5.7. The sample holder, whose self-weight corresponded to 7 g, also allowed for loading the sample with a supplementary mass m = 20 g, needed to maintaining a proper contact with the surface of the linear guide during the sliding. A double inextensible wire, connected to the grip of the tensile machine, pulled the slider with a constant speed of 0.1 mm/s. For each sample, the pulling force, i.e. the friction force transmitted from the sliding surface to the load cell trough a frictionless roller, was continuously recorded during the sliding. The self-weight of each 3D printed bristle pad was measured with a precision scale, the following values were recorded: 0.46 g, 0.51 g, 0.60 g, 0.74 g, 0.93 g and 1.18 g for angles 15°, 25°, 35°, 45°, 55°, 65°, respectively. The self-weight of the steel bristle pad accounted for 0.5 g. The total weight of the slider was calculated by adding the masses of the bristle pad, the sample holder and the supplementary mass m, allowing for calculating the total normal force applied to the sample for each test performed.

At the time of incipient sliding, when the detachment force was reached, the static friction force corresponded to the first maximum peak in the load-displacement curve. After reaching this peak, the sample started sliding at an approximately constant force value, corresponding to the dynamic friction force. When this value had stabilized, the test was stopped. The dynamic friction force was taken as the mean value during the sliding phase. Since no adhesion occurred, both the static and dynamic friction coefficients μ_s and μ_d were calculated as the ratio between the friction force (static and dynamic, respectively) and the applied normal load. In Figure 5.8, we report the experimental results obtained from the friction tests for every pad configuration. From the results, it can be deduced that while the 3D printed pads at first sight seems to be characterized by a similar behaviour in either forward or backward sliding, stainless steel pads exhibit a substantial variation in the coefficient of friction with respect to the sliding direction.

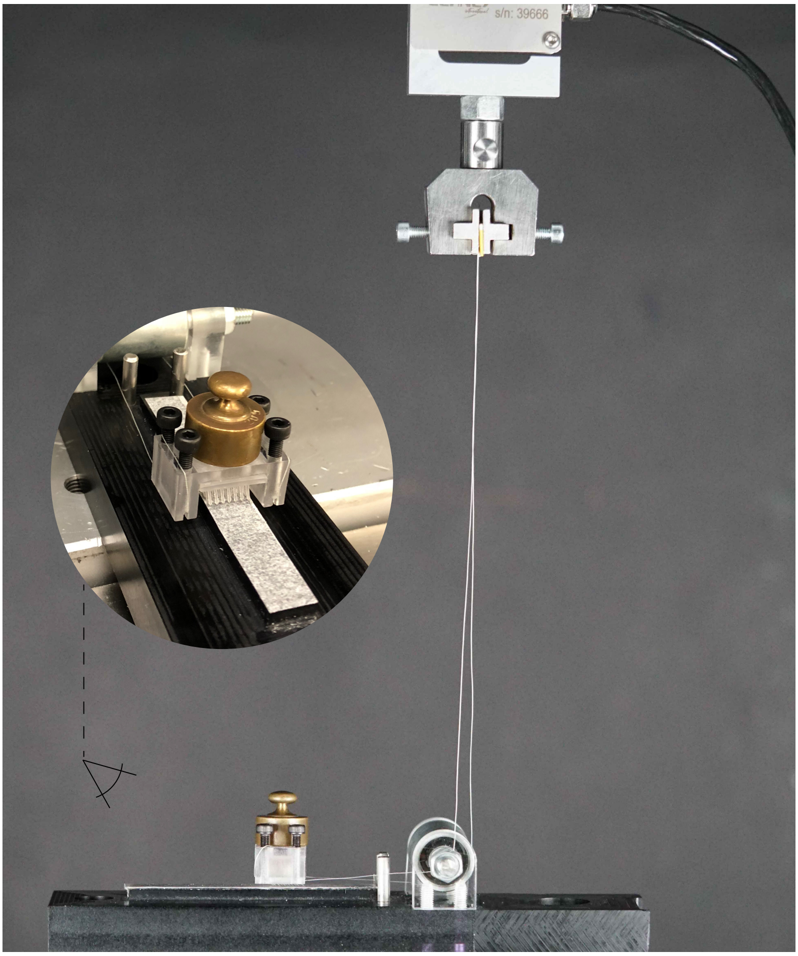

FIGURE 5.7: Experimental setup for the measurement of the friction force generated at the interface between the testing surface and the bristle pads. The bristle pad sample coupled to the sample holder and loaded with a mass m = 20 g constituting the slider. A double inextensible wire allowed for pulling the slider with a tensile machine along the linear guide covered with a layer of baking paper showed in the enlargement of the picture.

It is worth to point out that the friction coefficient for the 3D printed pads present variability related to the bristle's angle. Indeed, from Figure 5.9 we see that both μ_s and μ_d peaks at 35° in case of backward sliding, while it seems that the optimum value for those coefficients in case of forward sliding lies within the range 35°-45°. The relatively high value of the friction coefficient for the pad whose angle is 15° can be explained considering that the bristles may have engaged with the baking paper surface during the sliding test. For such a low value of the angle the entire load was applied directly to the bristle tip, possibly inducing a slight indentation.

As shown in Figure 5.8 and highlighted in Figure 5.10, for the 3D printed pads with a grade up to 35° the friction coefficient measured during the backward sliding

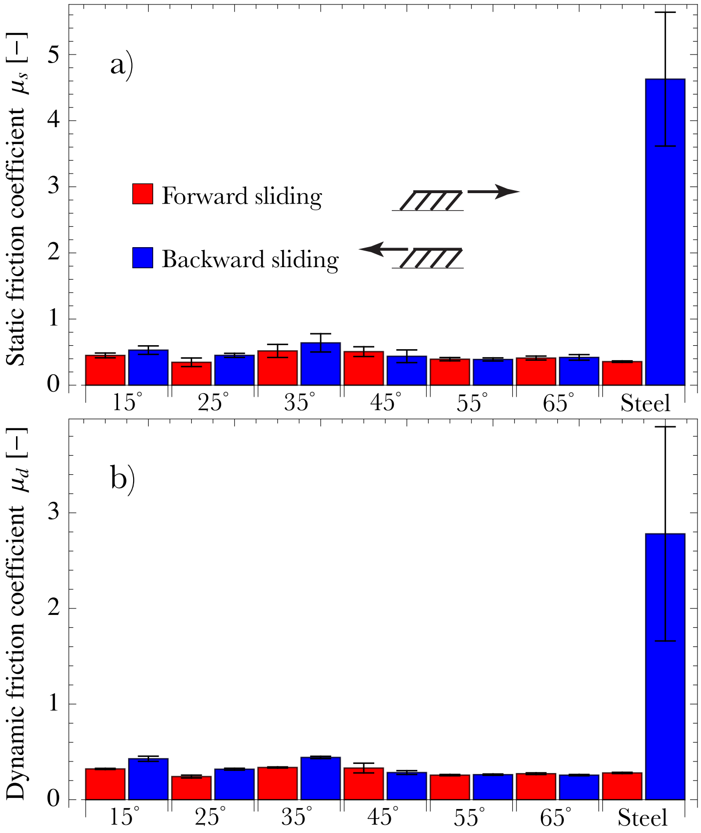

FIGURE 5.8: Static (a) and dynamic (b) friction coefficients of the six 3D printed bristle pads (indicated with the values of the angles) and the steel bristle pad.

was greater than that observed during the forward sliding. Conversely, when the value of the angle increased beyond 35°, an opposite trend was revealed. This trend may lead to the possibility of a motion inversion of the robot simply triggered by a variation of its actuation frequency. This behaviour has been already revealed in a bristle-bot featured by flexible joints between the bristles and the substrate [92, 93]. The one we present here possesses rigid bristles. We do believe this is the reason why we were not able to observe such motion inversion during the locomotion tests we performed. Nonetheless, we also believe that a motion inversion is possible by optimizing the bristle's design.

5.2.3 Robot manufacturing

Upon coupling with the plastic beam, the DE actuator was subject to a tensile load along the longitudinal direction. Due to the highly viscoelastic behaviour of the VHB acrylic elastomer, its length increased from 70 mm to 110 mm after 24 hours, resulting in an increase of its longitudinal pre-stretch from the initial 300% up to 529%. This caused a further average thickness reduction of the DE membrane from 0.125 mm

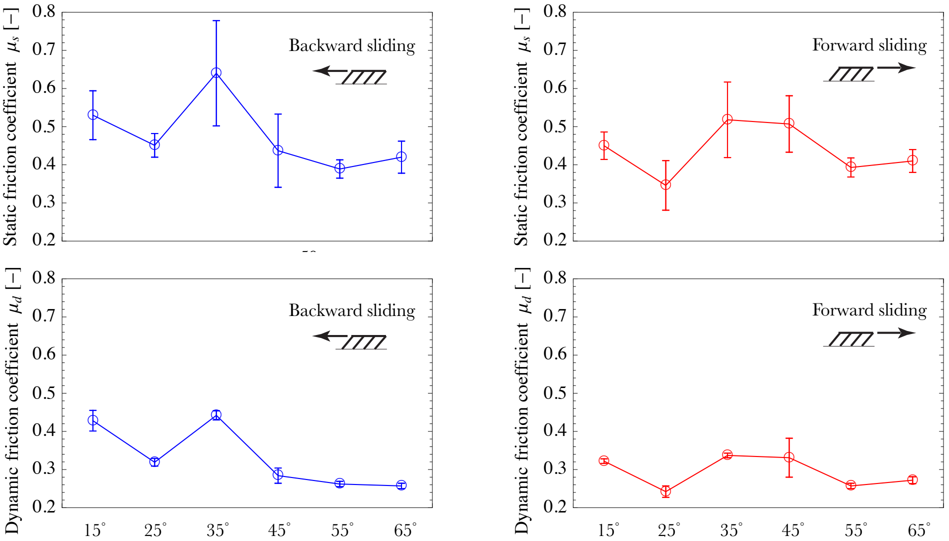

FIGURE 5.9: Static and dynamic friction coefficients of the 3D printed bristle pads for increasing value of the bristle's angle.

to 0.080 mm, calculated assuming material incompressibility. As better described in the following, during the locomotion tests the robot was eventually loaded on its top with a lumped mass m = 9 g made out of two metallic bolts coupled together by means of a double-sided adhesive tape of negligible weight.

5.2.4 Estimation of the fundamental frequency

The analysis of the locomotion of the robot requires the estimate of the fundamental frequency f_n of the system that is computed in this section following two approaches: the one that is first presented is based on the Rayleigh's quotient method, the second one relies on a finite element computation.

Analytical: Rayleigh's quotient method

The fundamental frequency of the robot is estimated through the Rayleigh's quotient [94] on the structure schematically represented in Figure 5.11. In this calculation, the asymmetry induced by the bristles is neglected and therefore the structure is considered symmetric and only its left-hand half is studied, being composed of six subsystems, namely the beam segment EF, the parts AB, BD and DE, the spring DO and the lumped mass m/2. Slider constraints are imposed along the symmetry axis y in F and O. The horizontal length $l/2 = 55$ mm and the height $h = 25$ mm correspond to the half-length of the dielectric elastomer actuator and to the rise of the beam in the operational configuration, respectively. The curved beam DFD′ can be satisfactorily

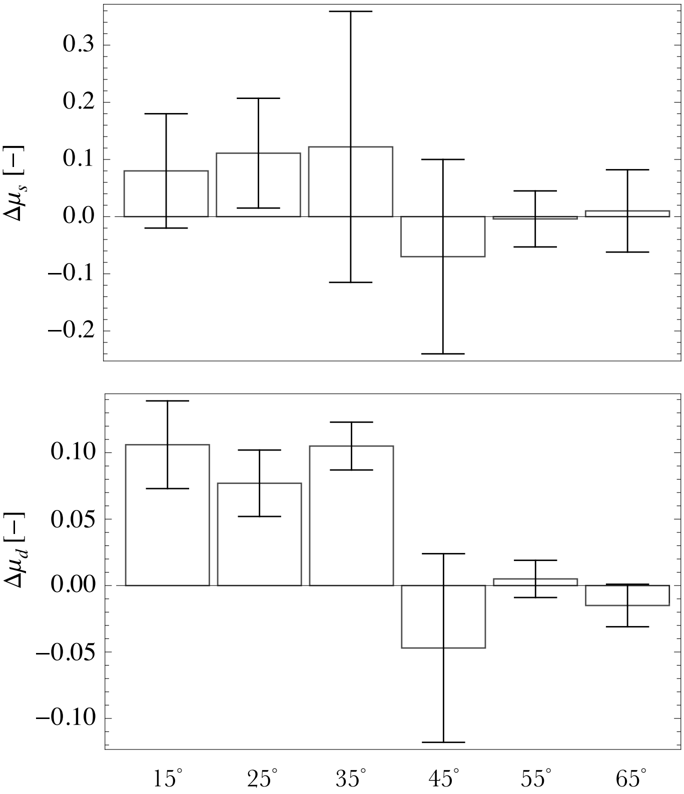

FIGURE 5.10: Variation of the backward vs forward sliding static and dynamic friction coefficients of the 3D printed bristle pads for increasing value of the bristle's angle. The error bar associated with each value of $\Delta\mu_s$ and $\Delta\mu_s$ is calculated according to the variance sum law.

described by the sinusoidal function

$$y(x) = h\left[\sin\left(x + \frac{l}{2}\right)\frac{\pi}{l}\right] \tag{5.1}$$

and its slope in D, namely $y'(-l/2)$, provides the angle $\bar{\theta}$.

When the square wave voltage signal is applied to the elastomer actuator, the structure of the robot vibrates about its initial configuration with the fundamental mode sketched in Figure 5.12. We assume that during this motion, the parts AB and BD undergo a rigid rotation about point D as represented in the detail of Figure 5.12. By considering the static scheme of the beam shown in Figure 5.11 and Figure 5.12, with an application of the principle of the virtual work it is possible to calculate that an arbitrary horizontal infinitesimal displacement δ_x in D generates a vertical displacement in F whose value is 1.772 δ_x. With reference to Figure 5.11, we introduce the curvilinear abscissa s on the beam segment DF, and the coordinates η and ξ on

AB and BD, respectively. The displacements of actuator DO is described by the coordinate x.

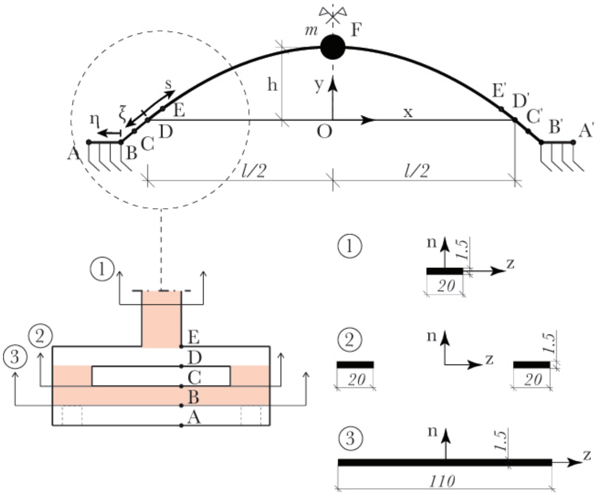
m
F
h
y
s
ξ
η
E
D
C
B
A
O
x
E'
D'
C'
B'
A'
l/2
l/2
①
②
③
E
D
C
B
A
n
z
1.5
20
20
20
110

FIGURE 5.11: Schematic representation of the robot structure. Top: longitudinal section. Bottom: top view of the detail of the connection between curved beam, straight actuator and clawed pads (whose perimeters are sketched with dashed lines) (left) and detail of the cross sections (right). Coordinate z describes the out-of-plane axis. Dimensions are expressed in mm.

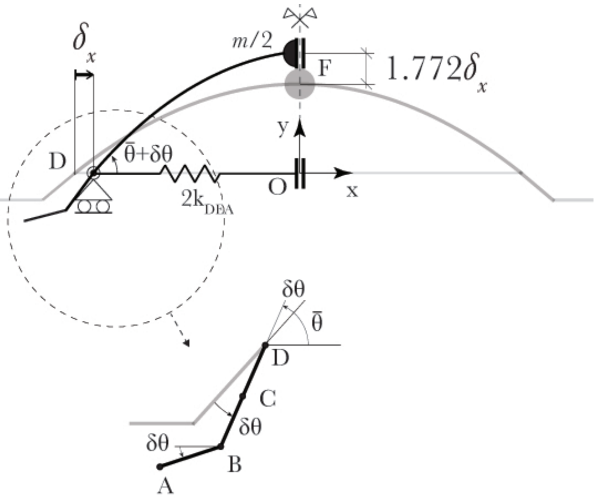
δ_x
m/2
F
$1.772\delta_x$
y
D
$\bar{\theta}+\delta\theta$
$2k_{DBA}$
O
x
δθ
$\bar{\theta}$
D
C
δθ
δθ
B
A

FIGURE 5.12: Schematic representation of the robot about the initial configuration of equilibrium. An imposed horizontal displacement δ_x in D induces a vertical displacement $1.772\delta_x$ in F. The magnification shows the kinematics of the rigid motion of the structure about point D.

When the system is vibrating in its fundamental eigenmode, by assuming a separable solution for the generic displacement w of its points, for each component of the system we can formally write

$$\boldsymbol{w}(\psi,t) = \boldsymbol{W}(\psi)\sin(\omega_n t) = (w_x(\psi)\boldsymbol{i} + w_y(\psi)\boldsymbol{j})\sin(\omega_n t), \tag{5.2}$$

where $\boldsymbol{W}(\psi)$ is an eigenfunction that approximately represents the shape of the system and ω_n is the vibration circular frequency. In (5.2), ψ represents the generic abscissa describing each element of the structure. In particular, $\psi \equiv s$ for the segments DE and EF, $\psi \equiv \eta$ for AB, $\psi \equiv \xi$ for the segment BD and $\psi \equiv x$ for the spring DO. The vertical displacement of mass $m/2$ corresponds to the same quantity of the beam segment EF at point F.

The Rayleigh's quotient allows the evaluation of the frequency $f_n = \omega_n/(2\pi)$ by equalling maximum strain ($U^{\max}$) and maximum kinetic ($K^{\max}$) energies computed for the system by assuming the vibration mode described by eq. (5.2), namely

$$\sum_{i=1}^{6} U_i^{max} = \sum_{i=1}^{6} K_i^{max} \tag{5.3}$$

where the two energies are written as a sum of contributions of the six subsystems, each described by index i running from 1 to 6, as detailed in the following. Note, however, that for some elements the maximum strain energy is vanishing. It should be emphasised that due to the form (5.2) of the eigenmode, in the interval $t \in [0, 2\pi/\omega n[$ the maximum strain energy for each element is reached at $t = \pi/(2\omega n)$, while the maximum kinetic energy is to be sought at $t = 0$.

Beam EF ($i = \mathbf{1}$). For the beam segment EF, we assume that its shape during the vibration is described by the shape function $W(s) = w_x(s)\boldsymbol{i} + w_y(s)\boldsymbol{j}$ whose components are

$$w_x(s) = \delta_x \cos(\pi \frac{s}{L}), \tag{5.4a}$$

$$w_y(s) = 1.772\delta_x \sin(\pi \frac{s}{L}), \tag{5.4b}$$

where L = 120 mm. In eq. (5.4), $\boldsymbol{i}$ and $\boldsymbol{j}$ are the component of an orthonormal basis associated with axis x and y, respectively. The kinetic energy is therefore given by

$$K_1 = \frac{1}{2}\int_{L/12}^{L/2} \mu_1 \dot{\boldsymbol{w}}(s,t)^2 ds, \tag{5.5}$$

where the mass per unit length μ_1= 0.0315 kg/m is calculated over a length of 0.05 m (that corresponds to the half-length of the central beam as shown in Figure 5.11 and a superposed dot indicates differentiation with respect to time. The transverse component of the total displacement, which is the one contributing to the elastic strain energy when the axial elongation of the beam is neglected, is given by

$$\boldsymbol{w}_{tr}(s,t) = \boldsymbol{w}(s,t)\cos\gamma(s), \tag{5.6}$$

where $\gamma = \frac{\pi}{2} - \alpha + \beta$, with $\alpha = \tan^{-1}(y'(x))$ and $\beta = \tan^{-1}(w_x(s)/w_y(s))$.

The strain energy stored during the deformation is

$$U_1 = \frac{1}{2} Y I_{zz} \int_{L/12}^{L/2} (\boldsymbol{w_{tr}}(s,t)'')^2 ds, \tag{5.7}$$

where I_{zz} is the second moment of area of the beam cross section (see Figure 5.11) and a dash denote differentiation with respect to the coordinate s.

Beam DE ($i = \mathbf{2}$). The shape of the beam segment DE is also described by the shape function $W(s)$ defined through the components (5.4). Assuming that the section vibrates as a rigid body, the strain energy is $U_2 = 0$, whereas the kinetic energy can be written as

$$K_2 = \frac{1}{2} \int_0^{L/2} \mu_2 \dot{\boldsymbol{w}}(s,t)^2 ds, \tag{5.8}$$

where the mass per unit length μ_2= 0.2983 kg/m is calculated taking into account the weights of both the plastic structure between points D and E (Figure 5.11) and the rigid plastic bar screwed on it.

Segment AB ($i = \mathbf{3}$). This is a rigid body, therefore $U_3 = 0$. Considering a uniform mass distributed along AB whose density (per unit length) is μ_3= 0.273 kg/m (μ_3 is comprehensive of the two bristle pads each weighing 0.5 g), the kinetic energy of AB is given by

$$K_3 = \frac{1}{2} \int_0^{\bar{\eta}} \mu_3 \dot{\boldsymbol{w}}(\eta,t)^2 d\eta, \tag{5.9}$$

where the components of the displacement along x and y are

$$w_x(\eta) = \delta_x + \bar{\xi}\delta\theta \sin\bar{\theta}, \tag{5.10a}$$

$$w_y(\eta) = -\bar{\xi}\delta\theta \cos\bar{\theta} - \eta\delta\theta, \tag{5.10b}$$

respectively.

Segment BD ($i = \mathbf{4}$). BD is considered as a rigid body as well, then $U_4 = 0$. Considering a uniform mass distribution μ_4= 0.1181 kg/m, the kinetic energy of BD can be written as

$$K_4 = \frac{1}{2} \int_0^{\bar{\xi}} \mu_4 \dot{\boldsymbol{w}}(\xi,t)^2 d\xi, \tag{5.11}$$

where the components of the displacement along x and y are now given by

$$w_x(\xi) = \delta_x + \bar{\xi}\delta\theta \sin\bar{\theta}, \tag{5.12a}$$

$$w_y(\eta) = -\bar{\xi}\delta\theta \cos\bar{\theta}. \tag{5.12b}$$

Dielectric elastomer actuator ($i = \mathbf{5}$). The DE actuator is modelled as a spring of length $l/2$, therefore the stiffness is twice that computed in § 5.2.2, namely $2k_{DEA}$= 59.70 N/m. Moreover, μ_5= 0.0227 kg/m and the two components of the displacement function are

$$w_x(x) = -\delta_x \left(\frac{2x}{l}\right), \tag{5.13a}$$

$$w_y(\eta) = 0. \tag{5.13b}$$

Therefore the kinetic energy is

$$K_5 = \frac{1}{2}\int_{-l/2}^{0} \mu_5 \dot{w}(x,t)^2 dx, \tag{5.14}$$

while the maximum value of the strain energy can be easily written as

$$U_5 = \frac{1}{2}(2k_{DEA})\delta_x^2. \tag{5.15}$$

Point mass $(i = \mathbf{6})$. The mass possesses only kinetic energy (i.e. U_6=0) that can be written as

$$K_6 = \frac{m}{4}\left(\dot{w}_y(s)|_{L/2}\right)^2. \tag{5.16}$$

Eq. (5.3) can be solved for ω_n to obtain the estimation of the fundamental frequency f_n. The values f_n=24.29 Hz and f_n=19.77 Hz were calculated for m=0 and m=9 g, respectively.

Numerical: finite element analysis

The Finite Element Method (FEM) was used to numerically estimate the eigenfrequencies and the modal shapes of a 3D model of the robot. The model was developed with the Solid Mechanics module of the COMSOL Multiphysics v. 5.0 software. In this model, the polystyrene plastic beam was considered as a linear elastic material. While the Young's modulus Y was obtained with the tensile test reported in § 5.2.2, the value of the Poisson's modulus ν = 0.32 was adopted from literature [95]. We exploit the symmetry of the structure by imposing a null displacement of the centreline in F along x and z, and a roller constraint along both the edges in D and D′ which corresponds to the static scheme reported in § 5.2.4. We assume that the shape of the central beam in the deformed configuration is given by (5.1) while all the other dimensions are as reported in Figure 5.4. The lumped mass m and the masses due to the bristle pads, to the rigid bar and its screws and the mass of the DE actuator are assigned as edge loads along the edges defined by the points F, A, E and D, respectively. The DE actuator is modelled as a linear spring by assigning a "Spring Foundation" constraint with $2k_{DEA}$= 59.70 N/m in correspondence of each roller. The structure was meshed with 9167, 6738, 1410 and 132 tetrahedral, triangular, edge and vertex quadratic elements respectively by using the COMSOL mesh subroutine. The meshed structure is shown in Figure 5.13. The eigenfrequencies and the correspondent modal shapes, for both the loaded with m=9 g and the unloaded case, were obtained by using the COMSOL's "Eigenfrequency Study" solver. The values f_n=22.79 Hz and f_n=18.12 Hz were calculated for m=0 and m=9 g, respectively.

5.2.5 Frequency response analysis: calculation of net displacement and locomotion speed

In this section, we report about the FEM model developed to calculate the overall net displacement of the robot δ_x during each actuation cycle as a function of the actuation frequency f. To do so we modified the numerical model presented in § 5.2.4 by taking

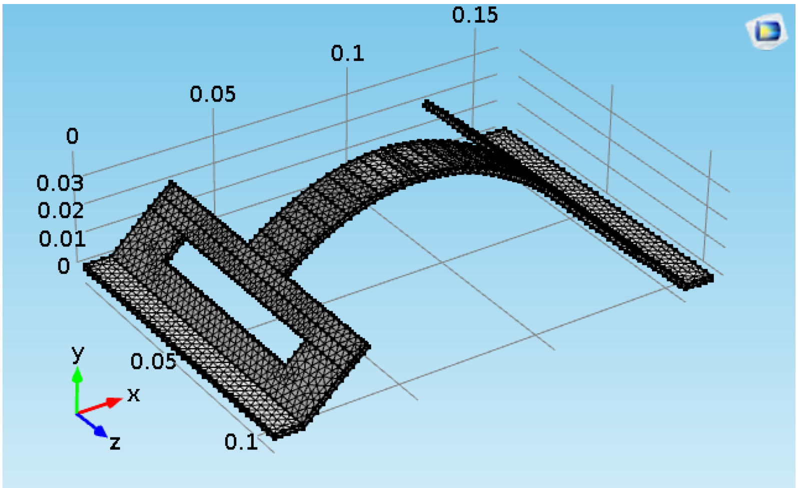

FIGURE 5.13: Mesh of the robot plastic structure about the initial configuration of equilibrium. The DE actuator is not visually represented since its presence is imposed as equivalent spring constraints to the plastic structure.

in account the viscoelastic response of the DE actuator, as better explained in the following of this section. This allowed the theoretical locomotion speed along the x-axis v_x, namely

$$v_x = f\delta_x, \tag{5.17}$$

to be estimated and compared with the experimental measurements.

The structure was loaded with a force F_x, applied as a step load in correspondence of the external edge identified on the plastic structure by the point D (see Figure 5.11) with frequency f to simulate the effect of the voltage driving. The force was set to F_x = 0.25 N since for this value the total displacement δ_x obtained from the model with a static analysis was equal to that measured in the lab, namely δ_x= 1 mm.

The frequency response of the robot highly depends on the mechanical damping of its deformable components: the polystyrene plastic beam and the VHB 4910 DE actuator. The damping of the polystyrene plastic beam was modelled with a rate-independent isotropic structural loss factor η= 0.04 [96], which is defined as the ratio of the energy dissipated per cycle to the maximum strain energy stored. The frequency response of the DE actuator requires a more accurate modelling due to its highly frequency-dependent viscoelastic behaviour [97]. For this reason, we modelled it as a Kelvin-Voigt material, which consists of a purely viscous damper and a purely elastic spring connected in parallel [98] as shown in Figure 5.14. For this model, the relaxation time constant τ is

$$\tau = \frac{C_d}{2k_x}, \tag{5.18}$$

where C_d is the coefficient of viscous damping and $2k_x$ is the stiffness of the VHB material.

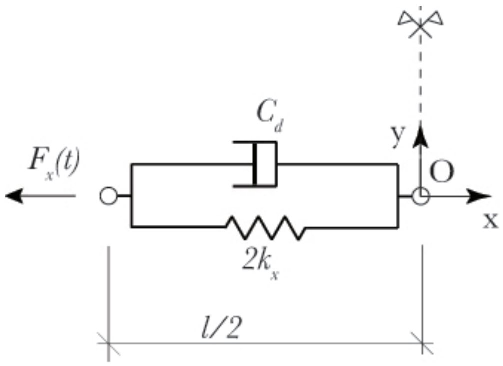

FIGURE 5.14: Kelvin-Voigt model adopted to describe the viscoelastic behaviour of the DE actuator.

Since the elastomer is loaded with a time-dependent load, it presents a rate-dependent viscoelastic behaviour that results in a reduction of the relaxation time constant τ for increasing values of the longitudinal stretch rate $d\lambda/dt$. In particular, by assuming the nonlinear nonaffine model presented in [99], we find that such relation monotonically decreases for increasing stretch rates with the law

$$\tau = A\left(\frac{d\lambda}{dt}\right)^{-B}, \tag{5.19}$$

where A= 2.94s^{1-B}, B = 1.12 and $d\lambda/dt$ is the stretch rate of the elastomer (response) that we assume being coincident with the frequency f (stimulus) of the voltage input of the DE actuator during each actuation cycle between the range $1 \le f \le$ 30 Hz. By equating (5.18) and (5.19) we get the expression of coefficient C_d as a function of the frequency f, namely

$$C_d = 2k_x A\left(\frac{d\lambda}{dt}\right)^{-B}. \tag{5.20}$$

It is worth to point out that the model leading to eq. (5.19) is validated [99] with an experimental investigation performed on VHB specimens longitudinally pre-stretched up to 6 times their initial length, for frequencies spanning over four orders of magnitude ($6.7\cdot10^{-5}$ – 0.67 Hz). In our case we have a biaxial stress state with a similar longitudinal stretch but also a transverse stretch and higher actuation frequencies. However, despite these discrepancies, due to the lack of both experimental data and models available in literature, by taking into account higher frequencies and biaxial stretch states, we adopt this model to describe the behaviour of our DE actuator, although a certain grade of approximation might be introduced. The model was analysed with the COMSOL's "Frequency Domain Study" solver in the range of frequencies investigated in the experiments allowing for obtaining the frequency dependent displacements of the structure reported in the following. The chosen frequency step was Δf = 0.1 Hz.

5.2.6 Locomotion test: experimental setup and test procedure

The experimental setup here described was conceived to measure the locomotion speed of the robot as a function of the actuation frequency of the DE actuator. In this regard, a 0.3 m long testing track consisting of a flat surface coated by a thin sheet of baking paper to achieve homogeneous roughness was used as a surface course. A laser optical transducer (optoNCDT, Micro-Epsilon, USA) was used as finish line, while a high-voltage amplifier (Model 10/10B, Trek Inc., USA) provided the driving voltage. The generator was connected to the electrodes of the DE actuator by means of two thin metal stripes and thin wires to avoid any constraint during the locomotion. A square wave voltage signal V, with 6 kV of amplitude, was provided to the DE actuator with frequencies within the range 5-30 Hz. A custom made LabView program allowed for simultaneously applying the driving voltage to the DE actuator (thus triggering the locomotion of the robot) and record the time of its application. Both the voltage and the time counter were automatically switched off when the robot reached the vertical laser beam located at the end of the testing track. For each frequency tested, the average locomotion speed of the robot was obtained by measuring the time needed to complete the full length of the testing track. Each locomotion test was repeated five times, allowing for obtaining the experimental speed values in terms of mean and standard deviation. Figure 5.15 shows a picture of the experimental setup used for the tests.

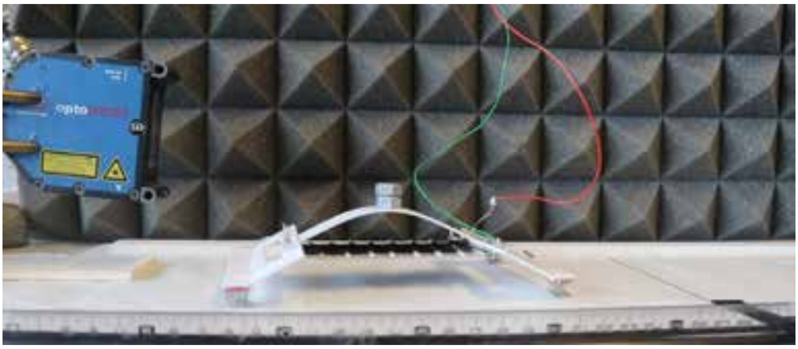

FIGURE 5.15: Picture of the experimental setup.

5.3 Results and discussion

The locomotion tests revealed that a forward displacement δ_x was observed only when the robot was equipped with the steel bristle pads. Conversely, a vibration about the starting position, with no net displacement, was recorded when the robot was equipped with the 3D printed bristles for any whole frequency in the range 5-30 Hz. This evidence suggests that the magnitude of the frictional anisotropy generated by the robot's bristles plays a key role for achieving a forward motion. Indeed, as shown in Figure 5.8, the 3D printed bristles featured a much smaller frictional anisotropy compared to the steel ones; this result justifies the inability of the robot to advance on the surface chosen for the experiments. The experimental values of the locomotion speed measured during the tests performed with the steel bristles are shown with blue circles in Figure 5.16.

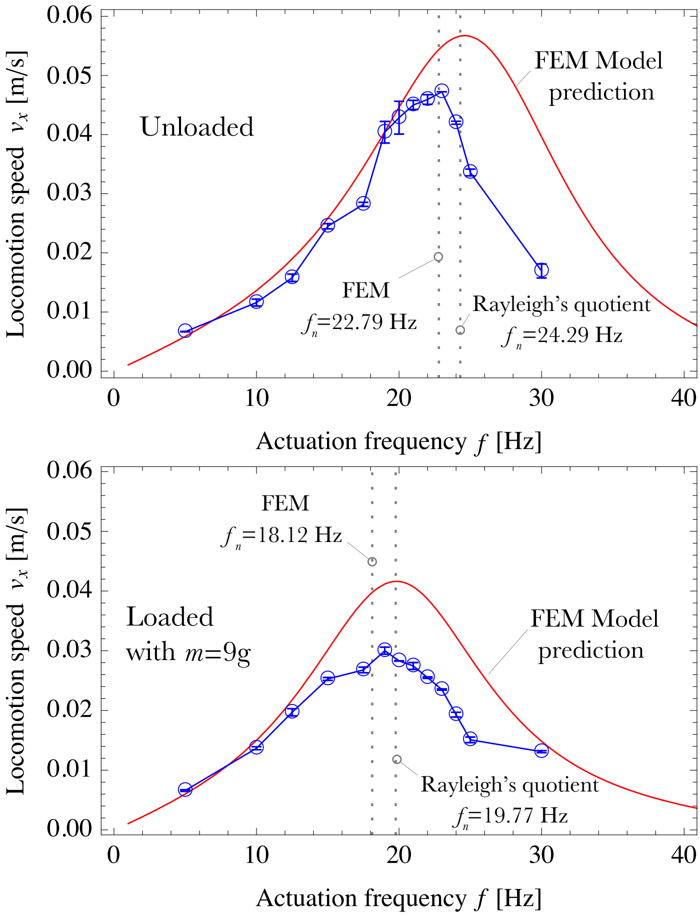

FIGURE 5.16: Locomotion speed v_x vs actuation frequency f: experimental data and model prediction for the unloaded (top) and loaded with m=9 g (bottom) robot. Bars represent the standard deviation of measures. The two dotted lines represent the fundamental frequency f_n calculated with either the Rayleigh's quotient method (on the right in both plots) or the FEM modal analysis (on the left in both plots).

In particular, Figure 5.16(bottom) reports the locomotion speed measured for the robot loaded with a lumped mass m=9 g whereas Figure 5.16(top) shows the results for the case of unloaded robot. We observe that the locomotion speed increased in both cases up to a maximum value, namely 3.0 cm/s at an actuation frequency of 19 Hz in the former case and 4.7 cm/s at f=23 Hz in the latter. The two vertical dotted lines drawn in each graph mark the fundamental frequencies f_n estimated with the two methods described in Section § 5.2.4. The data reported Figure 5.16 show that for both the cases of unloaded and loaded robot, the maximum value of the experimental locomotion speed lies within the range of fundamental frequencies calculated with the two proposed methods. In particular, the Rayleigh's quotient method gives an upper-bound estimate of f_n whereas the FEM calculations provide values that are approximately 6.5% and 9.5% lower with respect to the former for the unloaded and the loaded robot, respectively. From the superposition between the experimental data and the locomotion speed model predictions, calculated with the FEM frequency response analysis described in Section § 5.2.4, we see that the model predicts a rising locomotion speed up approximately to the fundamental frequency. For higher values of the frequency f, the model foresees lower values of the speed v_x in a fairly good agreement with the experimental data. In the absence of any damping mechanism, we would have expected an unbounded, asymptotic behaviour for the locomotion speed at the fundamental frequency f_n computed via FEM (indicated with 'FEM' in Figure 5.16), that also represents the resonance frequency for the system. In the current framework, the peak of the locomotion speed is slightly shifted to the right with respect to f_n as, in eq. (5.17), the displacement is multiplied by the frequency f itself. The behaviour highlighted in the previous paragraph can be explained by considering that the frequency response of the robot is given by a combination of its eigenmodes. Indeed, for increasing value of the actuation frequency from zero to the first eigenvalue, the structure would tend to vibrate according to the first eigenmode, as represented in Figure 5.17 (top).

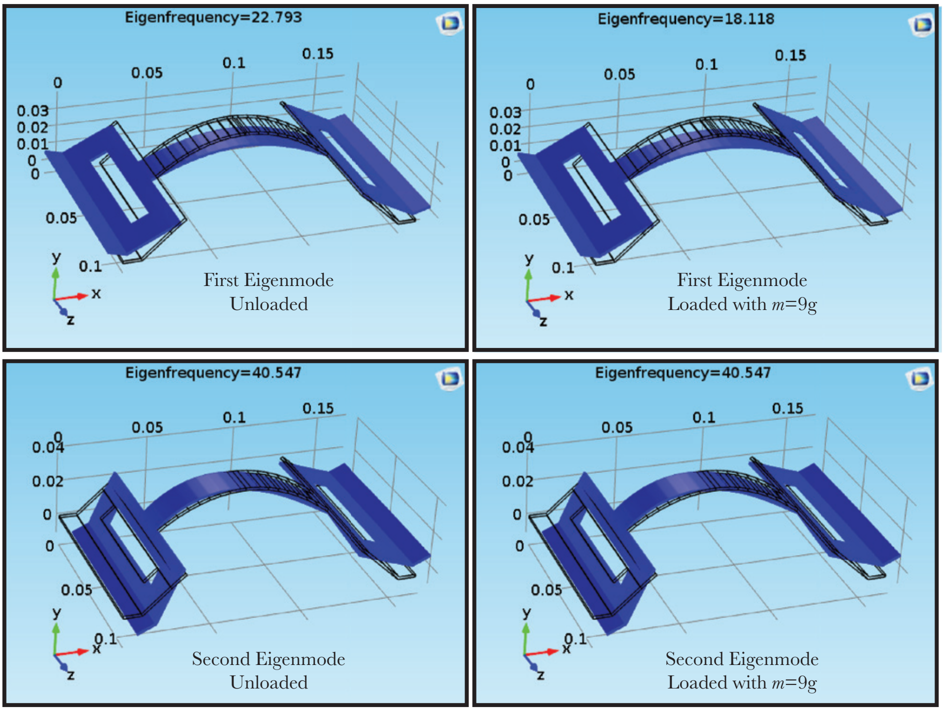
Eigenfrequency=22.793
First Eigenmode
Unloaded
Eigenfrequency=18.118
First Eigenmode
Loaded with m=9g
Eigenfrequency=40.547
Second Eigenmode
Unloaded
Eigenfrequency=40.547
Second Eigenmode
Loaded with m=9g
0
0.05
0.1
0.15
0.03
0.02
0.01
0.04
y
x
z

FIGURE 5.17: Eigenfrequencies and modal shapes of a 3D model of the robot: first vibration mode for the unloaded (top left) and loaded with m=9 g (top right) robot; second vibration mode for the unloaded (bottom left) and loaded with m=9 g (bottom right) robot.

Since the first eigenmode is symmetric, the net displacement δ_x is given by the sum of two components that are equal in modulus. Conversely, when the robot vibrates according the second eigenmode (shown in Figure 5.17, bottom), which is asymmetric, the net displacement δ_x sharply decreases. This behaviour highlights the importance of identifying the correct value of the first eigenfrequency in order to maximise the locomotion speed.

As previously anticipated, the fundamental frequency f_n of the robot decreases at an increase of the weight of the lumped mass. Figure 5.18 shows the experimental data points correspondent to the value of f_n measured at the maximum locomotion speed (i.e. in correspondence with the natural vibration frequency) and the outcome of both FEM analysis (red solid line) and Rayleigh's quotient method (solid blue line), the former interpolating a finite number of points whose distance along the abscissa corresponds to $\Delta m = 0.1$ g. The agreement between tests and theory is very good.

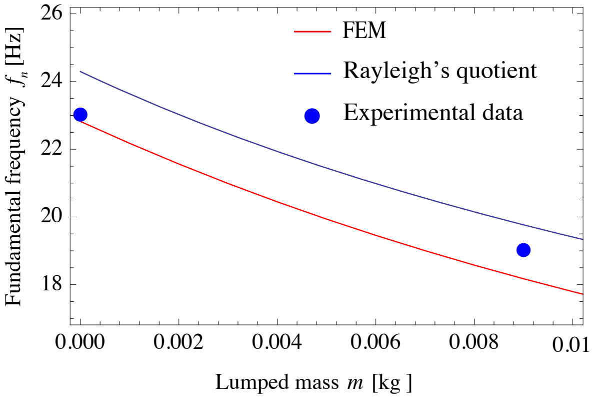

FIGURE 5.18: Fundamental frequency vs lumped mass weight. The experimental data corresponding to the peak values of the locomotion speed, namely 19 Hz for m=9 g and 23 Hz for m=0 are marked by dots. The blue solid line represents the predictions of the Rayleigh's quotient method whereas the red solid one refers to the FEM calculations performed with a step along the abscissa corresponding to Δm=0.1 g.

Despite the inability of the 3D printed bristles to trigger locomotion for such low grade of frictional anisotropy, it is worth to point out that the effect of the bristle's angle on the actuation performance might be relevant when the frictional anisotropy reaches the threshold. Indeed, when a set of bristles reaches the frictional anisotropy threshold for locomotion, since the frictional anisotropy is null when both the back and front bristle's angle are either 0° or 90°, it must be that that for an intermediate value of the bristle's angle the frictional anisotropy is maximised. In our case, from the friction measurements performed on the 3D printed bristles reported in Figure 5.9, we see that both the static and dynamic friction coefficients peak for an angle of 35° for a backward sliding, while it seems that the maximum value is in the range 35°- 45° when the sliding is forward. The relatively high value of friction observed for the angle whose value is 15° in both the backward and the forward sliding might be explained with the indentation occurred between the sharp tips and the paper, which is reasonable to observe for such a low value of the bristle's angle. Either the identification of the optimum value of such an angle to achieve the maximum locomotion speed or the investigation of other kind of bristles might be the goals of a future work.

5.4 Conclusions

In this paper, we have presented the concept of a novel kind of limbless resonating locomotion robot supported by four pads with asymmetric metallic rigid bristles. The forward motion of the robot was generated by the voltage-driven elongation of the dielectric elastomer actuator that triggers a partial release of the elastic energy stored in the plastic beam, enabling the stick-slip locomotion favoured by the frictional anisotropy of the pads. The locomotion speed reached a maximum in the vicinity of the fundamental frequency of the system that was estimated either analytically or numerically. The behaviour of the robot was successfully captured by a numerical model where the damping characteristics of the elastomer were simulated with a Kelvin-Voigt rheological scheme.

We have also 3D-printed and tested similar robots equipped with resin pads with different bristle's angles. However, all those systems proved not to be able to display any forward motion. The reason is to be found in the lack of anisotropy of the friction coefficients for the pads.

Chapter 6

Summary and Outlook

6.1 Summary and Outlook

The work presented in this thesis is divided into three sets of investigations.

The first one, presented in Chapter 3, is about the use of dielectric elastomer actuators for the development of soft active compression bandages. Such bandages may be worn as a medical aid to counteract dynamically, rather than statically, limb swelling due to various pathologies or conditions. Since dielectric elastomers require high voltage to operate, the problem of proper electrical insulation to prevent electrical shocks was solved by using soft silicone layers coating the dielectric elastomer active layers. In doing so, we showed that the passive layers coating the bandage have a function that goes beyond those of electrical protection and mechanical impedance matching. Indeed, evidences about the existence of an optimum value of the passive layer thickness were found. Also, we found that the variation of the voltage-induced contact pressure increases with the number of active layers, with a saturation trend. A theoretical framework, specifically developed for the case of prestretched multiple layers, was also developed. These outcomes are expected to serve as help for future improvements of the design, implementation and manufacturing process of prestretched multi-layer electroactive bandages.

Suggestions for further studies specific to this kind of actuator were included in §3.8.

The second work, presented in Chapter 4, reports about the use of dielectric elastomers in a soft actuator designed for the manipulation of delicate and fragile objects. This actuator, which is an upgraded version of the Hydrostatically Coupled Dielectric Elastomer Actuator presented by Carpi et al. [28], enables for generating a 3D trajectory (instead of a push-pull action allowed by the older version) thanks to a new design featuring segmented electrodes. This new feature endows the actuator with a multi-degree of freedom kinematics that allows for the simultaneous generation of both a normal and a tangent voltage-induced action. We found that, for this kind of actuators, the relation between the contact area and the normal force acting at the interface with an object is given by an analytical function (obtained by fitting the experimental data) describing an extension of the contact mechanics law of Hertz. This relation showed that the actuator features a gentle touch similar to the soft silicone fingers used in robotics, hence allowing for its use with delicate objects.

Future works may be required to study the dimensional scalability of HC-DEAs. Indeed, while the literature reports on millimeter scale HC-DEAs, there seems to be a lack of knowledge regarding HC-DEAs with a diameter over a few centimeters. Also, as highlighted for the soft active compression bandage developed in Chapter 3, the influence of thicker coating layers on the actuation performance may be of interest for applications where the direct contact with humans might be required.

The third work, presented in Chapter 5, shows a locomotion robot composed of a linear DE actuator and a flexible beam. Thanks to the presence of asymmetric rigid bristles the robot is able to perform locomotion when the DE actuator is activated. We demonstrated that when the robot is actuated at increasing frequency, its structure exploits the resonance condition to reach the maximum locomotion speed. The range of frequencies in which the top locomotion speed was observed during the experiments was accurately estimated both analytically and numerically. The locomotion speed of the robot as a function of the actuation frequency was also estimated with a frequency response analysis performed on a discretised model of the structure, revealing good agreement with the experimental evidence.

Future developments may lead to the design of a fully autonomous untethered version of this robot, where all the electronics and batteries needed could be put in place of the lumped mass, actually taken into account by both the analytic and numerical models presented. Indeed, the increasing energy density of lithium-ion batteries in conjunction with the miniaturization of the high voltage electronics highlighted in §3.8.3 may soon lead to the development of a new class of autonomous soft robots of this kind, that may benefit from the theoretical framework here developed.

Appendix A

List of Publications

Papers on international journals

- Calabrese, L., Frediani, G., Gei, M., De Rossi, D. E. and Carpi, F. (2018). Active compression bandage made of electroactive elastomers. *IEEE/ASME Transactions on Mechatronics*, 23(5), 2328-2337.
- De Acutis, A., Calabrese, L., Bau, A., Tincani, V., Pugno, N. M., Bicchi, A. and De Rossi, D. E. (2018). Design and proof of concept for multi degree of freedom hydrostatically coupled dielectric elastomer actuators with roto-translational kinematics for object handling. *Smart Materials and Structures*, 27(7), 074005.
- Calabrese, L., Berardo, A., De Rossi, D. E., Gei, M., Pugno, N. M., and Fantoni, G. (2019). A soft robot structure with limbless resonant, stick and slip locomotion. *Smart Materials and Structures*, (submitted).

Conference presentations

- Calabrese, L., Frediani, G., N. Pugno, Gei, M., De Rossi, D. E. and Carpi, F. On the actuation of multilayer dielectric elastomer actuators interfaced to compressive loads via thick soft membranes. EuroEAP International conference 2016, Helsingør (Denmark), June 14-15 2016.
- De Acutis, A., Calabrese, L., Bau, A., Tincani, V., Pugno, N. M., Bicchi, A., De Rossi, D. E. Soft platforms for objects transportation. EuroEAP International conference 2017, Cartagena (Spain), June 6-7 2017.
- Calabrese, L., Gei, M., De Rossi, D. E., Pugno, N. M., Fantoni, G., Dielectric elastomer based prototype of a mechanically resonating inchworm-like robot with unidirectional claws. EuroEAP International conference 2018, Lyon (France), June 5-6 2018.
- Calabrese, L., Gei, M., De Rossi, D. E., Pugno, N. M., Fantoni, G., Dielectric elastomer driven resonating inchworm-like robot with unidirectional claws. 10th European Solid Mechanics Conference (ESMC), Bologna (Italy), July 2-6 2018.

Abstracts

- De Acutis, A., Calabrese, L., Bau, A., De Rossi, D. E. Slowbots, object propulsion and locomotion. Italian Institute of Technology (IIT), Genova (Italy), November 28 2016.
- De Rossi, D.E., Calabrese, L., De Acutis, A., Slowbots for autonomus navigation. 7th Journées Nationales sur la Récuperation et le Stockage d'Energie. Lyon (France), May 9-10 2017.
- Calabrese, L., Frediani, G., Gei, M., De Rossi, D. E. and Carpi, F. Optimisation of dielectric elastomer limb compression bands for biomedical applications. EMMC15 15th European Mechanics of Materials Conference, Brussels (Belgium), September 7-9 2016.
- De Rossi, D.E., Calabrese, L., De Acutis, A., Slowbots: low-gear pest busters. 9th World Congress on Biomimetics, Artificial muscles and Nano-bio. Wollongong, Australia, September 25-27 2017.

Bibliography

[1] Deepak Trivedi, Christopher D Rahn, William M Kier, and Ian D Walker. Soft robotics: Biological inspiration, state of the art, and future research. *Applied bionics and biomechanics*, 5(3):99–117, 2008.

[2] Sangbae Kim, Cecilia Laschi, and Barry Trimmer. Soft robotics: a bioinspired evolution in robotics. *Trends in biotechnology*, 31(5):287–294, 2013.

[3] Guo-Ying Gu, Jian Zhu, Li-Min Zhu, and Xiangyang Zhu. A survey on dielectric elastomer actuators for soft robots. *Bioinspiration & biomimetics*, 12(1):011003, 2017.

[4] Carmel Majidi. Soft robotics: A perspective—current trends and prospects for the future. *Soft Robotics*, 1:5–11, 03 2014.

[5] Daniela Rus and Michael T Tolley. Design, fabrication and control of soft robots. *Nature*, 521(7553):467, 2015.

[6] David Brock. Review of artificial muscle based on contractile polymers. Technical report, MASSACHUSETTS INST OF TECH CAMBRIDGE ARTIFICIAL INTELLIGENCE LAB, 1991.

[7] Danilo DeRossi, Kanji Kajiwara, Yoshihito Osada, and Aizo Yamauchi. Polymer gels. In *Fundamentals and Biomedical Applications*. Springer, 1991.

[8] Yoshihito Osada and Mariko Hasebe. Electrically activated mechanochemical devices using polyelectrolyte gels. *Chemistry Letters*, 14(9):1285–1288, 1985.

[9] Danilo de rossi, Piero Chiarelli, G Buzzigoli, C Domenici, and Luigi Lazzeri. Contractile behavior of electrically activated mechanochemical polymer actuators. *ASAIO transactions / American Society for Artificial Internal Organs*, 32:157–62, 07 1986.

[10] D De Rossi, M Suzuki, Y Osada, and P Morasso. Pseudomuscular gel actuators for advanced robotics. *Journal of intelligent material systems and structures*, 3(1):75–95, 1992.

[11] RH Baughman. Conducting polymer artificial muscles. *Synthetic metals*, 78(3):339–353, 1996.

[12] A Della Santa, D De Rossi, and A Mazzoldi. Characterization and modelling of a conducting polymer muscle-like linear actuator. *Smart Materials and Structures*, 6(1):23, 1997.

[13] Federico Carpi, Danilo De Rossi, Roy Kornbluh, Ronald Edward Pelrine, and Peter Sommer-Larsen. *Dielectric elastomers as electromechanical transducers: Fundamentals, materials, devices, models and applications of an emerging electroactive polymer technology*. Elsevier, 2008.

[14] Robert F Shepherd, Filip Ilievski, Wonjae Choi, Stephen A Morin, Adam A Stokes, Aaron D Mazzeo, Xin Chen, Michael Wang, and George M Whitesides. Multigait soft robot. *Proceedings of the national academy of sciences*, 108(51):20400–20403, 2011.

[15] Koichi Suzumori, Shoichi Iikura, and Hiroshisa Tanaka. Applying a flexible microactuator to robotic mechanisms. *IEEE Control systems magazine*, 12(1):21–27, 1992.

[16] Fionnuala Connolly, Panagiotis Polygerinos, Conor J Walsh, and Katia Bertoldi. Mechanical programming of soft actuators by varying fiber angle. *Soft Robotics*, 2(1):26–32, 2015.

[17] Raphael Deimel and Oliver Brock. A novel type of compliant and underactuated robotic hand for dexterous grasping. *The International Journal of Robotics Research*, 35(1-3):161–185, 2016.

[18] Steven Ceron, Itai Cohen, Robert Shepherd, James Pikul, and Cindy Harnett. Fiber embroidery of self-sensing soft actuators. *Biomimetics*, 3(3):24, 2018.

[19] Ching-Ping Chou and Blake Hannaford. Measurement and modeling of mckibben pneumatic artificial muscles. *IEEE Transactions on robotics and automation*, 12(1):90–102, 1996.

[20] Graham Robinson and J Bruce C Davies. Continuum robots-a state of the art. In *Proceedings 1999 IEEE international conference on robotics and automation (Cat. No. 99CH36288C)*, volume 4, pages 2849–2854. IEEE, 1999.

[21] Robert J Webster III and Bryan A Jones. Design and kinematic modeling of constant curvature continuum robots: A review. *The International Journal of Robotics Research*, 29(13):1661–1683, 2010.

[22] L Margheri, C Laschi, and B Mazzolai. Soft robotic arm inspired by the octopus: I. from biological functions to artificial requirements. *Bioinspiration & biomimetics*, 7(2):025004, 2012.

[23] B Mazzolai, L Margheri, M Cianchetti, P Dario, and C Laschi. Soft-robotic arm inspired by the octopus: Ii. from artificial requirements to innovative technological solutions. *Bioinspiration & biomimetics*, 7(2):025005, 2012.

[24] Carter S Haines, Márcio D Lima, Na Li, Geoffrey M Spinks, Javad Foroughi, John DW Madden, Shi Hyeong Kim, Shaoli Fang, Mônica Jung de Andrade, Fatma Göktepe, et al. Artificial muscles from fishing line and sewing thread. *science*, 343(6173):868–872, 2014.

[25] Yoseph Bar-Cohen. Electroactive polymers as artificial muscles-capabilities, potentials and challenges. *Handbook on biomimetics*, 8, 2000.

[26] Ron Pelrine, Roy Kornbluh, Qibing Pei, and Jose Joseph. High-speed electrically actuated elastomers with strain greater than 100%. *Science*, 287(5454):836–839, 2000.

[27] Todd A Gisby, Benjamin M O'Brien, and Iain A Anderson. Self sensing feedback for dielectric elastomer actuators. *Applied Physics Letters*, 102(19):193703, 2013.

[28] F. Carpi, G. Frediani, and D. De Rossi. Hydrostatically coupled dielectric elastomer actuators. *IEEE/ASME Transactions on Mechatronics*, 15(2):308–315, April 2010.

[29] Federico Carpi and Elisabeth Smela. *Biomedical applications of electroactive polymer actuators*. John Wiley & Sons, 2009.

[30] Federico Carpi. *Electromechanically active polymers: a concise reference*. Springer, 2016.

[31] Matthias Kollosche, Jian Zhu, Zhigang Suo, and Guggi Kofod. Complex interplay of nonlinear processes in dielectric elastomers. *Phys. Rev. E*, 85:051801, May 2012.

[32] Jiangshui Huang, Tiefeng Li, Choon Chiang Foo, Jian Zhu, David R. Clarke, and Zhigang Suo. Giant, voltage-actuated deformation of a dielectric elastomer under dead load. *Applied Physics Letters*, 100(4), 2012.

[33] Christoph Keplinger, Tiefeng Li, Richard Baumgartner, Zhigang Suo, and Siegfried Bauer. Harnessing snap-through instability in soft dielectrics to achieve giant voltage-triggered deformation. *Soft Matter*, 8(2):285–288, 2012.

[34] Paul Brochu and Qibing Pei. Advances in dielectric elastomers for actuators and artificial muscles. *Macromolecular rapid communications*, 31(1):10–36, 2010.

[35] Federico Carpi, Siegfried Bauer, and Danilo De Rossi. Stretching dielectric elastomer performance. *Science*, 330(6012):1759–1761, 2010.

[36] Zhigang Suo. Theory of dielectric elastomers. *Acta Mechanica Solida Sinica*, 23(6):549–578, 2010.

[37] Morton E Gurtin, Eliot Fried, and Lallit Anand. *The mechanics and thermodynamics of continua*. Cambridge University Press, 2010.

[38] A Dorfmann and RW Ogden. Nonlinear electroelasticity. *Acta Mechanica*, 174(3-4):167–183, 2005.

[39] Katia Bertoldi and Massimiliano Gei. Instabilities in multilayered soft dielectrics. *Journal of the Mechanics and Physics of Solids*, 59(1):18–42, 2011.

[40] Ronald E Pelrine, Roy D Kornbluh, and Jose P Joseph. Electrostriction of polymer dielectrics with compliant electrodes as a means of actuation. *Sensors and Actuators A: Physical*, 64(1):77–85, 1998.

[41] Robert T Eberhardt and Joseph D Raffetto. Chronic venous insufficiency. *Circulation*, 111(18):2398–2409, 2005.

[42] Michele Brignole and David G Benditt. Pathophysiology of syncope. In *Syncope*, pages 15–25. Springer, 2011.

[43] Thomas Lewis. A lecture on vasovagal syncope and the carotid sinus mechanism. *British medical journal*, 1(3723):873, 1932.

[44] AH Chen, SG Frangos, S Kilaru, and BE Sumpio. Intermittent pneumatic compression devices–physiological mechanisms of action. *European Journal of Vascular and Endovascular Surgery*, 21(5):383–392, 2001.

[45] John J Bergan, Geert W Schmid-Schönbein, Philip D Coleridge Smith, Andrew N Nicolaides, Michel R Boisseau, and Bo Eklof. Chronic venous disease. *New England Journal of Medicine*, 355(5):488–498, 2006.

[46] Hugo Partsch, Michael Clark, Giovanni Mosti, Erik Steinlechner, Jan Schuren, Martin Abel, Jean-Patrick Benigni, Philip Coleridge-Smith, Andre Cornu-Thénard, Mieke Flour, et al. Classification of compression bandages: practical aspects. *Dermatologic surgery*, 34(5):600–609, 2008.

[47] NH Hills, JJ Pflug, K Jeyasingh, Lynn Boardman, and JS Calnan. Prevention of deep vein thrombosis by intermittent pneumatic compression of calf. *Br Med J*, 1(5793):131–135, 1972.

[48] Alexander GG Turpie, Jack Hirsh, Michael Gent, Denise Julian, and Judith Johnson. Prevention of deep vein thrombosis in potential neurosurgical patients: a randomized trial comparing graduated compression stockings alone or graduated compression stockings plus intermittent pneumatic compression with control. *Archives of internal medicine*, 149(3):679–681, 1989.

[49] Shahram Pourazadi, Sadegh Ahmadi, and Carlo Menon. Towards the development of active compression bandages using dielectric elastomer actuators. *Smart Materials and Structures*, 23(6):065007, 2014.

[50] Shahram Pourazadi, Sadegh Ahmadi, and Carlo Menon. On the design of a dea-based device to pot entially assist lower leg disorders: an analytical and fem investigation accounting for nonlinearities of the leg and device deformations. *Biomedical engineering online*, 14(1):103, 2015.

[51] Tongqing Lu, Jiangshui Huang, Christa Jordi, Gabor Kovacs, Rui Huang, David R Clarke, and Zhigang Suo. Dielectric elastomer actuators under equal-biaxial forces, uniaxial forces, and uniaxial constraint of stiff fibers. *Soft Matter*, 8(22):6167–6173, 2012.

[52] Rong Liu, Yi Lin Kwok, Yi Li, Terence TH Lao, Xin Zhang, and Xiao Qun Dai. Objective evaluation of skin pressure distribution of graduated elastic compression stockings. *Dermatologic Surgery*, 31(6):615–624, 2005.

[53] Soo Jin Adrian Koh, Tiefeng Li, Jinxiong Zhou, Xuanhe Zhao, Wei Hong, Jian Zhu, and Zhigang Suo. Mechanisms of large actuation strain in dielectric elastomers. *Journal of Polymer Science Part B: Polymer Physics*, 49(7):504–515, 2011.

[54] S Roccabianca, Massimiliano Gei, and D Bigoni. Plane strain bifurcations of elastic layered structures subject to finite bending: theory versus experiments. *IMA journal of applied mathematics*, 75(4):525–548, 2010.

[55] Federico Carpi and Danilo De Rossi. Dielectric elastomer cylindrical actuators: electromechanical modelling and experimental evaluation. *Materials Science and Engineering: C*, 24(4):555–562, 2004.

[56] Jian Zhu, Hristiyan Stoyanov, Guggi Kofod, and Zhigang Suo. Large deformation and electromechanical instability of a dielectric elastomer tube actuator. *Journal of Applied Physics*, 108(7):074113, 2010.

[57] Fabia Galantini, Federico Carpi, and Giuseppe Gallone. Effects of plasticization of a soft silicone for dielectric elastomer actuation. *Smart Materials and Structures*, 22(10):104020, 2013.

[58] Michael Bozlar, Christian Punckt, Sibel Korkut, Jian Zhu, Choon Chiang Foo, Zhigang Suo, and Ilhan A Aksay. Dielectric elastomer actuators with elastomeric electrodes. *Applied physics letters*, 101(9):091907, 2012.

[59] Mavinakere Eshwaraiah Raghunandan, Jitendra S Sharma, and Biswajeet Pradhan. A review on the effect of rubber membrane in triaxial tests. *Arabian Journal of Geosciences*, 8(5):3195–3206, 2015.

[60] Emco - High Voltage Corporation [online]. `http://www.emcohighvoltage.com`. Accessed: 30-3-2019.

[61] Frederikke B Madsen, Anders E Daugaard, Søren Hvilsted, and Anne L Skov. The current state of silicone-based dielectric elastomer transducers. *Macromolecular rapid communications*, 37(5):378–413, 2016.

[62] Simon J Dünki, Yee Song Ko, Frank A Nüesch, and Dorina M Opris. Self-repairable, high permittivity dielectric elastomers with large actuation strains at low electric fields. *Advanced Functional Materials*, 25(16):2467–2475, 2015.

[63] Alexandre Poulin, Samuel Rosset, and Herbert R Shea. Printing low-voltage dielectric elastomer actuators. *Applied Physics Letters*, 107(24):244104, 2015.

[64] Martin Hägele, Klas Nilsson, J Norberto Pires, and Rainer Bischoff. Industrial robotics. In *Springer handbook of robotics*, pages 1385–1422. Springer, 2016.

[65] Tao Wang, Jinhua Zhang, Jun Hong, and Michael Yu Wang. Dielectric elastomer actuators for soft wave-handling systems. *Soft robotics*, 4(1):61–69, 2017.

[66] Chiwon Lee, Myungjoon Kim, Yoon Jae Kim, Nhayoung Hong, Seungwan Ryu, H Jin Kim, and Sungwan Kim. Soft robot review. *International Journal of Control, Automation and Systems*, 15(1):3–15, 2017.

[67] Josie Hughes, Utku Culha, Fabio Giardina, Fabian Guenther, Andre Rosendo, and Fumiya Iida. Soft manipulators and grippers: a review. *Frontiers in Robotics and AI*, 3:69, 2016.

[68] Eric Brown, Nicholas Rodenberg, John Amend, Annan Mozeika, Erik Steltz, Mitchell R Zakin, Hod Lipson, and Heinrich M Jaeger. Universal robotic gripper based on the jamming of granular material. *Proceedings of the National Academy of Sciences*, 107(44):18809–18814, 2010.

[69] GmbH FH. WaveHandling [online]. `https://www.festo.com/net/SupportPortal/Files/248127/Festo_WaveHandling_en.pdf`. Accessed: 30-3-2019.

[70] Martin Stommel, Weiliang Xu, P.P.K. Lim, and Bourhane Kadmiry. Robotic sorting of ovine offal: Discussion of a soft peristaltic approach. *Soft Robotics*, 1(4):246–254, 2014.

[71] Bobak Mosadegh, Aaron D. Mazzeo, Robert F. Shepherd, Stephen A. Morin, Unmukt Gupta, Idin Zhalehdoust Sani, David Lai, Shuichi Takayama, and George M. Whitesides. Control of soft machines using actuators operated by a braille display. *Lab Chip*, 14:189–199, 2014.

[72] Z. Deng, M. Stommel, and W. Xu. A novel soft machine table for manipulation of delicate objects inspired by caterpillar locomotion. *IEEE/ASME Transactions on Mechatronics*, 21(3):1702–1710, June 2016.

[73] A T Conn and J Rossiter. Towards holonomic electro-elastomer actuators with six degrees of freedom. *Smart Materials and Structures*, 21(3):035012, feb 2012.

[74] Andreas Tröls, Alexander Kogler, Richard Baumgartner, Rainer Kaltseis, Christoph Keplinger, Reinhard Schwödiauer, Ingrid Graz, and Siegfried Bauer. Stretch dependence of the electrical breakdown strength and dielectric constant of dielectric elastomers. *Smart Materials and Structures*, 22(10):104012, sep 2013.

[75] F. Carpi, R. Kornbluh, P. Sommer-Larsen, D. D. Rossi, and G. Alici. Guest editorial introduction to the focused section on electroactive polymer mechatronics. *IEEE/ASME Transactions on Mechatronics*, 16(1):1–8, Feb 2011.

[76] Nicholas Xydas and Imin Kao. Modeling of contact mechanics and friction limit surfaces for soft fingers in robotics, with experimental results. *The International Journal of Robotics Research*, 18(9):941–950, 1999.

[77] Brygida M. Dzidek, Michael J. Adams, James W. Andrews, Zhibing Zhang, and Simon A. Johnson. Contact mechanics of the human finger pad under compressive loads. *Journal of The Royal Society Interface*, 14(127):20160935, 2017.

[78] Federico Carpi, Gabriele Frediani, Sergio Tarantino, and Danilo De Rossi. Millimetre-scale bubble-like dielectric elastomer actuators. *Polymer International*, 59(3):407–414, 2010.

[79] Yang M Wood KL Fu K, Moreno D. Bio-inspired design: An overview investigating open questions from the broader field of design-by-analogy. *ASME. J. Mech. Des*, 136(11):111102–111102–18, 2014.

[80] Owen Holland and David McFarland. *Artificial Ethology*. Oxford University Press, Inc., New York, NY, USA, 2001.

[81] Editor Langton, C.G. *Artificial life: an Overiview, in: Complex Adaptive System*. MIT Press., Cambridge, Massachussetts - London, England, 1997.

[82] Jean-Arcady Meyer and Agnes Guillot. *Biologically Inspired Robots*, pages 1395–1422. In: B. Siciliano, O. Khatib (eds) Springer Handbook of Robotics, Springer Berlin Heidelberg, Berlin, Heidelberg, 2008.

[83] B. Trimmer S. Kim, C. Laschi. Soft robotics: a bioinspired evolution in robotics. *Trends in Biotechnology*, 31(5):287–294, Cell Press, 2013.

[84] Michael H. Dickinson, Claire T. Farley, Robert J. Full, M. A. R. Koehl, Rodger Kram, and Steven Lehman. How animals move: An integrative view. *Science*, 288(5463):100–106, 2000.

[85] Boye K. Ahlborn, Robert W. Blake, and William M. Megill. Frequency tuning in animal locomotion. *Zoology*, 109(1):43 – 53, 2006.

[86] A Filippov and Stanislav Gorb. Frictional-anisotropy-based systems in biology: Structural diversity and numerical model. *Scientific reports*, 3:1240, 02 2013.

[87] Halvor T. Tramsen, Stanislav Gorb, Hao Zhang, Poramate Manoonpong, Zhendong Dai, and Lars Heepe. Inversion of friction anisotropy in a bioinspired asymmetrically structured surface. *Journal of The Royal Society Interface*, 15:20170629, 01 2018.

[88] Samuel Rosset, Benjamin M O'Brien, Todd Gisby, Daniel Xu, Herbert R Shea, and Iain A Anderson. Self-sensing dielectric elastomer actuators in closed-loop operation. *Smart Materials and Structures*, 22:104018, 09 2013.

[89] Philippe Dubois, Samuel Rosset, Muhamed Niklaus, Massoud Dadras, and Herbert Shea. Voltage control of the resonance frequency of dielectric electroactive polymer (deap) membranes. *Microelectromechanical Systems, Journal of*, 17:1072 – 1081, 11 2008.

[90] L. Calabrese, G. Frediani, M. Gei, D. De Rossi, and F. Carpi. Active compression bandage made of electroactive elastomers. *IEEE/ASME Transactions on Mechatronics*, 23(5):2328–2337, Oct 2018.

[91] Mokarram Hossain, Duc Vu, and Paul Steinmann. A comprehensive characterization of the electro-mechanically coupled properties of vhb 4910 polymer. *Archive of Applied Mechanics*, 85, 11 2014.

[92] Giancarlo Cicconofri and Antonio Desimone. Motility of a model bristle-bot: a theoretical analysis. *International Journal of Non-Linear Mechanics*, 76, 10 2014.

[93] Giancarlo Cicconofri, Felix Becker, Giovanni Noselli, Antonio Desimone, and Klaus Zimmermann. *The Inversion of Motion of Bristle Bots: Analytical and Experimental Analysis*, volume 569, pages 225–232. 01 2016.

[94] G. B. Warburton. Dynamics of structures, by ray w. clough and joseph penzien, 2nd edition, mcgraw-hill, new york, 1993. no. of pages: 738. isbn 0-07-011394-7. *Earthquake Engineering & Structural Dynamics*, 24(3):457–462, 1995.

[95] B Wunderlich. Low-temperature properties of polymers, i. i. perepechko, pergamon, london, 1980, 301 pp. *Journal of Polymer Science: Polymer Letters Edition*, 20:241–242, 04 1982.

[96] K H. Illers and E Jenckel. Dynamic mechanical behavior of polystyrene, poly-p-chlorostyrene, and poly-p-bromostyrene at low temperatures. *Journal of Polymer Science*, 41:528 – 531, 12 1959.

[97] Jillian Kiser, Michael Manning, David Adler, and Kenneth Breuer. A reduced order model for dielectric elastomer actuators over a range of frequencies and prestrains. *Applied Physics Letters*, 109, 09 2016.

[98] R.M. Christensen. Chapter i - viscoelastic stress strain constitutive relations. In R.M. Christensen, editor, *Theory of Viscoelasticity (Second Edition)*, pages 1 – 34. Academic Press, second edition edition, 1982.

[99] Paul Miles, Michael Hays, Ralph Smith, and William Oates. Bayesian uncertainty analysis of finite deformation viscoelasticity. *Mechanics of Materials*, 91:35 – 49, 2015.

Dielectric elastomer (DE) actuators are electromechanical transducers that essentially consist of one layer of an insulating soft elastomer coated on both sides with compliant electrodes. When a voltage is applied between the electrodes, an electrostatic pressure deforms the elastomer triggering the motion of the actuator. In this thesis, this principle is exploited for the development of three different actuators: an electroactive compression bandage, a hydrostatically coupled actuator for use in the field of soft manipulators and a dielectric elastomer based inchworm-like robot able to perform locomotion. By doing so, several challenges related to the design, to the modeling and to the manufacturing of this kind of devices are raised and tackled.

During the development of the electroactive compression bandage, the issue of electrical insulation and prevention of electrical discharge in wearable devices was addressed by using coating layers as an interface between the DE actuator and the human body. Both experimental investigations and a finite electro-elasticity analytical model showed that the passive layers play a key role for an effective transmission of the actuation from the active layers to the load. Indeed, the model showed that by increasing the number of electroactive layers, the pressure variation can be increased, although with a saturation trend, providing a useful indication for future designs of such bandages. The second piece of work here reported consists in a design upgrade of the Hydrostatically Coupled Dielectric Elastomer Actuator (HC-DEA), already known in the literature, that enable its use in the field of soft manipulators. The new design features segmented electrodes, which stand as four independent elements on the active membrane of the actuator, enabling it for generating both out of plane and in plane motions. This novel design makes the actuator suitable for delicate transportation of a flat object. This capability was proven via an experimental investigation in which a flat Petri dish was roto-translated on a platform composed of two actuators. The electromechanical transduction performance of the actuator was characterized and its contact mechanics was modeled.Finally, a smart robot structure that exploits anisotropic friction to achieve stick-slip locomotion is presented. The robot, which is made out just of a plastic beam, a planar dielectric elastomer actuator and four bristle pads with asymmetric rigid metallic bristles, exploits the resonance condition to reach the maximum locomotion speed. The fundamental frequency of the structure, which was estimated both analytically and numerically, was identified within the range of frequencies in which the top locomotion speed was observed during the experiments to be identified.

Luigi Calabrese was born in Chiusi, Siena, Italy in 1986. He received the Laurea degree in civil engineering from the University of Perugia, Perugia, Italy in 2011 and a Master degree in structural engineering from the University of Trento, Trento, Italy in 2015. He is currently pursuing a Ph.D. degree in modeling and simulation within the Doctoral Programme in Civil, Environmental and Mechanical Engineering at University of Trento. Since 2015 he has been research fellow with the Interdepartmental Research Center “E. Piaggio,” School of Engineering, University of Pisa. His research interests focus on the development of electroactive-polymer-based mechatronic devices. Since 2014 he is member of the EuroEAP – European Society for Electromechanically Active Polymer Transducers & Artificial Muscles, where he has been volunteering since 2018 as president of the Dissemination & Outreach Committee.